A Study of Optical Scattering Methods in Laboratory Plasma Diagnostics

by

Claude R. Phipps, Jr.

March 1972

SUIPR Report No. 462

National Aeronautics and Space Administration
Grant NGR-05-020-277

INSTITUTE FOR PLASMA RESEARCH
STANFORD UNIVERSITY, STANFORD, CALIFORNIA

A STUDY OF OPTICAL SCATTERING METHODS IN LABORATORY PLASMA DIAGNOSTICS

by

Claude R. Phipps, Jr.

National Aeronautics and Space Administration
Grant NGR-05-020-277

SUIPR Report No. 462

March 1972

Institute for Plasma Research
Stanford University
Stanford, California

ACKNOWLEDGMENT

In a thesis published several years ago at Stanford, another graduate student explicitly acknowledged the help of the Deity in the successful completion of his work. While I would not presume that the Divine Being would consider this work of sufficient import to give it His assistance, there have been times during the course of it when Divine Intervention, or plain good luck, obviously came to my aid.

I have also received magnificent support from a number of mortal individuals, but they are too numerous to mention, so I will just list those without whose help I would have been much less likely to finish.

First among these are my wife Lynn and son David who bore with me (literally) through over six years at Stanford, the latter for 80% of his present life span. Lynn also drew the originals for most of the figures in this work. Second, I would like to thank Howard Stine, head of the High Enthalpy Research Branch at NASA-Ames for his continuing financial and moral support through some extremely lean times for experimental research.

Without the theoretical and practical assistance of both Professors Oscar Buneman and Daniel Bershader, this experiment would not have been done. Also, both gentlemen saw to it that my work was focussed on something, while providing a freedom that I will be fortunate to find again.

In designing the experiment itself, I leaned heavily on Jack MacGowan. He is primarily responsible for reducing my initial ideas to something that could be built, as well as for the design and construction of the scattering chamber and vacuum system.

The precision of the experimental results is also due to the careful

machine work of John Schick, Jerry deWerk, Joe Price, Karl and Rainer Neumarker and Gunter Kuhn, and the electronic expertise of Geert deGraff.

During the process of getting this work in printed form, I have been fortunate in having the cheerful help of one of the most efficient technical typists I know, Evelyn Carr.

Finally, I wish to thank Harry Sitam, who always wished me well, Professor Bob Gray who reminded me that it was worthwhile, Paul Bailiff who reminded me that I was worthwhile, and Gary McDonough who made the rough roads smooth.

ABSTRACT

Electron velocity distributions are deduced along axes parallel and perpendicular to the magnetic field in a pulsed, linear Penning discharge in hydrogen by means of a laser Thomson scattering experiment. Results obtained are numerical averages of many individual measurements made at specific spacetime points in the plasma evolution, and take advantage of the high level of reproducibility of density and velocity parameters possible in this type of discharge. Observation solid angles are made quite small to maximize resolution between the two distributions. Because of the high resolution in k-space and the relatively low maximum electron density $2 \times 10^{13} cm^{-3}$, special techniques were required to obtain measurable scattering signals. These techniques are discussed and experimental results are presented.

Our Thomson scattering measurements show identical behavior of the longitudinal and azimuthal distributions, within experimental error. For magnetic fields below the critical value for onset of strong instability in the Penning discharge, our results show impressively good fit to a calculated gaussian distribution, for electron energies up to 6 times the thermal energy. However, measurements above this critical field show a distinct excess of high energy electrons which cannot be accounted for by a single gaussian, within experimental error. Equipment scattered light levels are the lowest ever attained in an experiment of this kind.

TABLE OF CONTENTS

LIST OF ILLUSTRATIONS

1. INTRODUCTION

1.1 General

Since the availability of ruby lasers made Thomson scattering practicable in laboratory plasmas[1,2] this technique has attracted intense interest as a plasma diagnostic tool. The prime reason for this interest is that Thomson scattering makes directly available the ion and electron velocity distributions and thus in principle does not require thermal equilibrium for either species. Furthermore it can be used anywhere a beam of light can be sent, provided the electron density is sufficient to produce a detectable scattered signal. In particular, this method is well suited for regions of density and temperature inaccessible to standard techniques, such as occur in thermonuclear plasmas.

In this work, we are reporting results from an experiment in which the electron velocity distributions parallel and perpendicular to the axis of a linear Penning discharge plasma are measured. Our purpose is to determine whether the overall distribution is anisotropic. For the first time, these distributions are measured separately and unequivocally at a particular spacetime coordinate, with convincing independence between the two measurements. The Penning discharge is used because it can be conveniently driven from quiescent operation to strong drift-type instabilities at sufficiently high density to make scattering measurements feasible. We operate the machine in a pulsed mode so that the dynamic history of velocity and density parameters may be constructed, as a function of the applied magnetic field. The discharge is operated in hydrogen.

This experiment is a member of the emerging second generation of Thomson scattering experiments, in which this technique is used as a

well understood tool and where the surprises are expected from the plasma rather than from the physics governing scattering.

For the benefit of the reader who has not used this technique, it should be mentioned that such experiments invariably involve a large initial investment of time (in our case approximately 10^4 man hours), considerable expense and patience. Nevertheless, it is a powerful, precise and widely applicable method which can yield measurements of plasma parameters that can be obtained in no other way.

1.2 Brief Introduction to Thomson Scattering and Its Applications

Electromagnetic wave scattering by density fluctuations in a plasma has been properly understood for just over a decade. Prior to the pioneering experiment of Bowles[3] in 1958, the richness of information contained in the scattered spectrum was not realized. This experiment was the stimulus for intensive theoretical work in the early 1960's[6-16] which resulted in a complete scattering theory based on a modern understanding of plasma fluctuations.

Gordon[4] suggested the Bowles experiment in a paper which showed the feasibility of using radar backscatter measurements for the remote determination of electron density and temperature at any level in the earth's ionosphere. It was originally thought that the backscattered microwave spectrum would have a thermal doppler width characteristic of the electron temperature at the chosen level. The expected spread of frequencies in the scattered signal was of the order of 20 Khz. at a radar frequency of 40 Mhz. However, Bowles' results showed a spread many times smaller than could be explained by the lowest available estimates of electron temperatures at the observation height.

Bowles himself realized[5] that his results were explained if the observed scattering was produced by just the electron density fluctuations required to neutralize the slow density fluctuations of the more massive ions in the plasma. Of course, the electron spectrum is not always absent, and with the benefit of modern scattering theory we would say that a particular combination of frequency, scattering angle and electron density and temperature permitted Bowles to observe only the "ion feature" of his plasma (see Chapter 2). In contrast, our experiment is concerned only with the "electron feature", where the scattered signal is doppler shifted according to the electron velocity distribution.

To investigate a plasma in the laboratory, it is necessary to scale down the illumination wavelength to the optical region, for two reasons. First, laboratory plasmas tend to have Debye lengths of the order of several microns at most and, as will be seen in Chapter 2, the illumination wavelength must be much less than 4π times the Debye length in order to observe electron features. Second, any experiment designed to measure scattering off thermal fluctuations in a plasma requires quite large photon densities in the illumination beam just to get one or two photons into the detector. It happens that lasers are the only adequately bright primary beam sources of appropriate wavelength available today. Visible or near infrared lasers are indicated because detectors are more sensitive in this region. In plasmas with very large Debye lengths where far infrared or microwave sources would be permitted in principle, the diffraction limited spacial resolution is insufficient for the small plasmas found in laboratories.

It is true that powerful x-ray sources are also available. Unfortunately, these are not sufficiently bright or monochromatic, and

individual x-ray photons are so energetic that, for fixed illumination energy, fewer photons enter the experiment. At the detector, this is a statistical disadvantage.

In the next chapter, we discuss the theory of Thomson scattering, before continuing the history of scattering experiments in Chapter 3.

2. THOMSON SCATTERING - THEORY

2.1 Definition of Scattering Types

Photon "scattering" occurs when a beam of electromagnetic radiation penetrates a material medium. The electric field of the illuminating wave produces microscopic electric currents which are then the source of secondary or "scattered" photon radiation. The latter will generally travel in different directions and have different frequencies than the illuminating wave.

"Thomson" and "Compton" scattering are subclasses in which the motion of free charged particles causes the scattering. Thomson scattering[17] is the long-wavelength, classical limit of electric monopole scattering, and applies when the photon energy is much less than or approximately equal to the particle rest energy.*

In contrast, when the scattering is due to the motion of bound electrons, Mie-Debye[18] scattering is obtained. Rayleigh scattering is the long-wavelength limit of this process, for frequencies well below resonance for the electrons in a molecule or ion system.

2.2 Scattering by Single Nonrelativistic Electrons

According to the Larmor formula, a free electron being accelerated by the electric field of a plane, linearly polarized, monochromatic electromagnetic wave $\bar{E} = E_o e^{i(\bar{k}_i \cdot \bar{x} - \omega_i t)}$ gives rise to a reradiated field of instantaneous magnitude

$$|\bar{E}_r| = \frac{e^2 E_o}{mc^2 R} \sin\Psi = \frac{E_o r_o}{R} \sin\Psi \qquad (2\text{-}1)^{**}$$

*For scattering from electrons, with $m_e c^2 = 511$ Kev, the Thomson approximation is valid up through the x-ray region. Thomson's work was in fact done to describe the scattering of x-rays by electrons.

**Gaussian units are used throughout this work, except as noted.

in direction Ψ relative to $\vec{E}_o$ and distance R, so that average power into unit solid angle around this direction is

$$\frac{dP}{d\Omega} = \frac{c\left\langle |E_r|^2 \right\rangle}{4\pi} R^2 = \frac{cE_o^2}{8\pi} r_o^2 \sin^2\Psi \ . \qquad (2\text{-}2)$$

If this power is normalized to unit incident intensity $cE_o^2/8\pi$, the "total Thomson differential scattering cross-section" is obtained,

$$\frac{d\sigma_T}{d\Omega} = r_o^2 \sin^2\Psi \qquad (2\text{-}3)$$

where r_o^2 is the square of the classical electron radius and equal to 7.94×10^{-26} cm^2. We see that Thomson scattered radiation, like any dipole radiation, is isotropic in the plane normal to $\bar{E}_o$ and linearly polarized in the plane containing $\bar{E}_o$ and $\bar{R}$. The power of Thomson scattering as a diagnostic method lies in the extreme simplicity of this relationship between the incident and scattered fields. It is violated only when the illuminating field is intense enough to cause relativistic motions of the electron, but to avoid this it is sufficient to have

$$E_o \lambda_o << \pi(m_e c^2/e) = \pi W_o \text{ volts} \ , \qquad (2\text{-}4)$$

where W_o is the electron rest energy. This is an easy limit, not exceeded e.g. for 0.7μ radiation until $E_o = 2 \times 10^{10}$ v/cm or $I_o = 5 \times 10^{17}$ watts/cm^2.*

*This criterion is mathematically the same as Bernstein's requirement that the electron's excursion during illumination be less than a wavelength of the incident wave.

2.3 Scattering by Cloud of Independent Electrons

For a tenuous cloud of randomly spaced electrons (but no ions as yet) such that $n_e^{-1/3} \gg \lambda_o$, there will hardly ever be more than one electron in a cubic wavelength cell, and their vibrations in the illuminating field will be uncorrelated. Then the scattered photon number from a volume V of such electrons into solid angle $d\Omega$ will be

$$\frac{N_{sc}}{\hat{N}_o} = n_e V \left(\frac{d\sigma_T}{d\Omega}\right) d\Omega \tag{2-5}$$

with $\hat{N}_o$ the number of incident photons per unit area. This is just the sum of the individual radiated intensities.

If the cloud is still composed of independently moving randomly spaced electrons, but is more dense such that $n_e^{-1/3} \ll \lambda_o$, we may consider the total scattering for the sake of discussion to be the sum of contributions from adjacent cells in the volume V, each cell having edge length $\lambda_o/2$. If the density were absolutely uniform, at any given instant there would be no net scattered electric field because of exact phase cancellation between adjacent cell scattered fields. If we allow random (thermal) density fluctuations, however, say a number $(N_j + \delta N_j)$ of electrons in the jth cell, this cell's contribution to the scattered field will be proportional to $\delta N_j e^{i\phi_j}$ and the ensemble averaged total scattered intensity to

$$\begin{aligned}\left\langle N_{sc}\right\rangle &\propto \left\langle |E_{sc}|^2\right\rangle \propto \left\langle \left|\sum_j e^{i\phi_j}\delta N_j\right|^2\right\rangle \\ &= \left\langle \sum_j (\delta N_j)^2\right\rangle + \left\langle \sum_k \sum_{j\neq k} e^{i(\phi_j-\phi_k)}\delta N_j \delta N_k\right\rangle \\ &= \left\langle \sum_j (\delta N_j)^2\right\rangle = \sum_j N_j = n_e V \ . \end{aligned} \tag{2-6}$$

This is because the assumption of independence requires the density

fluctuations in adjacent cells to be independent and thus $\langle \delta N_j \delta N_k \rangle = \langle \delta N_j \rangle \langle \delta N_k \rangle = 0$. Therefore (2-5) describes scattering from a cloud of independent electrons whether or not $n\lambda_o^3 > 1$.*

This discussion shows the importance of density fluctuations to scattering and predicts that the calculation of scattered power will be complicated by the absence of independence, as for example when coherent density waves are present. In fact, in the limit of perfect dependence, the term we ignored in (2-6) becomes n times larger than the one we kept, where n is the number of cells in V, according to the present simple analysis. In actuality, the coherent cross-section is arbitrarily large.

2.4 Scattering by Plasma: Heuristic Results

The introduction of an equal number of positive ions into the electron cloud produces a much more complicated situation in which the electrons are less independent and scatter less efficiently[6,8,10,15]. The primary effects are on the frequency distribution of the scattered light which we will consider in the next section. It should be mentioned that equation (2-1) shows that scattered power varies inversely as the mass squared of the scattering particle, so that direct scattering by the ions of a hydrogen plasma should have an intensity only 3×10^{-7} of that due to the electrons, and less for heavier ions. But the ions do have a strong effect on the scattered spectrum through the electron velocity distribution.

We define the important parameter α as the ratio of the "momentum exchange length" 1/k to the electron Debye length $D_e = (KT_e/4\pi n_e e^2)^{1/2}$

* If, however, the electrons are neutralized by even a smeared-out non-discrete positive charge background, more exact calculation are necessary.[12]

where $k = |\bar{k}| = |\bar{k}_s - \bar{k}_i| = 2k_i \sin\frac{\theta}{2}$* and $\hbar k$ is the amount of momentum exchanged when an incident photon with momentum $\hbar\bar{k}_i$ is deflected through a scattering angle θ to the direction $\bar{k}_s$ of the scattering observer. Then

$$\alpha = \frac{1}{(kD_e)} \quad . \tag{2-7}$$

As shown by Buneman[15], the overall effect of the ions on the total scattering cross-section can be expressed by a modulation function $S(\alpha)$, so that equation (2-3) for electron cloud scattering is replaced by:

$$\frac{d\sigma_T}{d\Omega} = S(\alpha) r_o^2 \sin^2\Psi \tag{2-8}$$

and

$$S(\alpha) = \left\{ \frac{1}{1+\alpha^2} + \frac{Z\alpha^4}{(1+\alpha^2)\left[1+\alpha^2\left(1+\frac{ZT_e}{T_i}\right)\right]} \right\} \tag{2-9}$$

where Z is the ionic charge number. This result is more or less independent of the exact nature of the electron and ion velocity distribution functions so long as an approximate temperature exists. The same result was obtained also by Salpeter[12]. The main features of this modulation are that it tends to $\left(\frac{Z}{1+ZT_e/T_i}\right)$ in the limit $\alpha \gg 1$ and 1.0 in the limit $\alpha \ll 1$ (see Figure 1). The case $\alpha \ll 1$ will be seen to be equivalent to the case of free independent electron scatterers in what is to follow.

*For nonrelativistic plasmas, the doppler shift of scattered light, being proportional to v/c, will be only a few percent. Thus the change in photon momentum magnitude $|\bar{k}|/k_i$ is ignorable in most cases.

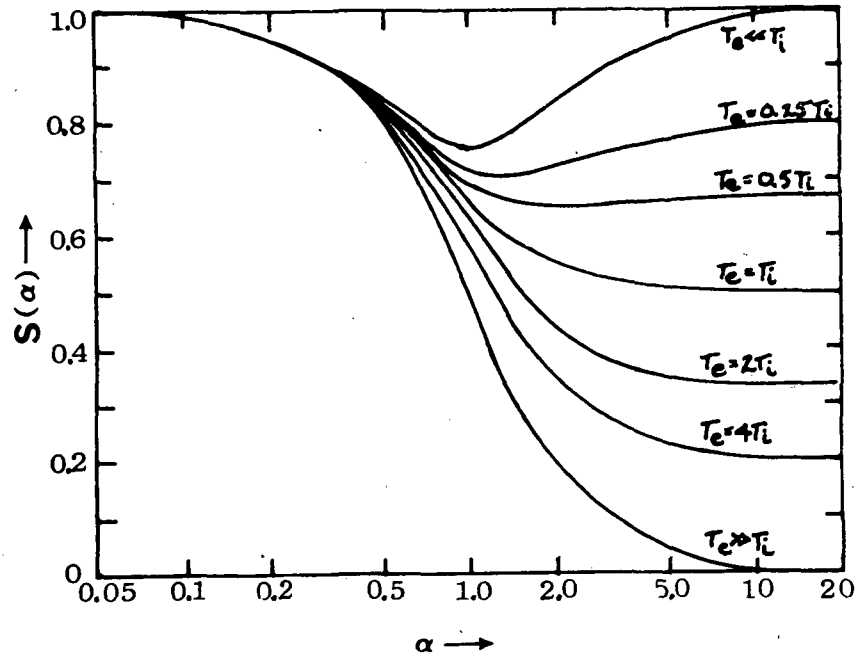

Figure 1

Total Thomson Cross-Section Modulation Function

Unfortunately a more accurate calculation of $S(\alpha)$ is necessary for large α and large temperature ratios T_e/T_i and especially when large electron-ion drift velocities are present as well, due to the ion-acoustic resonance at frequencies $\frac{\omega_{ac}}{k} = \sqrt{\frac{ZKT_e}{m_i}}$ corresponding to the ion sound speed. This resonance can contribute arbitrarily large scattering analogous to critical opalescence in solids[19], whereas (2-9) predicts zero scattering under these conditions. Also, we need a calculation that shows the frequency dependence of Thomson scattering as well as the k-dependence we have been considering up to now.

At the beginning of this section, we provided an initial motivation for the consistent appearance of the momentum difference vector $\hbar\bar{k}$, rather than the incident or scattered beam vectors $\hbar\bar{k}_i$ or $\hbar\bar{k}_s$ in the

scattering formalism, by mentioning momentum conservation. In fact, a moment's heuristic thought will make the qualitative predictions of the scattering theory quite plausible. If we observe (in the scattering plane) a photon scattered into a small solid angle around direction θ to the illumination direction, we are seeing the result of momentum transfer from a plasma electron to the incident photon in the direction $\bar{k}$ (see Figure 2).

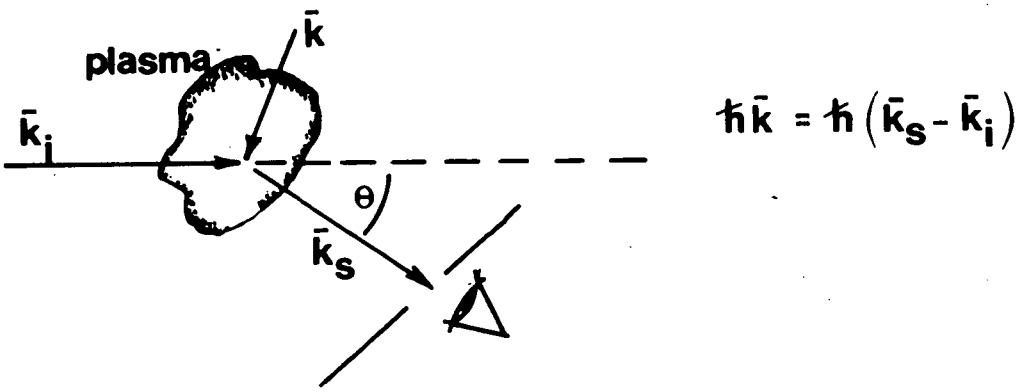

Figure 2
Illustrating Momentum Transfer

The amount of the electron's total momentum $m_e\bar{v}$ which is transferred in a particular event depends only on its momentum vector component along $\bar{k}$ just prior to illumination. If the detector has frequency discrimination ability, the amount of momentum transfer can be measured quite easily from the scattered photon's doppler shift $\omega = \omega_s - \omega_i = \bar{k} \cdot \bar{v}_e$ when the electrons are nonrelativistic. A calculated modulation function $S(\bar{k},\omega)$ (also called the dynamic form factor) determines the extent to which density fluctuations attenuate or enhance the scattered photon flux in a particular plasma. However, it will be shown that this function is simple in the absence of large scale coherent density waves.

If we momentarily ignore the effect of this modulation (independent) electron scatterers, section 2.3), the measured scattered photon intensity into solid angle $d\Omega$ around a fixed direction θ will be seen to have a frequency distribution

$$\frac{N_{sc}(\bar{k},\omega)}{\hat{N}_o} = n_e V \frac{d\sigma_T}{d\Omega} f_{ek}\left(\frac{\omega}{\bar{k}}\right) d\Omega \qquad (2\text{-}10)$$

which is proportional to the one-dimensional electron velocity distribution function $f_{ek}\left(\frac{\omega}{\bar{k}}\right)$ along the direction $\bar{k}$. In (2-10), this function is normalized so that its integral is unity. The primary effect of varying θ will in this case be to change k and thus the velocity scale factor of the observed distribution. The only additional limitation that arises in this discussion is the implicit assumption from which the power of Thomson scattering techniques derives, that the amount of an electron's total momentum $m_e v$ transferred to a scattered photon is very small. This will be true for any θ if $h/\lambda_o \ll m_e v$ or, which is the same thing if

$$\frac{v}{c} \gg \frac{h\nu_o}{m_e c^2} . \qquad (2\text{-}11)$$

This is an easy limit also, since for 0.7μ radiation it amounts to avoiding measurements on electrons with temperatures lower than $0.05^{o}K$. It is extremely unlikely that an electron will emit more than one scattered photon in a particular scattering event, since the probability of a particular electron scattering one photon is only $\frac{6.7 \times 10^{-25}}{A}$, where A is the cross-section area of the illuminating beam in cm^2.

2.5 Scattering by Plasma: Direct Calculation

Since Akhiezer et al.[20] first indicated the importance of thermal density fluctuations in the calculation of plasma Thomson scattering, several authors have contributed to an exact calculation and useful approximations which we outline here[6,8,10,14,19,21].

We consider a volume V of plasma containing $N = n_e V$ electrons with $V \gg D_e^3$. From an origin within V, we will note the observer position by $\bar{R}$ and the position of the jth electron by $\bar{x}_j$. Under the influence of an illuminating wave $\bar{E} = \bar{E}_o\, e^{i(\bar{k}_i \cdot \bar{x} - \omega_i t)}$ the scattered electric field due to acceleration of the jth electron is:

$$\bar{E}_{sj}(\bar{R},t) \cong \frac{e^2 E_o}{mc^2 R} [\hat{R} \times (\hat{R} \times \hat{E}_o)]\, e^{i(\bar{k}_i \cdot \bar{x}_j' - \omega_i t_j')} . \qquad (2\text{-}12)$$

In the above, the retarded time $t_j' = t - \frac{|\bar{R} - \bar{x}_j'|}{c}$, $\bar{x}_j' = \bar{x}_j(t_j')$, $\hat{}$ denotes a unit vector and we have made the approximation $\frac{1}{|\bar{R} - \bar{x}_j'|} \cong \frac{1}{R}$ in the field amplitude only for an observer located well away from the scattering volume. Now we approximate the retarded time by

$$t_j' \approx t - \frac{R}{c} + \frac{\hat{R} \cdot \bar{x}_j(t - R/c)}{c} \qquad (2\text{-}13)$$

so that the phase factor becomes approximately

$$\phi_j \approx \exp i\left\{\bar{k}_i \cdot \bar{x}_j\left(t - \frac{R}{c}\right) - \omega_o\left[t - \frac{R}{c} + \frac{\hat{R} \cdot \bar{x}_j\left(t - \frac{R}{c}\right)}{c}\right]\right\}$$

$$\approx \exp i\left\{\bar{k} \cdot \bar{x}_j\left(t - \frac{R}{c}\right) - \omega_o\left[t - \frac{R}{c}\right]\right\} \qquad (2\text{-}14)$$

where we have introduced the difference vector $\bar{k} = \bar{k}_i - \bar{k}_s \cong \bar{k}_i - \frac{\omega_o \hat{R}}{c}$. Therefore,

$$\bar{E}_{sj}\left(\bar{R}, t + \frac{R}{c}\right) \cong \frac{r_o E_o}{R} [\hat{R} \times \hat{R} \times \hat{E}_o] e^{i(\bar{k} \cdot \bar{x}_j - \omega_o t)} . \qquad (2\text{-}15)$$

Now, the Thomson cross-section, which is just the total scattered intensity per unit solid angle in direction $\hat{R}$ normalized to unit incident intensity, can be written (since $|\hat{R} \times \hat{R} \times \hat{E}_o| = \sin\Psi$)

$$\frac{d\sigma_T}{d\Omega} = \frac{I_s\left(R, t + \frac{R}{c}\right)}{I_o} \cong \frac{R^2\left\langle |E_s,(R,t)|^2\right\rangle}{E_o^{\,2}}$$

$$= r_o^{\,2}\sin^2\Psi\left\langle \left| \sum_{j=1}^{N} e^{i(\bar{k}\cdot\bar{x}_j(t))} \right|^2 \right\rangle . \qquad (2\text{-}16)$$

In the above, $\langle\ \rangle$ indicates an ensemble average over all states of the plasma (assumed stationary), $\bar{x}_j = \bar{x}_j(t)$ and the first Born approximation ($|\bar{E}_s| \ll |\bar{E}_o|$) is assumed to be valid. We note that if we define the density of point electrons in the plasma by

$$n_e(\bar{x}) = \sum_{j=1}^{N} \delta(\bar{x}-\bar{x}_j) \qquad (2\text{-}17)$$

at time t, the space Fourier transform of this quantity is

$$n_e(\bar{k}) = \sum_{j=1}^{N} e^{-i\bar{k}\cdot\bar{x}_j(t)} . \qquad (2\text{-}18)$$

So,

$$\frac{d\sigma_T}{d\Omega} = r_o^{\,2}\sin^2\Psi\left\langle |n_e(\bar{k})|^2 \right\rangle . \qquad (2\text{-}19)$$

If we now also require the frequency dependence of scattered radiation, the same procedure yields

$$\frac{d\sigma_T}{d\Omega d\omega} = r_o^{\,2}\sin^2\Psi\ S(\bar{k},\omega) \qquad (2\text{-}20)$$

$$S(\bar{k},\omega) = |n_e(\bar{k},\omega)|^2 \qquad (2\text{-}21)$$

$$n_e(\bar{k},\omega) = \lim_{\tau\to\infty}\left\{\frac{1}{\tau}\int_\tau dt\ e^{i\omega t}\sum_{j=1}^{N} e^{-i\bar{k}\cdot\bar{x}_j(t)}\right\}. \qquad (2\text{-}22)$$

From this derivation and the Parseval theorem, we also have

$$S(\bar{k},\omega) = \int_V d\bar{x}\int_\tau dt\ e^{-i(\bar{k}\cdot\bar{x}-\omega t)}C(\bar{x},t) \qquad (2\text{-}23)$$

where $C(\bar{r},t) = \langle n(\bar{x},t')n(\bar{x}+\bar{r},t'+t)\rangle_{\bar{x},t'}$ is the "time dependent pair correlation function" of density fluctuations in the plasma.

Equation (2-20) forms the basis for all scattering calculations. The dynamic form factor $S(\bar{k},\omega)$ contains all information about the plasma density fluctuation spectrum, and its calculation is only symbolically possible in the general case. Fortunately, useful approximations have been developed.

In a typical approach[19], the linearized Vlasov-Poisson equations are used within the random phase approximation to compute the response of a plasma to a test charge. This response is then averaged over all particles in the plasma, considering each to be a test charge to obtain

$$S(\bar{k},\omega) = \left|\frac{1+4\pi\chi_i(\bar{k},\omega)}{\epsilon(\bar{k},\omega)}\right|^2 f_e\left(\frac{\omega}{\bar{k}}\right) + Z\left|\frac{4\pi\chi_e(\bar{k},\omega)}{\epsilon(\bar{k},\omega)}\right|^2 f_i\left(\frac{\omega}{\bar{k}}\right) \qquad (2\text{-}24)$$

where

$$\chi_{e\atop i}(\bar{k},\omega) = \lim_{\delta\to 0}\left\{-\frac{Ze^2}{m_{e\atop i}k^2}\int d\bar{v}\left(\frac{\bar{k}\cdot\bar{\nabla}_v f_e(\bar{v})}{\bar{k}\cdot\bar{v}-\omega-i|\delta|}\right)\right\} \qquad (2\text{-}25)$$

(Z=1 for electrons) are the free electron and ion polarizabilities, and

$$\epsilon(\bar{k},\omega) = 1 + 4\pi[\chi_e(\bar{k},\omega) + \chi_i(\bar{k},\omega)] \qquad (2\text{-}26)$$

is the plasma dielectric function.

In the Salpeter approximation, it is assumed that the velocity distributions are Maxwellian with electrons and ions allowed to have different temperatures. In this case, Salpeter finds essentially

$$S(k,\omega) \cong \left| \frac{1}{1 + \alpha^2 W\left(\frac{\omega}{\omega_e}\right)} \right|^2 \frac{e^{-(\omega/\omega_e)^2}}{\sqrt{\pi}\,\omega_e} + Z\left(\frac{\alpha^2}{1+\alpha^2}\right)^2 \left| \frac{1}{1 + \frac{ZT_e}{T_i}\left(\frac{\alpha^2}{1+\alpha^2}\right) W\left(\frac{\omega}{\omega_i}\right)} \right|^2 \frac{e^{-(\omega/\omega_i)^2}}{\sqrt{\pi}\,\omega_i} \qquad (2\text{-}27)$$

with

$$W(\xi) = \left\{ 1 - 2\xi e^{-\xi^2} \int_0^{\xi} e^{p^2} dp - i\sqrt{\pi}\, \xi\, e^{-\xi^2} \right\} \qquad (2\text{-}28)$$

and

$$\frac{\omega_{e,i}}{k} = \sqrt{\frac{2KT_{e,i}}{m_{e,i}}} \qquad (2\text{-}29)$$

is the electron or ion thermal velocity. For $\alpha \ll 1$, the Maxwellian dynamic form factor reduces to

$$\lim_{\alpha \to 0} S(\bar{k},\omega) = \frac{e^{-(\omega/\omega_e)^2}}{\sqrt{\pi}\,\omega_e} \quad , \qquad (2\text{-}30)$$

the so-called "electron feature". In the opposite limit $\alpha \gg 1$, the electron contribution condenses into 2 narrow Lorentzian spikes symmetrically displaced from the laser frequency by an amount equal to the Bohm-Gross frequency

$$\omega_B^2 = \omega_p^2 + \frac{3KT_e}{m_e} k^2 \approx \omega_p^2 \qquad (2\text{-}31)$$

These lines are called the "satellite lines" and their contribution to the total scattering cross-section for $\alpha \gg 1$ is proportional to α^{-2}. If the plasma is "cool", we see that their location tells us the plasma density. The actual width of the satellite lines is limited only by Landau damping in the Salpeter theory. However, when collisions are permitted, the necessary corrections are treated by Taylor and Comisar[24], Dougherty and Farley[9], Sitenko and Gurin[25], and especially well by Ron, Dawson and Oberman[26].

The right-hand term of (2-27) yields a contribution called the "ion feature" which is not perfectly gaussian, (having symmetric maxima away from zero frequency) but which has a width characteristic of the ion temperature. Because of the preponderant ionic mass, this width will usually be much smaller than the corresponding electron feature width, and will be harder to separate from the incident radiation at $\omega = 0$.

In $\alpha \gg 1$ experiments in particular, the assumptions leading to (2-27) may be strongly violated if there is a very large electron-ion drift velocity compared to electron thermal velocity or, at microwave illumination frequencies, if $T_e \gg T_i$. Also, as pointed out by Kegel[22], if the electron velocity distribution consists of separate cold and hot Maxwellians, strong enhancement of the scattering may occur, producing a strong central spike, and a spike in the vicinity of the plasma frequency even for $\alpha \ll 1$. All these effects result from the behavior of the functions which multiply the electron and ion distributions in equation (2-24). $S(\bar{k},\omega)$ may be arbitrarily large at any zero of the plasma dielectric function[23].

The effects of nonzero magnetic field on $S(\bar{k},\omega)$ have also been treated[7,8,11,27,28,29]. In general, the electron feature spectrum predicted with no field is found to be modulated by a periodic fine structure

at multiples of the electron cyclotron frequency, when the sensitivity vector $\bar{k}$ is perpendicular to the applied magnetic field. No effect is expected for $\bar{k}$ parallel to the field. This modulation is a manifestation of the Bernstein modes in (2-24). In our experiment, no effect from this source will be seen because the spacing between the modulation peaks is of the order 0.02 $\mathring{A}$ in the azimuthal spectrum, much less than our 5 $\mathring{A}$ resolution capability. For $\alpha \gg 1$, the effect of the magnetic field is much more complicated, depending in detail on the state of coupling between the upper hybrid and Bernstein modes[29].

Ichimaru[19] discusses the effect of large-scale turbulence and incipient instabilities upon the $\alpha \gg 1$ scattered spectrum. He has been able to derive an asymptotic expression, valid near a zero of the dispersion relation, which predicts tremendously enhanced scattering relative to that predicted for simple thermal fluctuations.

References 30-33 discuss relativistic corrections to the theory which are necessary for very hot plasmas. Brown and Rose[30], for example, show that in case $\alpha \ll 1$, a unique mapping exists between the spectral distribution and the electron velocity distribution. In principle, this relationship can always be inverted experimentally, to obtain the distribution function $f(\bar{v})$ from the total scattered intensity $S(\bar{k})$. Of course, our plasma is nonrelativistic.

Computations of scattering profiles according to the Salpeter theory appear, for example, in Gerry and Patrick[34] and Williamson et al.[35]

In the present work, we desire only to measure the electron feature of the scattered spectrum, i.e. $\alpha \ll 1$. Therefore equation (2-30) will adequately describe our scattering results, if we have a Maxwellian, nonrelativistic plasma, since the only significant deviations from (2-30) occur within a few plasma frequencies of the laser frequency and

$$(\omega_p/\omega_e) = \frac{\alpha}{\sqrt{2}} \ll 1 \ . \qquad (2\text{-}32)$$

3. SUMMARY OF PREVIOUS SCATTERING EXPERIMENTS

As mentioned in Chapter 1, optical scattering from free electrons was first observed in the laboratory by Fiocco and Thompson in 1962[1], using an electron beam as the scattering medium and a normal mode ruby laser for illumination. In 1963, Thompson[36] and Fünfer et al.[37] reported the first successful optical scattering from a laboratory plasma almost simultaneously. Since then, many experiments have been reported, showing the ion feature, the electron feature and combinations of the two.

The great majority of these experiments have involved dense plasmas ($n_e > 10^{16}$ cm^{-3}) giving several orders of magnitude greater total scattering than is possible in our experiment.

Among the ion feature experiments, the earliest was that of Fünfer et al., mentioned above. This work was performed in a theta-pinch where electron densities up to 10^{18} cm^{-3} were available. However, spectral resolution was insufficient to resolve the central peak of the ion feature. The satellite lines were not seen at this time, but were observed emerging for $\alpha \approx 1$ by the same group in 1964[38]. The experiments of DeSilva et al.[39] in the same year was the first in which both electron and ion features were measured in the same plasma (a hydrogen arc with $n \cong 10^{15}$cm^{-3}) by changing the scattering angle from a large to a small value. Even with this density, stray light was about 70% of the Thomson signal at the center of the electron feature.

The satellite lines were first clearly observed by Chan and Nodwell in 1965[40], and subsequently by Ramsden and Davies[41]. In the latter experiment, the plasma was a hydrogen theta-pinch with $n_e \approx 2 \times 10^{15}$ cm^{-3} and scattering angles of 13.5° and 90° gave α values of 3.0 and 0.5 respectively. Their experiment was the first to show both features with good resolution.

The experiment of Röhr[42,43] first showed the detailed shape of a satellite line, in a theta-pinch with $n_e = 5 \times 10^{17}$ cm^{-3} and $\Theta_e = \Theta_i = 32$ ev. Since α was only ~ 3.0 in this experiment, the line is not expected to be as narrow as in the limit $\alpha \gg 1$, yet is was found to be about 4 times broader (~ 15 Å) than could be explained by collisions. Nonuniform density in the scattering region was offered as the explanation. This experiment is also important because it is one of the first for which the number of electrons per Debye cube was of the order of unity. The Salpeter theory assumes $n_e D_e^3 \gg 1$.

Two other interesting ion feature experiments are those of Daehler and Ribe[44,45] and Kronast et al.[46] at Garching. Daehler has shown scattering cross-sections several times larger than the theoretical value, based on known plasma parameters in the Scylla theta-pinch at Los Alamos. He attributes this enhancement to superthermal density fluctuations. Kronast et al. were probably the first to show large net drifts of a plasma from ion feature measurements.

Several electron feature experiments have been done, and these will be mentioned only as they are relevant to our own experiment or for their historical interest. For an exhaustive listing, the reader is referred to the papers of Kunze[47] and of Evans and Katzenstein[48].

Electron feature measurements are more sensitive to stray laser light than are those of the ion feature, because the same order of scattered energy is spread over approximately $\sqrt{m_i/m_e}$ times greater doppler width for equal ion and electron temperatures. Accordingly, the ratio of stray to scattered light intensities per unit bandwidth at the spectrum center has usually been quite large in previous electron feature experiments. In the work of Fünfer et al. mentioned at the beginning of this chapter, this ratio was about 100:1 even with

Θ_e = 100 ev and $n_e = 10^{17}$ cm^{-3}. In the experiment of Davies and Ramsden[49] it was 1000:1 when the electron density was 5×10^{15} cm^{-3} and the electron temperature 3 ev.

The experiment of Gerry and Rose[50] in 1966 was the first in which the stray laser light level was reduced to the same order of magnitude as the scattered signal at the spectrum center, with plasma densities and temperatures similar to ours.* Their experiment was done in an argon plasma formed in a hollow cathode discharge at an electron density of only 5×10^{13}cm^{-3} and an electron temperature of the order of 5 ev. However, plasma light was always larger than the scattered signal in their experiment, reaching a maximum which prevented measurements at or beyond the strong Argon II line at 6886.6 Å. As a result, their data show Maxwellian behavior only out to 2 thermal half-widths. Their experiment is interesting because of the great care taken in its design.

Several electron feature measurements have been done in theta-pinches and other devices characterized by densities or temperatures much greater than ours. Only one of these, the work of Forrest, et al.[52] in 1970 is very interesting from our point of view. In this experiment, conducted by the Culham group on the Russian Tokamak T3-A machine, electron temperatures in the range 100 ev < Θ_e < 1000 ev were found, at densities of order 10^{13} cm^{-3}. Their laser energy was very similar to ours (about) 6 joules, Q-switched). In most cases, the stray light signal was 200 times the true scattered signal at the spectrum center. Since, at the

*The earlier experiment of Schwarz[51] showed a stray laser light contribution only one eighth of the scattered signal for $n_e = 10^{14}$ cm^{-3} and electron temperatures which must have been of order 5 ev. However, only electron density was measured, so that the "scattered signal" consisted of the entire integrated scattered spectrum.

spectrum center, their detector has a bandwidth designed to collect about the same proportion of the total scattered light as does our detector, their experiment may be directly compared to ours, with regard to stray laser light level. The result of such a comparison shows our stray light reduction methods to be superior to theirs by a factor of about 3,000. Also, measurements were made only on the blue side of the spectrum because of limited photomultiplier quantum efficiency in the red.

In all other respects, the Tokamak scattering experiment stands as a model for such work. Exhaustive measurements were made of electron temperature versus time, versus radial position and for various plasma parameters. Measurements show Maxwellian behavior out to 3.5 thermal half-widths. Standard deviation of the data points relative to a gaussian is very small, of the order of 5%. Of course, the Tokamak measurements were for only one direction of the sensitivity vector $\bar{k}$.

A very few experiments have also been done on shock-wave plasmas. Two of interest are those of Patrick[53] in 1965 and Martone and Segre[54] in 1969. In Patrick's experiment, electron density behind the shock in a magnetic annular shock tube between 10^{15} and 10^{17} cm^{-3}, and electron temperature in excess of 20 ev were found. His experiment showed stray laser light levels approximately 3×10^{4} greater than ours, and measurements were made at only two wavelengths. Martone and Segre performed their experiment in a hydrogen theta-pinch with preionization, and found electron temperatures of about 80 ev.

Experiments showing the expected cyclotron harmonic modulation of the scattered spectrum in a magnetic field have been done by Kellerer[55], Evans and Carolan[56], and Kronast and Benesch[57]. The latter experiment shows clear evidence of the Bernstein modes in an $\alpha \gg 1$ theta-pinch

plasma. Kellerer and Evans et al. have seen the same effect for moderate and low α respectively.

The experiments of Ringler and Nodwell[58,59,60] should be mentioned as an example of low measurements which show anomalous results. Although their α value is 0.4 (clearly not $\ll 1$), one still expects a basically gaussian scattered spectrum from their steady state electric arc plasma. Instead, several resonance peaks were found at multiples of the plasma frequency and these could not be explained as due to density nonuniformities in the scattering region. Kegel[61] has offered the explanation that at least one of the observed peaks could be due to the presence of hot and cold Maxwellians in the electron velocity distribution.

A very few continuous laser and plasma experiments have been done. A first experiment of this kind was done by Farrow and Buchsbaum in 1965[62]. The experiment of Koons and Fiocco[63,64], in 1968, is of far greater interest to us, because it is the first in which electron temperatures parallel and perpendicular to the field direction in a magnetized plasma were measured. Their experiment was done in a reflex discharge in argon, with an illumination wavelength of 4880 $\mathring{A}$. Their results show a longitudinal temperature about 2.5 times larger than the transverse temperature. Measurements were made for doppler shifts out to a maximum of 2 thermal half-widths. Except for the type of discharge, our experiments are sufficiently different that a comparison of results is pointless. In the first place, the length of their plasma column is only twice its diameter. In our experiment, we have been careful to make measurements at a point about 15 plasma diameters distant from the reflex cathodes, in order to avoid the turbulent cathode-fall region near the electrodes. Also, Koons and Fiocco have a plasma which is only 1% ionized so that it is completely dominated by electron-neutral collisions. In contrast,

the density of neutrals in our plasma is never much greater than the electron density. As explained in Chapter 4, completely different transport mechanisms and instabilities exist for reflex discharges in the collisionless and collision-dominated regimes. Finally, their magnetic field is 1 kilogauss, whereas most of our measurements are made at quite low fields. Equipment scattered light is also quite large in their experiment, being some 20 times the scattered signal. This was probably due to the use of flat black rather than shiny black stray light trapping surfaces.

Toward the completion of our work, we became aware of independent work in a continuous hollow-cathode discharge being completed at M.I.T. by McCormick[65]. This experiment is also set up to measure longitudinal and azimuthal temperatures in a plasma which has similar density and temperature to ours. His laser stray light level is 5 times the Thomson signal at spectrum center, or about 100 times the level we have achieved. Also, the light collection optics in this experiment are $f_{\#}3.3$, giving 3 times our scattering angle uncertainty and thus significantly greater "cross-talk" between the parallel and perpendicular measurements that we have obtained. To date, the M.I.T. experiment has found equal-temperature Maxwellians for the longitudinal and azimuthal distributions as we have, but measurements were made only out to about one rather than 6 thermal half-widths.

4. DISCHARGE CONSTRUCTION AND PLASMA PARAMETERS

4.1 The Penning Discharge

The plasma which we study in this experiment is transient, highly ionized, moderately dense and characterized by warm electrons and cold ions. It is created in a pulsed Penning or Phillips Ionization Gage (P.I.G.) type linear discharge operating with two hot cathodes in a low to moderate magnetic field.

The Penning discharge is essentially an electron beam-generated plasma immersed in a magnetic field parallel to the beam, but is distinguished from other such discharges by the magnetron-like guns which produce the beam. Figure 3, which shows the construction of one of our cathode-anode assemblies, may be used to illustrate the basic principles of a Penning electron gun, although we should note that many quite different designs are used.

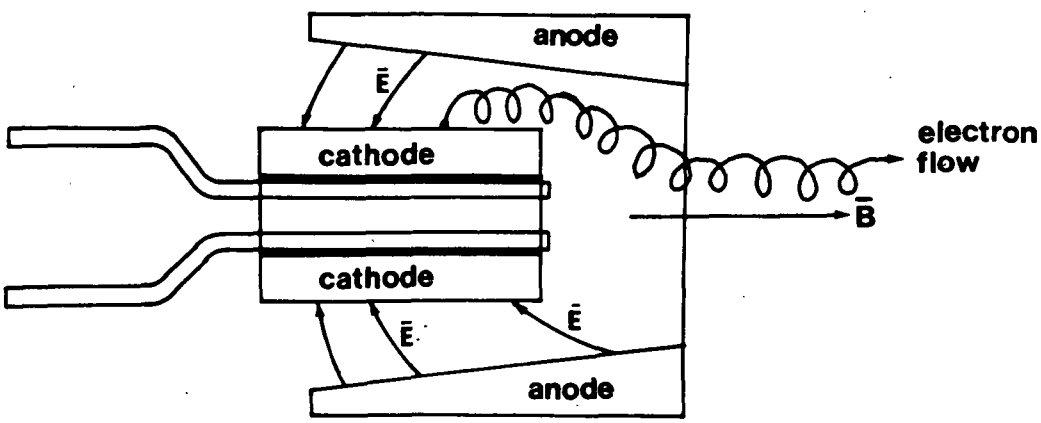

Figure 3
Construction of PIG Gun Assembly

A large electric field with both radial and axial components is impressed across an annular anode-cathode assembly. The cathode may be thermionic or cold, in which case the intensity of the plasma ion bombardment determines the magnitude of the beam current densities. If

the gun is now immersed in an axial magnetic field B_z, electrons emitted by the cathode in vacuum will be subject to an $\bar{E} \times \bar{B}$ drift with velocity $v_\theta = cE_r/B_z$ (so long as B_z is large enough to keep the gyroradius less than the cathode-anode spacing) and an axial acceleration $a_z = -eE_z/m_e$. The result is an energetic hollow beam in the z-direction. After leaving the gun the vacuum trajectory of the beam electrons will follow the magnetic field lines and may rotate slightly due to the radial self field of the beam. An electrostatic reflector at the opposite end of a discharge tube from such a gun can cause the beam electrons to spiral back and forth along the tube several times before colliding with the anode.

If now neutral gas is introduced to the discharge tube, the primary electrons return to the anode earlier, as the result of electron-neutral collisions. The advantage of this type of discharge is that the primary mean free path is initially determined by ionizing collisions down to neutral pressures as low as 10^{-12} torr.*[66] For this reason, the Penning discharge generates highly ionized plasma over a wide range of density. The primary limit is an upper one which is due to the combined effects of recombination, diffusion and reduced primary range. In our discharge, the upper limit for good ionization efficiency in hydrogen is about 2μ neutral pressure, while the discharge remains uniform to much higher pressures. Of course, the primary range can be many centimeters in a plasma (e.g. $n_e = 10^{13}$, $T_e = 1$ ev, $\lambda_{mfp} = 1.4$ mm) whose thermal particles have very small range, because (a) the primaries can easily have energies of the order 300 volts, and (b) the range in plasma is proportional to energy squared.

*In fact, since collision frequency is proportional to density, the device is particularly useful for measuring low pressures. The Phillips Company first marketed such a gage, hence the name Phillips Ionization Gage or PIG, after F.M. Penning[68] demonstrated the principle.

Hooper[67] gives an excellent review of Penning type discharges. He warns that no adequate theory exists for the PIG discharge, so that the studies which have been done are necessarily semi-empirical. This statement can be made even more strongly for highly ionized thermionic-cathode PIG discharges. The reason for this is the very complicated state of the PIG plasma during the discharge and the associated difficulty of studying the effect of changes in isolated parameters. Strong instabilities and highly non-Maxwellian particle distributions may exist, and these can cause relatively strong electric fields even in fully ionized plasmas. Such electric fields, combined with ordinary density or temperature gradients lead to completely nonclassical particle transport modes across magnetic field lines so that the usual ideas of mobility and diffusion velocity are useless.

4.2 Classical and Anomalous Particle Transport

The behavior of plasma in a magnetic field depends in an essential way on whether or not collisions are dominant. For purposes of discussion, the steady-state fluid equations for electrons and ions may be written[69,70]

$$nm\left(\frac{\partial}{\partial t} + \bar{v}\cdot\bar{\nabla}\right)\bar{v} = nq\left(\bar{E} + \frac{\bar{v}\times\bar{B}}{c}\right) - \bar{\nabla}\cdot(nm\overleftrightarrow{uu}) - nm\nu\bar{v} \qquad (4\text{-}1)$$

where n, m, q are species density, mass and charge, $\bar{v}$ is macroscopic drift velocity and $\overleftrightarrow{uu}$ the stress dyadic, taking account of the neutral component in the case of partially ionized plasma or of Coulomb collisions in fully ionized plasma through the collision frequency ν. If we now look just at situations in which the plasma is isotropic (ignoring viscosity effects) $\bar{\nabla}\cdot(nm\overleftrightarrow{uu}) = \overline{\nabla p}$ and if we ignore quadratic velocity terms, the simpler equation

$$p \frac{\partial \bar{v}}{\partial t} = \frac{\bar{j} \times \bar{B}}{c} - \overline{\nabla p} - nm\nu\bar{v} \qquad (4\text{-}2)$$

results for which a solution may be written for each of the two fluids in terms of their density n and the electric potential ϕ, in the form

$$-\bar{v} = \frac{1}{n} (\overleftrightarrow{D} \cdot \bar{\nabla}) n + (\overleftrightarrow{\mu} \cdot \bar{\nabla}) \phi \ . \qquad (4\text{-}3)$$

With $\tau = 1/\nu$ as a collision time (coulomb or neutral collisions), we have:

$$\overleftrightarrow{D} = \begin{bmatrix} D_\perp & -\omega\tau D_\perp & 0 \\ +\omega\tau D_\perp & D_\perp & 0 \\ 0 & 0 & D_\parallel \end{bmatrix}, \quad \overleftrightarrow{\mu} = \begin{bmatrix} \mu_\perp & -\omega\tau\mu_\perp & 0 \\ +\omega\tau\mu_\perp & \mu_\perp & 0 \\ 0 & 0 & \mu_\parallel \end{bmatrix}, \qquad (4\text{-}4)$$

where $\overleftrightarrow{D}$ and $\overleftrightarrow{\mu}$ are the diffusion and mobility tensors, respectively, in a coordinate system in which magnetic field $\bar{B}$ lies along the third or z-axis and is assumed homogeneous. Further ω is the species gyrofrequency given by $\omega = \frac{-qB}{mc}$. We have written this formalism in order to show the transition from collision-dominated to collisionless diffusion and mobility. This transition is accomplished by the substitution

$$\eta = \frac{m}{nq^2\tau} \qquad (4\text{-}5)$$

for the resistivity of a fully ionized plasma. The diffusion coefficients for the two cases are as follows:

	collision dominated	collisionless ($\omega\tau \gg 1$)
$D_{\parallel}$	$\frac{kT\tau}{m}$	$\frac{kT}{nq^2\eta}$ *
$D_{\bar{E}\times\bar{B}}$	$\pm \omega\tau D_{\perp}$	$\pm \frac{kTc}{qB}$
$D_{\perp}$	$\frac{D_{\parallel}}{1 + (\omega\tau)^2}$	$\frac{c^2 kTn\eta}{B^2}$

(4-6)

The mobilities are obtained by making the formal substitution $kT \rightarrow q$.

Considerations such as these lead to the statement that classical diffusion across magnetic field lines in a fully ionized plasma is proportional to $1/B^2$. However, in this form it is also easy to see that enhanced diffusion at the rate $1/B$ can also occur if there are significant electric fields present in the plasma in the direction perpendicular to $\bar{B}$. Relatively large electric fields (several volts/cm) can exist in ordinary laboratory plasmas, due to ordinary particle transport and instabilities, ignoring sheaths for the moment. In fact, recent results[72] show that such fields may be the rule rather than the exception.

In early plasma experiments, an attempt was made to distinguish between "classical" diffusion and the (1/B)-proportional diffusion which was first seen empirically and labeled "Bohm diffusion". In fact, Bohm suggested that[71] the appropriate perpendicular diffusion coefficient should be $D_{\perp} \sim \frac{kTc}{16qB}$.

4.2.1 Plasma Instabilities in the Penning Discharge

The formal similarity between the Bohm diffusion coefficient and the Hall coefficient $D_{\bar{E}\times\bar{B}}$ in the collisionless case shows the practical importance of self-induced electric fields in a plasma. In fact, in a

*Diffusion along the magnetic field is normally not defined, but the corresponding mobility $\mu_{\parallel} = \frac{1}{nq\eta}$ is.

cylindrical plasma, an azimuthal electric field due to charge separation would produce such a diffusion in the radial direction.

Such considerations led Kadomtsev and Nedospasov[73], Hoh[74], Guest and Simon[75] and others to develop a theory for "anomalous" diffusion featuring an instability known as the flute, screw, $\overline{E} \times \overline{B}$ or neutral drag instability. The model chosen was the Penning discharge in most cases, because of (a) the possibility of balanced longitudinal electron and ion currents (no net axial current), (b) the presence of a strong homogeneous longitudinal $\overline{B}$ field, (c) the presence of strong radial electric fields, and (d) the existence of much experimental data showing both enhanced diffusion and evidence of rotational instabilities of the type discussed in such devices. In such a discharge, the radial electric field E_r drives both electrons and ions azimuthally at the velocity $v_{E\times B} = E_r c/B_z$. In these early theories, a weakly ionized plasma was considered so that the neutral drag, that is the differing mobilities for electrons and ions colliding with neutrals, causes azimuthal charge separation when the plasma is attempting to move at this drift velocity. This charge separation generates an azimuthal electric field, which combined with a radial density gradient can grow arbitrarily large above a critical value of magnetic field. This electric field, of course, is all that is required to drive large quantities of particles radially outward, yielding enhanced diffusion.

If, as in our case, the degree of ionization is high, Hoh and Lehnert[76] have shown that the screw instability still occurs quite readily, with a new charge separation mechanism due to the combined effects of net longitudinal current flow and collision-dominated ions. Ion collisions with the plasma tube wall resulting from large ion gyroradius can produce this effect.

Other instabilities caused by finite resistivity or plasma density

gradients are undoubtedly present in the highly ionized Penning discharge, and can be responsible for the enhanced transverse particle loss rates that have been observed. Experimentally, the discharge at moderate and high densities operates in two basic modes. Below a critical magnetic field of the order of 200 gauss, classical or at most Bohm diffusion is observed. Above this field, the particle loss rate typically increases with increasing magnetic field[77,78,79]. This is not even diffusion any longer, but the expulsion of particles due to strong instabilities whose quantitative prediction has been impossible to date.

In the region below the critical field, in which most of our scattering measurements are reported, the plasma is reasonably quiescent but may well have nonthermal distributions of electron velocities. We have felt that an experiment would be of interest which could determine whether or not the electron velocity distributions in the quiescent PIG discharge are Maxwellian, and whether significant anisotropy exists between the azimuthal and longitudinal distributions.

4.3 Properties of our Penning Discharge

We operate a discharge (see Figure 4) with two opposed hot cathode Penning electron guns at either end of a pyrex discharge tube approximately 1 meter in length and 7.6 cm in diameter. The discharge is run in a pulsed fashion in hydrogen, at pressures between 0.5 and 2 microns.

Hydrogen was selected because of the absence of line radiation in its spectrum over the possible range of scattered radiation wavelengths, and because of the simplicity of the atom (see Chapter 5).

In the central region of the discharge tube, a blackened stainless steel scattering chamber is inserted to allow connection to stray-light trapping chambers which will be discussed later. All metal parts are allowed to float electrically to avoid interference with the Langmuir probe.

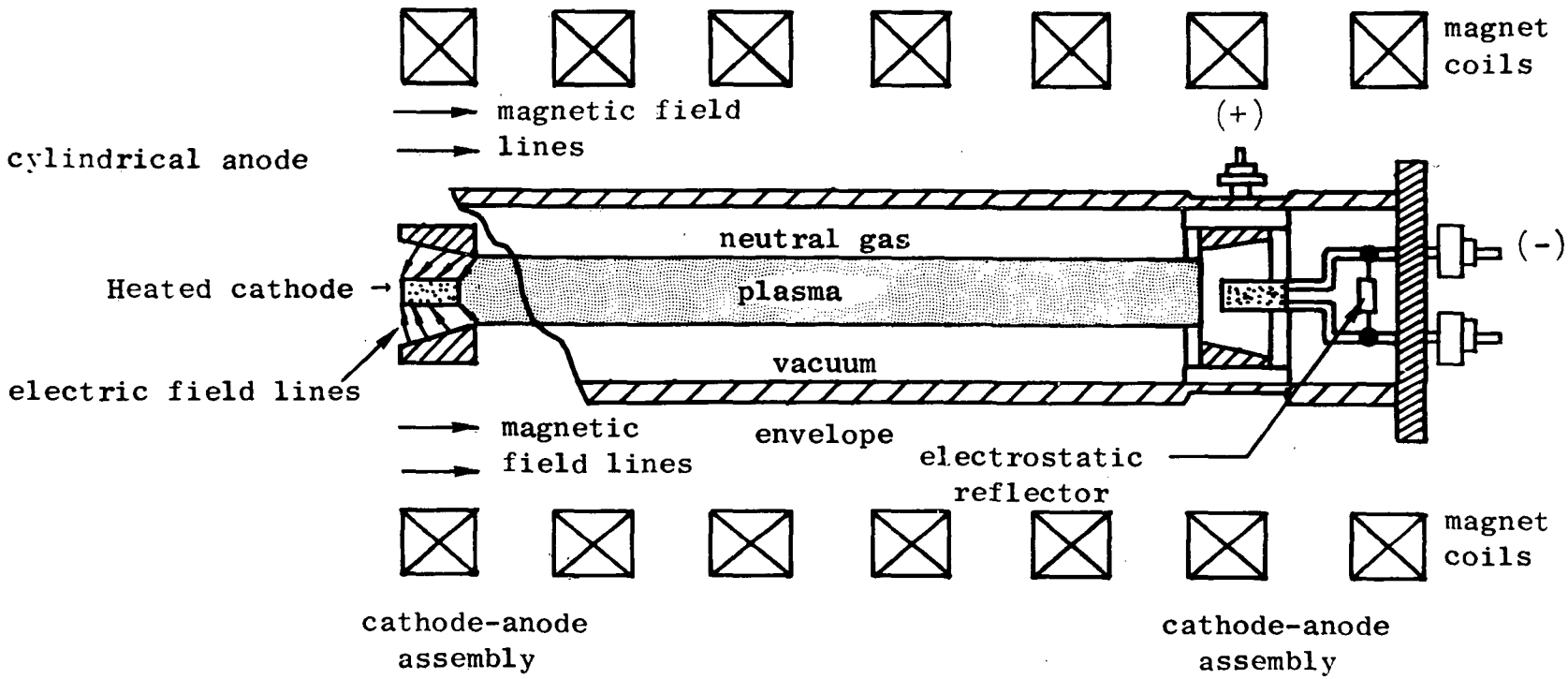

Figure 4

Construction of the PIG Discharge

The electron guns are as in Figure 3, and consist of a 2 cm diameter resistively heated cylindrical oxide-nickel mesh cathode of total surface area 30 cm^2, surrounded by a 3 cm diameter water-cooled anode sleeve and backed by a tantalum disc reflector at cathode potential. Each gun is capable of pulse currents up to 300 amps, temperature limited.

Gas enters at one end through a calibrated leak and is pumped out the other, however at such a low flow rate, about 2 liter/sec, that pressure differentials along the discharge tube are not significant. Impurity levels from virtual and real leaks remain less than 0.01 micron-liter/sec.

Typical operating parameters are: density $n_e = 2 \times 10^{13}$ cm^{-3}; $T_e = 5$ ev; $T_i = 0.5$ ev; Debye length $D_e = 5\mu$; magnetic field strength B = 190 gauss; relative ionization $\rho = 75\%$; $\omega\tau_e = 175$; electron mean free path $\lambda_e = 2$ cm, discharge duration = 250 μsec. With even a moderate magnetic field (50 gauss), the plasma forms a fairly well defined column with roughly rectangular radial density profile and outer radius slightly greater than the anode ring radius.

The discharge is operated from a vacuum-tube pulser whose own temperature-limited output provides stabilization for the discharge current and a nearly rectangular current wave form into the electron guns. The rapid shutdown of the excitation allows afterglow measurements to begin immediately.

Since the longitudinal resistivity of our discharge plasma is comparable to that of carbon, the main part of the plasma is a highly ionized positive column whose potential is within a few tens of volts of the anode potential. Most of the discharge voltage appears across a cathode fall region which is the main mechanism for primary electron injection in this operating mode. To facilitate probe measurements, the discharge is operated with anode grounded.

A typical plot of electron density and temperature vs time at the center of the plasma column is shown in Figure 5. In this figure, time begins at the end of the discharge pulse, which has been going on for 200 μsec prior. These measurements were made by Langmuir probe, and the density measurements have been verified by microwave interferometry. Conditions were as near as possible to those used in the actual Thomson scattering measurements to be reported.

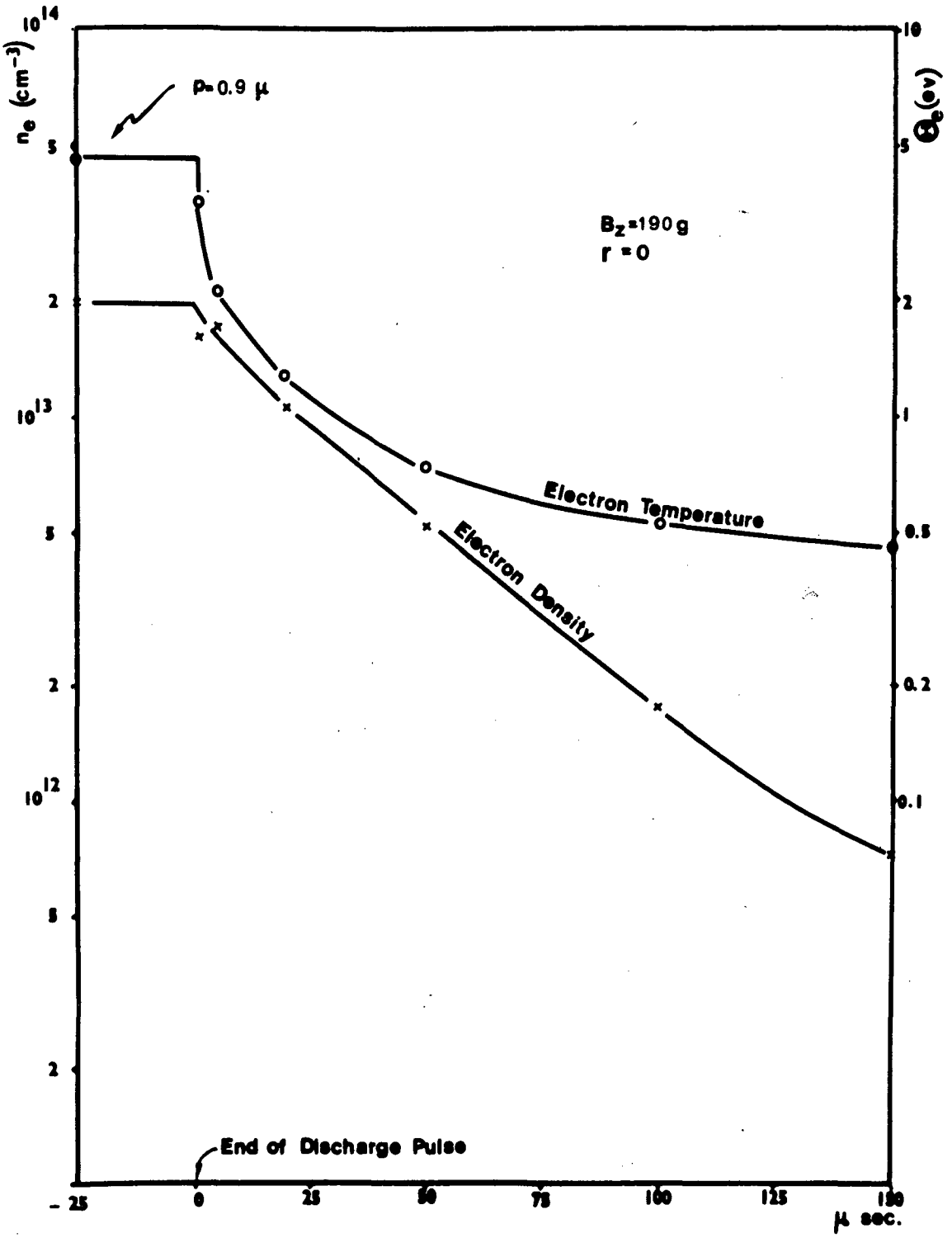

Figure 5

Electron Density and Temperature vs Time at End of Discharge Pulse (Langmuir Probe)

5. THE EXPERIMENT

5.1 Orientation

Figure 6 is a plan view of the main part of the scattering apparatus, showing just the mechanical arrangement of the Penning discharge, magnets, light ports and scattering chamber. Figure 7 is a complementary diagram, showing only the optical arrangement used. Both should be viewed in conjunction with the wide angle photograph of the completed experiment, Figure 8.

The Penning discharge assembly is the structure which threads the magnet coils from left to right in Figure 6. Its overall length is 1.8 meters; the plasma column itself is 1.0 meters long.

Attached to the Thomson scattering chamber in the central region of the discharge are three stray light trapping baffle tubes (see section 5.3), part of the vacuum system, at angles of 60° to the plasma axis. These convey the laser beam through the scattering region in either of two directions $\bar{k}_{i1}$ or $\bar{k}_{i2}$, and the scattered light to its detection system. The short section on the fourth flange of the scattering chamber is a viewing dump, which is a "black hole" designed to provide a proper background against which to view scattered light. The beam focussing and viewing lenses (L_3, L_4 and L_5 in Figure 7) are located just outside the windows of the three baffle tubes. The top of our Langmuir probe is seen in the center of the scattering chamber.

The scattering angle between incident and scattered wave directions is seen to be either 60° or 120°, depending upon which illumination direction is used. This choice of angles is primarily dictated by mechanical constraints (permissible field coil locations). Actually, any combination of angles such that $\theta_1 + \theta_2 = 180^{\circ}$ with the discharge axis bisecting the angle between illumination and scattering axes would serve to give the

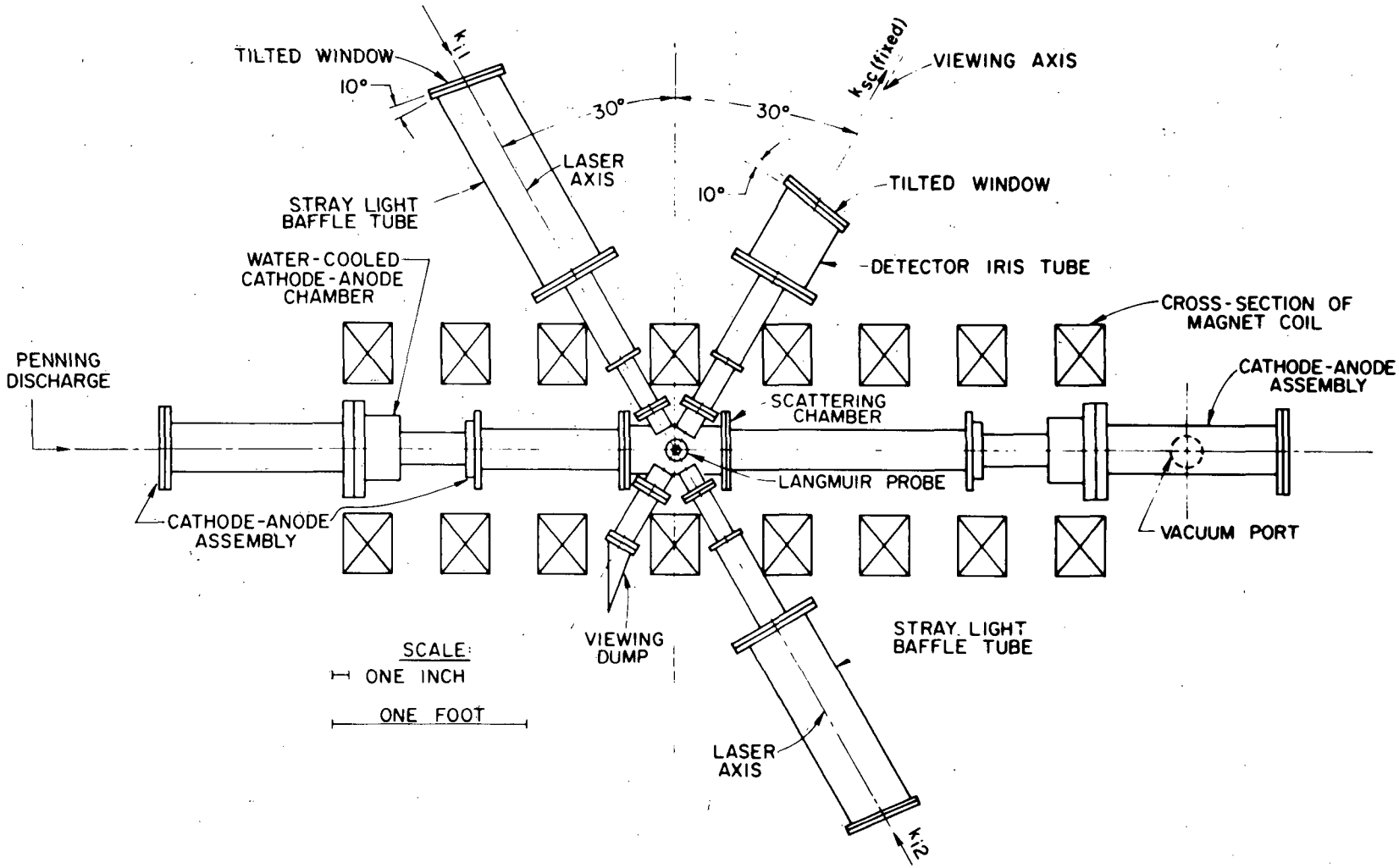

Figure 6

Schematic View of Scattering Experiment from Overhead (Optics Removed)

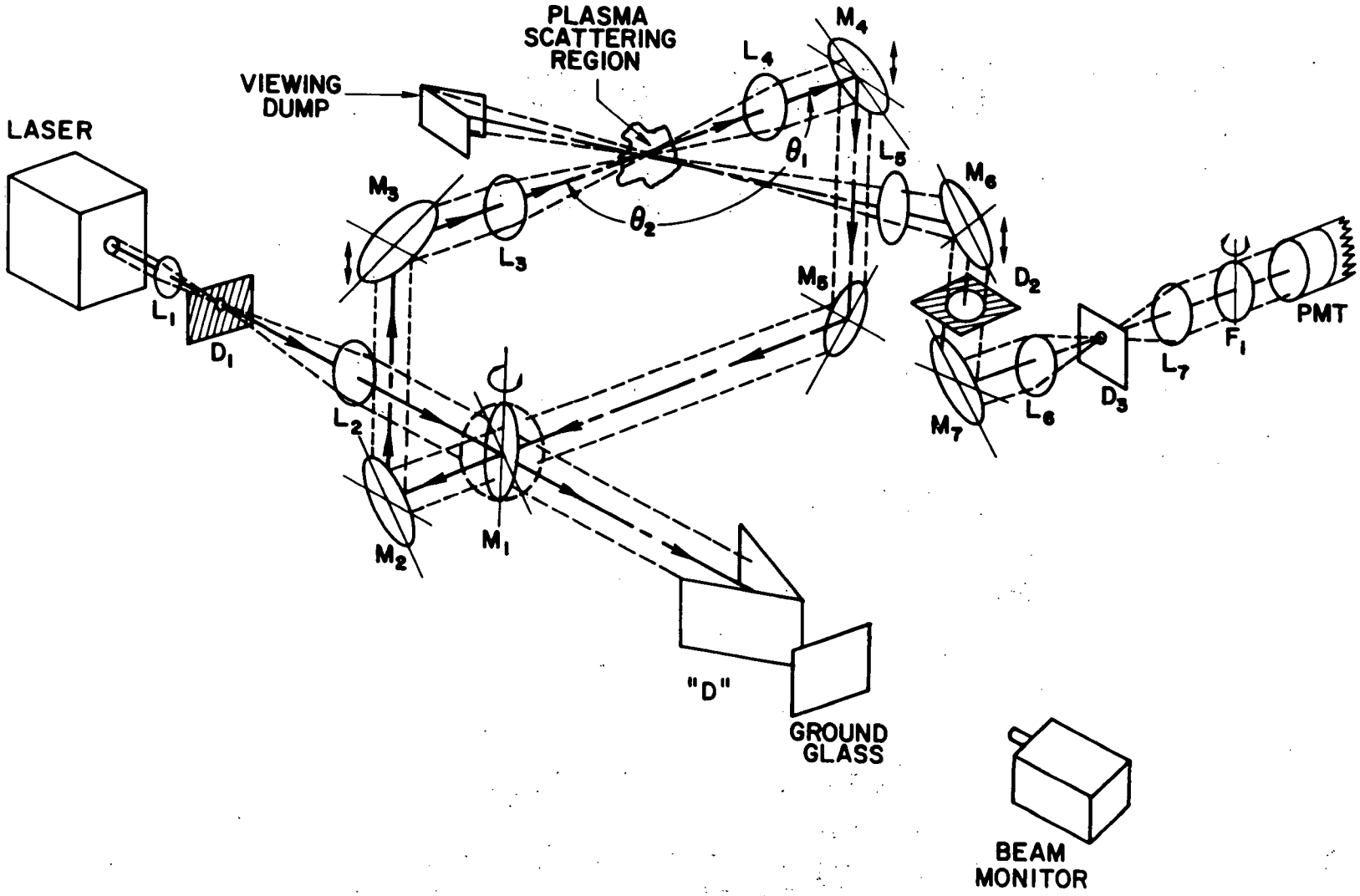

Figure 7

Schematic View of Illumination and Detection Optics

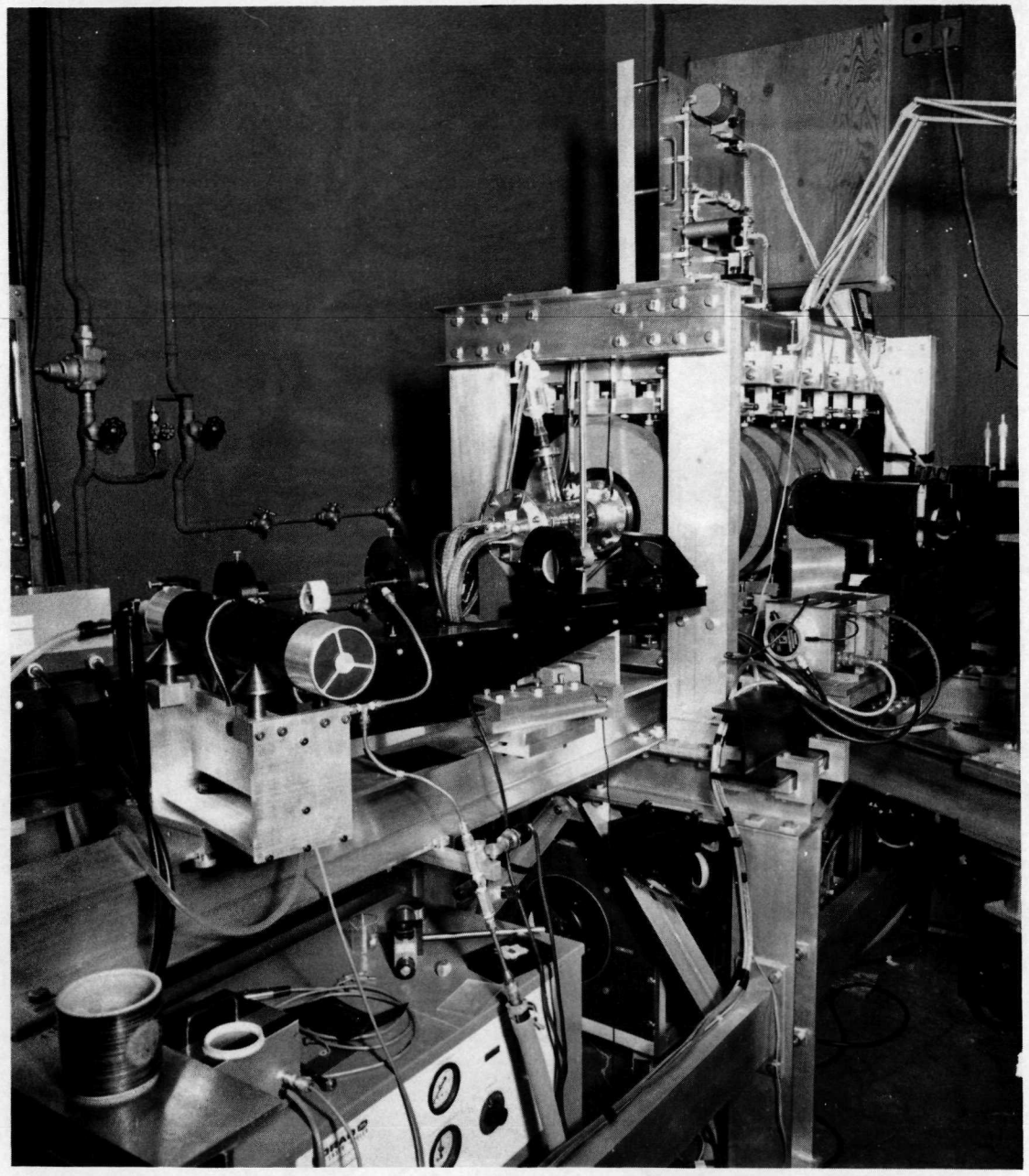

Figure 8

Wide Angle Photograph of Experiment

necessary sensitivity directions $\bar{k}_\perp$ and $\bar{k}_\parallel$ for measuring azimuthal and longitudinal velocity distributions (see Figure 2). The parameter α in the two directions is, respectively, of the order 0.03 to 0.02 during the discharge.

We could equally well have used a fixed illumination direction and two observation ports. The advantage of doing so is measurement simultaneity. The disadvantages are the cost of duplicating the scattering detection system, including spectrometer and photomultiplier, and, more important, the fact that relative errors due to miscalibration of the detection systems would add rather than cancel. In this experiment, both the laser and tne plasma are highly reproducible from shot to shot over long periods of operation, so we may use the single port method.

5.2 The Laser Light Source

The light source for our scattering experiment must meet several requirements, some of which are unusual for commercial equipment. The most obvious of these are sufficient energy and spectral energy brightness (energy per unit wavelength, area and solid angle). By rewriting equation (2-5) in terms of the differential Thomson cross-section and scattering length ℓ, we see that the minimum illumination energy required to produce at least N_{sc} scattered photons in detector solid angle $d\Omega$, and bandwidth $d\omega$ at doppler frequency ω is

$$L_o(\omega) = \frac{h\nu_o N_{sc}}{n_e \ell \left(\frac{d^2\sigma_T}{d\Omega d\omega}\right) d\Omega d\omega} \text{ joules} . \qquad (5\text{-}1)$$

More specifically, if we assume a Maxwellian, nonrelativistic plasma, we can use equations (2-20)' and (2-27) to calculate the cross-section and the required illumination energy at the center of the electron feature

spectrum in the scattering plane ($\alpha \ll 1$, $\omega = 0$, $\sin\Psi = 1$). This gives:

$$L_{oe} \cong \frac{\sqrt{\pi}\ hc}{r_o^2} \left(\frac{N_{sc}}{\lambda_o n_e \ell d\Omega} \right) \frac{\omega_e}{d\omega} \text{ joules} . \qquad (5\text{-}2)$$

Since, in any experiment of this type, the detector bandwidth will be determined with resolution of the thermal doppler width of the scattered feature in mind, we replace $(\omega_e/d\omega)$ by a constant R indicating the resolving power. Then, in practical units for this problem (wavelength in microns, density in 10^{12} cm^{-3}, energy in joules) we find:

$$L_{oe} \cong 4.4 \times 10^{-6} \left(\frac{R\ N_{sc}}{\lambda_{o\mu} n_{el2} \ell d\Omega} \right) \text{ joules} \qquad (5\text{-}2a)$$

for the minimum electron feature energy.

The same procedure for the ion feature ($\alpha \gg 1$) with $R = \frac{\omega_i}{d\omega}$ gives:

$$L_{oi} \cong \frac{1}{Z} \left(1 + Z \frac{T_e}{T_i} \right)^2 L_{oe} . \qquad (5\text{-}2b)$$

Stated in this way, the single number N_{sc} implicitly includes any necessary calculations of transmission loss and signal-to-noise ratio in the detection system.

As explained in Chapter 6, the only noise we have to deal with is statistical noise due to the discreteness of the tiny electrical signal present in the first stage of light detection. However, even with multiple measurements under the most favorable noise conditions, a practical minimum for this signal at the 1/e point of the electron feature spectrum is 10 electrons, or 27 at the spectrum center. Assuming a probability of 0.07 for conversion of a photon into a photoelectron at the detector and an average optical transmission of 0.20 for the detector optics within the pass band we require $N_{sc} = 1{,}930$ photons.

The typical parameters for the experiment we plan are $n_{el2} = 20$, $\lambda_{o\mu} = 0.694$, $d\Omega = 0.01$ sr, $R = 10$ and $\ell = 0.8$ cm, so that the required illumination energy is 0.77 joules.

The foregoing is precisely the reverse of our actual design procedure, but equation (5-2) provides a particularly useful way of looking at the energy requirements of a scattering experiment.

While an ordinary light source could supply this amount of energy, only a laser source has the necessary brightness and monochromaticity. The monochromaticity requirement arises from the fact that the illumination energy must all lie in a band smaller than the spectral resolution desired.* Usually, the most difficult part of this limitation is achieving an absolute stability of the illumination spectrum center wavelength commensurate with the permitted bandwidth. Brightness is needed because the beam solid angle and focal spot size both must be small enough to satisfy obvious bounds on incident beam direction uncertainty, and spacial resolution in the scattering volume. Further, the brightness of the illuminated plasma should exceed its natural brightness within the scattered spectrum. As an example, the spectral energy brightness of the laser used in our experiment is about 4×10^6 joules/sr-cm^2-Å.

Up to this point, we have deliberately avoided mentioning power or time duration. In our experiment, rapidly varying plasma parameters require a measurement interval of 1 microsecond at most. In any case, it is seldom desirable to obtain the required illumination energy over a long measurement interval at low power because of the complicated apparatus required to elicit the scattering signal when it is deeply

*The resolution needed is a few Angstroms in an electron feature experiment, or a few tenths Å in an ion feature experiment.

buried in noise. At present, commercial lasers designed for continuous operation feature power levels six orders of magnitude below that of Q-switched lasers, requiring plasma stability over a correspondingly longer period. In short, nothing can match the joy that comes from having a real signal-to-noise ratio of 20 db!

The source of illumination for our scattering experiment is a Korad model K1-Q Q-switched ruby laser, specially modified for spectral purity. The laser cavity was set up to produce a 25 to 30 nanosecond, 1.5 joule flash of light at 6943 $\mathring{A}$, about 50% of the maximum available Q-switched energy. Typical intensity in the 0.95 cm diameter output beam is 60 megawatts/cm^2. With these operating parameters, the laser can be fired ten times a minute, and the critical cavity parts have a life expectancy of about 50,000 shots.

Other characteristics of the laser output are: beam divergence, 3.0 milliradians for 95% beam energy; center wavelength uncertainty and spectral width, 0.03 $\mathring{A}$ or 2 Ghz, greater than 95% linear polarization and 3% standard deviation of the light pulse energy from shot to shot at 10 shots per minute. The resulting source spectral brightness is about 1.5×10^{14} watts/sr-cm^2-$\mathring{A}$.

The low bandwidth was achieved by the use of commercial resonant Fabry-Perot etalons for front and rear cavity reflectors. The reflectivity of each etalon is a comblike function of wavelength, having several maxima and minima within the wavelength interval for appreciable gain in the ruby rod, but the spacing between the teeth is slightly different for the two combs. By tuning one etalon relative to the other, their reflectivities can be made to reinforce significantly in a single narrow cavity gain maximum corresponding to only five or six longitudinal modes. In our laser, the rear etalon is fixed, while the output etalon may be temperature tuned. Correct adjustment of the etalons for narrowband

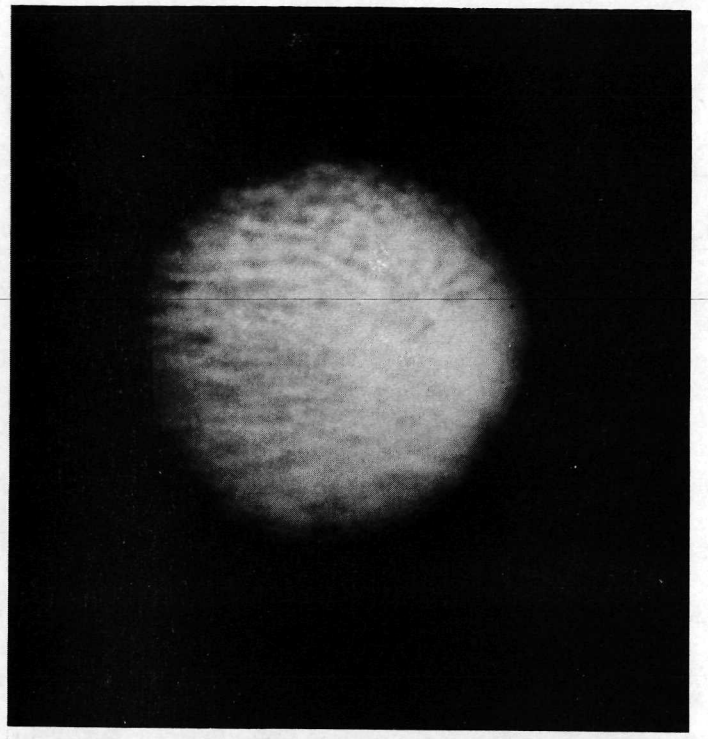

Figure 9a
Laser Beam Pattern, z = 3 meters

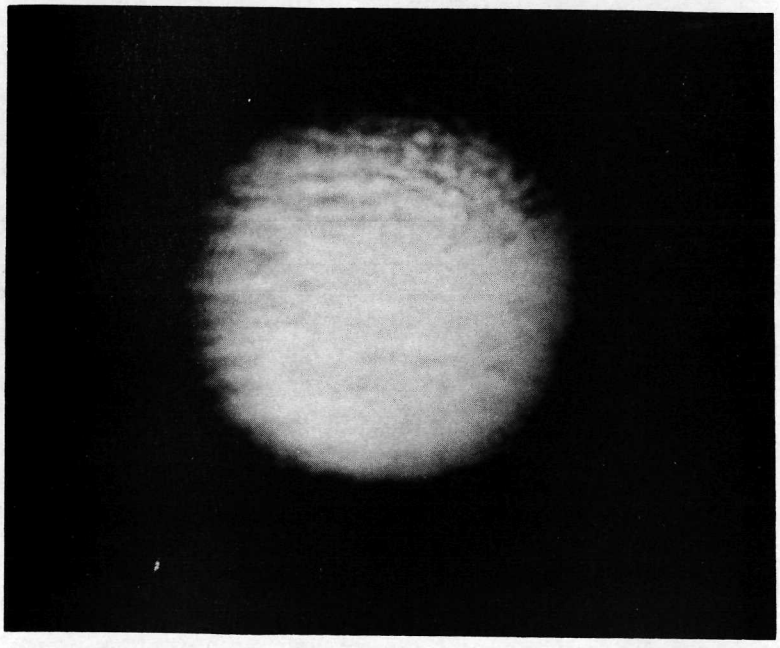

Figure 9b
Laser Beam Pattern, z = 5 meters

operation was verified with a spectrum analyzer, using measurement ranges of 1.20 Å, 0.24 Å, and 0.06 Å.

The laser's excellent output energy stability is due mainly to accurate control of lamp input energy through the use of oil-filled (rather than electrolytic) energy storage capacitors and well-designed capacitor charging circuitry. In addition, the flashlamp and ruby rod are water cooled, with ± 1°F regulation. This is important for stability of output power, energy and wavelength and for low beam divergence. Uncontrolled heating during the flashlamp pulse can easily cause output wavelength shifts of 1 or 2 Å in ruby and, with the natural temperature dependence of ruby gain plus the wavelength-dependent cavity gain with mode selection, very erratic output power. Heat also causes significant changes in beam divergence due to warping of the ruby. The same cooling system is used to control the output etalon temperature.

Another advantage of the laser head design for our purposes is the use of a helical flashlamp and diffuse lamp cavity reflectors, which results in unusually uniform pumping of the ruby. This is demonstrated in Figure 9 which shows actual photographs of the laser beam pattern on ground glass, after it has traveled 3 and 5 meters, respectively. Even at these distances, the beam diameter shows no appreciable increase. The beam expander used to achieve this degree of collimation is discussed in the following section.

5.3 Plasma Illumination Optics

The laser light output is sent through a 5X beam-expanding collimating telescope, $L_1 D_1 L_2$ in Figure 7. The function of this device is to reduce both the beam divergence and power density of the beam, while eliminating laser pump light and other stray radiation outside a narrow forward cone.

The telescope has an effective f-number of 10.0, chosen to permit rapid collimation with simple lenses. Lens L_1 focuses the laser energy on a 0.55 mm diameter spot in the center of D_1, which is a sharp-edged 0.95 mm diameter pinhole in 0.005" tantalum sheet. The power density at the focus is of the order of 40 gigawatts/cm^2, so the pinhole was deliberately made too large to absorb a significant amount of the main beam energy. Instead, all radiation in a cone of half-angle 4.9 milliradians (roughly $1/4^o$) about the forward direction is transmitted. The laser beam waist in the plasma is then determined by considerations other than the size of D_1.

As pointed out by Evans and Katzenstein[48], such focal power densities are sufficient to cause a spark in air, which would absorb and scatter a large and unpredictable amount of the beam energy. This is cited in their paper as being a basic difficulty with fast collimation, but we have found that evacuating the focal region to about 5 microns solves the problem.

After expansion and collimation, the beam has a diameter of 4.75 cm, the divergence has been reduced to 0.6 milliradians for 95% of beam energy, and the average power density is only 3 megawatts/cm^2. Overall transmission of the collimator for the raw laser beam is 69%. This power level has proved quite safe for the multilayer dielectric coatings used for mirror and antireflection surfaces in the laser beam optics. Further, the very low expanded beam divergence allows us to work with an essentially constant diameter beam throughout the experiment, which greatly simplifies handling of stray laser light.

The collimated laser beam next passes to the double-sided mirror M_1, which can be rotated to direct the beam through the plasma scattering region either along the path shown in Figure 7, or in the reverse direction.

Because of the symmetric train of optics M_3L_3, L_4M_4, the beam is focussed on the same volume of plasma for either incidence direction, to within a maximum misregistration of ± 0.5 mm. In the scattering region, the laser beam is vertically polarized. The beam waist diameter in the focal region is intended to be 1.0 mm for 95% of the beam energy, and has been deduced from measurements of the Rayleigh scattering intensity profile at the focus to be 0.95 ± 0.05 mm. The resulting energy density in the scattering region is then, typically, 150 joules/cm^2. The amount of plasma heating expected at this energy density will be discussed in Chapter 6.

It should be mentioned here that the effective f-number of the focussing lenses is completely determined by the desired beam waist diameter for a beam of known etendue (the product of illuminated solid angle and beam cross-sectional area). For example, our laser has an inherent etendue $\Phi_o = 1.94 \times 10^{-5}$ sr-cm^2 which gives an empirical relationship $d_\omega = 5.62 \times 10^{-3} f_\# \text{ cm}$ for the waist diameter. This was the primary reason for picking an f-number of 15 for these lenses, although this choice incidentally results in a quite acceptable contribution of 2^o to the standard deviation of the scattering angle. The one degree of freedom which exists is the expansion ratio of the beam collimator, which, when chosen determines the focal length of L_3 and L_4. Our ratio of 5.0 results in a 71 cm focal length, which is a desirable figure from scattered light considerations.

In order to scan the scattering region across the plasma column, we chose a very direct method in which mutually calibrated, parallel-axis micrometer drives allow simultaneous vertical translation of the mirror-lens assemblies M_3,L_3 and M_4,L_4 for the laser beam, and M_6,L_5 for the detected beam. A total translation of 3.8 cm is permitted.

All lenses and windows in the laser optical train are made from objective quality "Vycor" glass for thermal stability and uniform refractive index and have a surface figure accurate to within one wavelength of sodium "D" light. They also have a resonant multilayer dielectric coating which reduces the maximum reflectance at each surface to 0.1% at the laser wavelength. All mirrors are borosilicate glass flat to 1 wave per inch and provided with a resonant multilayer dielectric reflecting coating. For light at the laser wavelength, incident at 45° to the surface normal, these mirrors provide a reflectivity of at least 99.9% (see Figure 10). However, they are relatively transparent to light of substantially different wavelength, and so enhance rejection of laser pump light..

As a result, at least 98% of the laser light output at the collimator succeeds in passing through the experiment and bouncing off the second surface of M_1 into the beam dump.

The dump is a wedge constructed of two plates of Schott BG18 red absorbing glass, one piece intersecting the beam at the Brewster angle and the other parallel to and outside the beam. About 5×10^{-5} of the incident light is transmitted to the beam monitor photodiode by the Brewster plate, giving an electrical signal which is integrated to determine the relative energy of each laser pulse.

This is a somewhat unusual approach in that the laser light is absorbed far from the scattering region, and in such a way that return scattered light from the dump is effectively eliminated by geometry. The remaining sources of equipment scattered light at the laser wavelength are then the mirror-lens pairs M_3L_3 and the adjacent scattering chamber windows, shown in Figure 11.

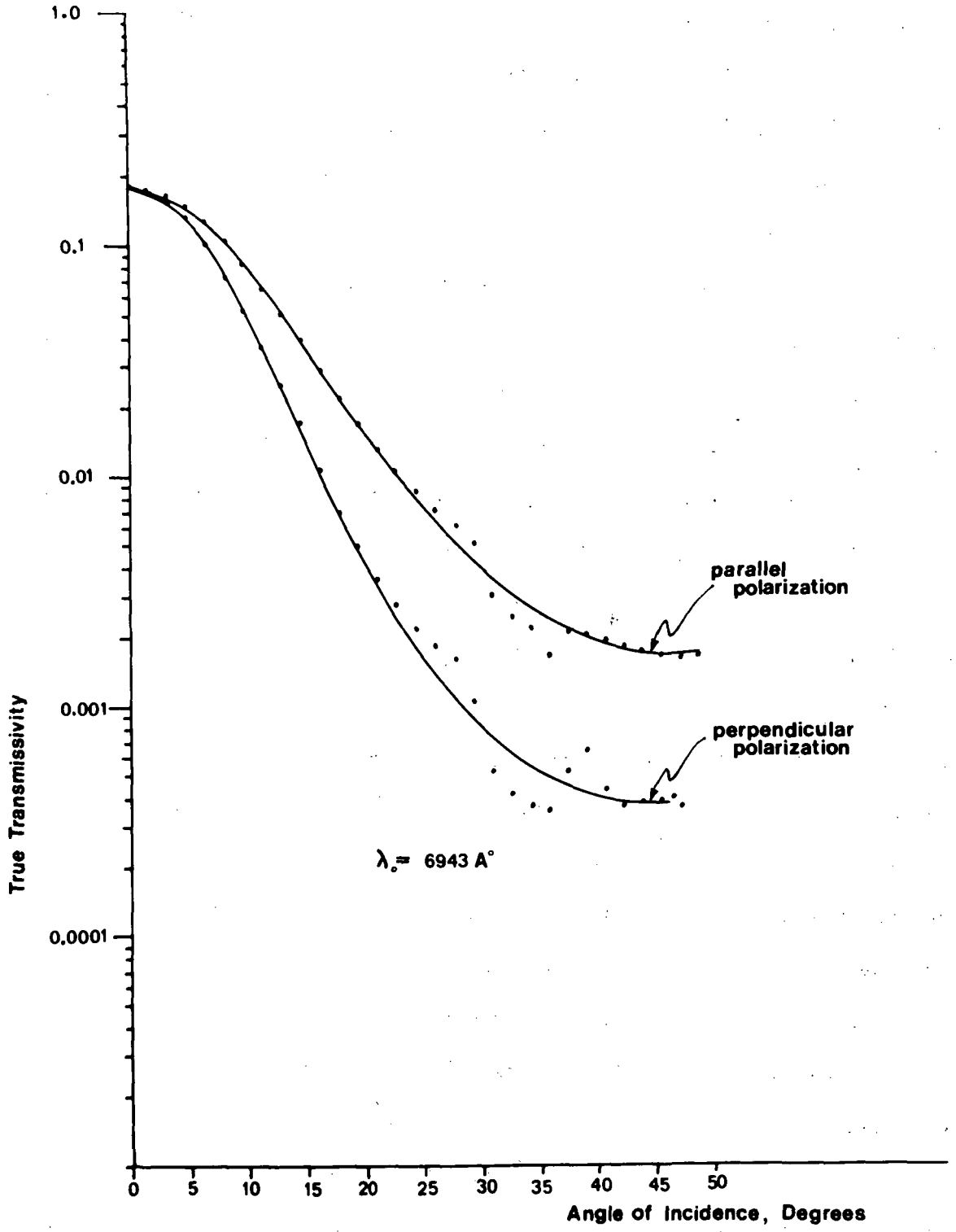

Figure 10

Typical Mirror Transmissivity vs Incidence Angle at 6943 $\mathring{A}$

5.4 Stray Laser Light

The scattered light spectrum in this experiment has a total intensity of the order of 10^{-14} of the illumination intensity because of the modest electron density and the small range of scattering angles we are permitted to use. For this reason a source of noise at the laser wavelength is laser light diffuse-scattered into 2π sterradians by the optical elements closest to the plasma and again scattered into the detection optics by the equipment itself. Even if the spectrometer has a rejection ratio* of 10^5, it cannot adequately discriminate against such light that has not already been reduced to 10^{-9} or so of the incident light level.

Figure 11 shows the internal construction of the stray light baffle tubes which accomplish a major part of the trapping. A similar but shorter baffle tube is used at the scattered beam port (see Figure 6).

In essence, these tubes are evacuated, rough-collimating light ports with perfectly black walls. The trick is to make the walls "black", at least for red light. This is accomplished by a telescoping series of thin, shiny black irises and light-tight spacers within each tube. The aperture of each iris is oblong and just slightly larger than the local cross-section of the collimated beam, allowing for beam translation. The frequency of irises along the beam axis is determined geometrically by the requirement that any uncollimated ray originating within the beam volume at the entrance window, or at points more distant from the beam focus, will be trapped by multiple reflections between adjacent irises.

*The "rejection ratio" of a band-pass filter is defined as the ratio of light transmitted at the point of peak transmission to that transmitted at adjacent frequencies where the filter is supposed to have zero transmission. For grating monochromaters, this ratio is seldom greater than 1000.

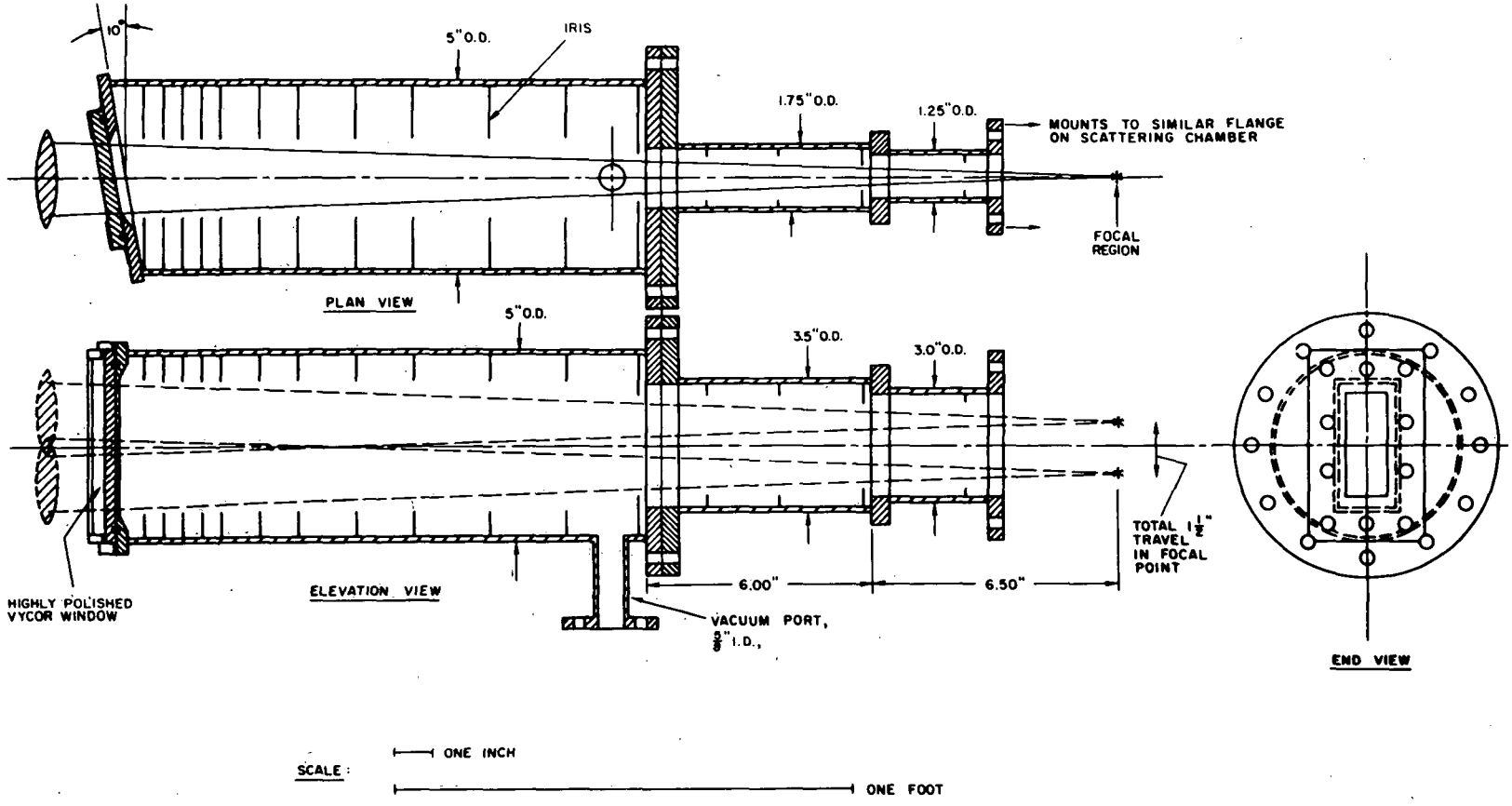

Figure 11

Internal Construction of Stray Light Trapping Tubes

Typical rays will be attenuated by 6 or 8 orders of magnitude before escaping from the wall region.

This technique depends upon the use of specular rather than diffuse iris and spacer surfaces. An ordinary "flat black" surface would scatter a significant portion of the stray light back into the focal region at the first encounter. Of course, the entrance windows must be tilted slightly out of the plane perpendicular to the tube axis, so that the small amount of properly collimated light specularly reflected from their surfaces may also be trapped.

Because the baffle tubes communicate directly with the Penning discharge, considerable effort was necessary to find a shiny black coating for their internal parts which would not outgas. We have developed a sequence of surface treatment procedures which permit the use of commercial paints for this purpose, achieving an outgassing rate of 0.005 micron-liter/sec per square meter of surface at room temperature. System partial pressure due to paint is about 3×10^{-7} torr. In addition, a very small amount of auxiliary pumping is done on the baffle tubes to maintain a net gas flow away from the scattering region.

Beyond merely trapping stray light, the entire experiment has been designed to reduce stray light flux by taking advantage of the inverse square law wherever possible. We have mentioned the use of a distant laser beam dump. Similarly, light from the laser head must travel approximately 3.5 meters through 5 right-angle turns and a 12.5° deviating prism (not shown in Figure 7) before entering the laser beam port.

Probably the most important measure of this type has proved to be locating the laser beam port windows 70 cm from the scattering region. The aperture next to the plasma in each of these ports then intercepts only 1.3×10^{-4} of the light scattered from a point in the entrance pane.

It might appear that nothing could be gained in this way, since we are dealing with fixed beam f-numbers for which the illuminated window area increases as the square of the distance from the focus. However, it should be remembered that the scattered intensity at the window is proportional to the incident intensity, and that both decrease as the distance squared, leaving a total scattering from the window which is independent of its location.

In fact, if we are to believe the military specifications[80] for optics, which treat only gross imperfections such as scratches and bubbles, a piece of given quality should have a per unit area scattering cross-section which actually varies inversely with the diameter of the piece, leading to an even greater stray light reduction!

The final surface which must receive careful attention to achieve a low stray light level is the background against which the scattering is viewed. If this surface (the "viewing dump") returns no light at all to the detector, we have achieved our purpose. The original model for a viewing dump is called a Rayleigh horn, after its inventor, and is just a hollow cone of black glass, curved into a horn-shape so that the point cannot be seen when looking at the inside. Its blackness depends upon the absorption of stray light in multiple specular reflections between highly polished black surfaces in much the same way as did light trapping in the baffle tubes.

However, a Rayleigh horn would be large and awkward in this experiment, so a simple wedge like the laser beam dump is used, but with a smaller dihedral angle of 20° between the Schott BG18 glass plates. As illustrated in Figure 12, 8 or 9 bounces are required for stray light to enter the viewing beam. The line of intersection of the wedge plates is out of sight of the detector. Further, the top and bottom of this

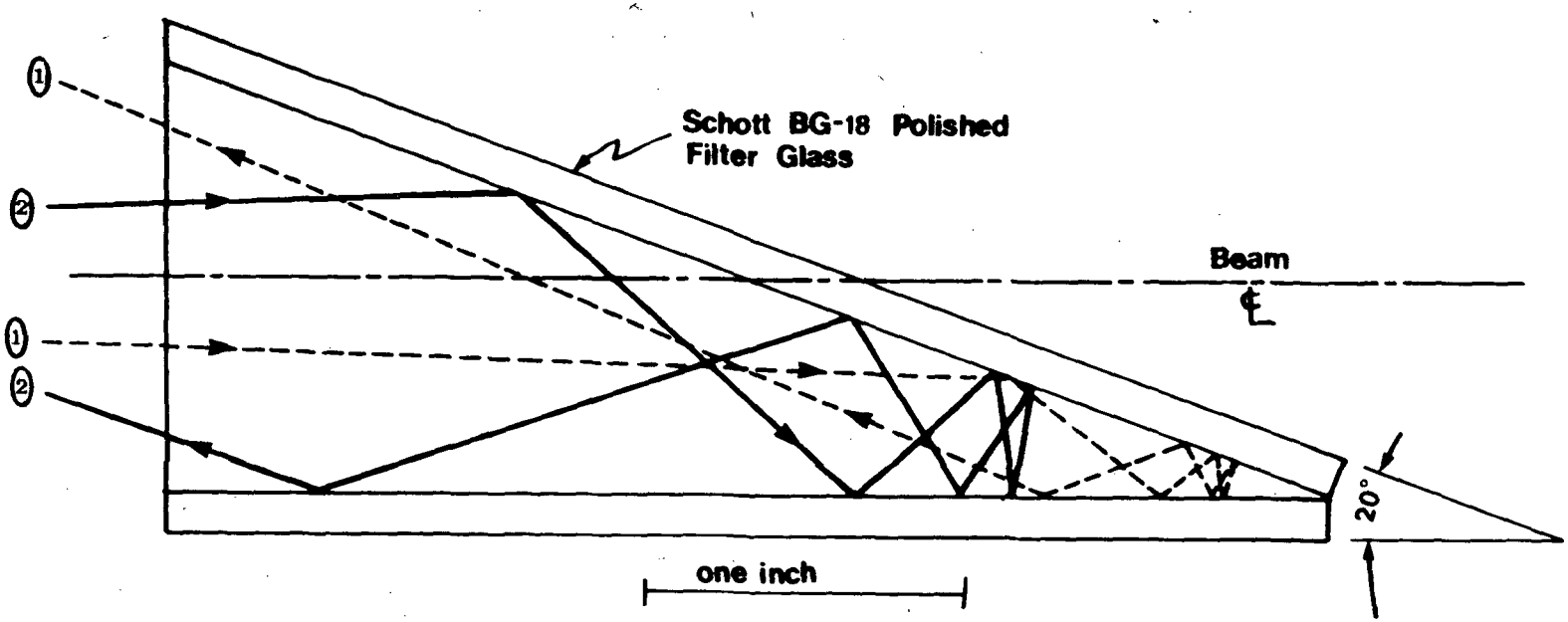

Figure 12

Ray Tracing in the Viewing Dump

wedge are covered by glass plates, resulting in a sort of flattened Rayleigh horn which is tailored to the oblong footprint of the scanned viewing beam. Finally, the dump is backed by a black surface of the same shape, and the whole structure placed at the rear of a short, dead-end port provided for the purpose.

The last element of our stray-light reduction program is the elimination of light transmitted to the scattering chamber by total internal reflection in the glass sections of the Penning discharge tube. This was done by painting the outside of these sections with a commercial black paint which reduces the reflectance at the exterior surface to about 10^{-6} by accurately matching the glass refractive index.

The ultimate test of these techniques is the measured equipment-scattered light level at the laser wavelength. This light level is one of the lowest attained in any experiment of this kind, being equivalent to Rayleigh scattering from no more than 3 microns of neutral nitrogen gas, or about 20% of the typical center-spectrum Thomson signal. The actual value in a particular experiment can be 2 or 3 times this figure if the entrance beam optics have been allowed to become dirty. The main point we wish to make is that ours is the only low-density experiment where accurate Thomson measurements have been possible at the laser wavelength. As discussed in Chapter 3, our equipment scattered light level is about 3,000 times better than that reported by the Culham group in their Tokamak measurements.

5.5 Scattered Light Detection Optics

The Thomson scattering volume is defined by the intersection of the volume illuminated by the focussed laser beam and the volume observable from a point on the detector surface. As shown in Figure 7, the observable volume is determined by the image of aperture D_3 projected on the

scattering region by the lens pair L_5, L_6. This aperture is rectangular, with fixed width and adjustable length, and oriented so that only the illuminated plasma is seen, while the length of the plasma sample can be varied to optimize received signal strength and resolution. Lens L_7 then returns the scattered beam to a parallel state as required by the multilayer filter F_1, which is the detected light spectrometer. Light transmitted by F_1 is detected by a photomultiplier. The characteristics of this filter are discussed separately in section 5.6.

Aperture D_2 is a large, adjustable, circular iris which determines the f-number of the viewing system. It is usually opened to the maximum useful aperture of the system, which is an effective f-number of 8.33. Since the lens L_5 has a 47 cm focal length, the scattered light viewing solid angle is at most

$$d\Omega_s = 0.011 \text{ sterradians} .$$

The maximum opening of D_3 consistent with useful spacial resolution in the plasma and beam parallelism at F_1 is 4 mm x 0.76 mm, giving an image in the plasma which corresponds to a cylindrical Thomson scattering volume of projected length 7.4 mm, or true length 8.6 mm, and diameter 0.95 mm. Therefore, the maximum available viewing <u>etendue</u>[81] in this experiment (the product of beam area and solid angle) is

$$\Phi_s = d\Omega_s \, \ell_{\perp s} d_s = 7.8 \times 10^{-4} \text{ sr-cm}^2 .$$

Finally, the total standard deviation of scattering angle due to both the illumination and detection beam ray bundles is 3.9° or 6.5% of the minimum angle used for scattering. This figure corresponds to an uncertainty of roughly $\pm 1^\circ$ in the direction of the sensitivity vector $\bar{k}$ for either of the two scattering angles. This means that there will be no more than a 2% cross-talk between measurements of the transverse

and longitudinal velocity distributions.

The rotation axis of F_1 is parallel to the long dimension of slit D_3 and perpendicular to the direction of linear polarization of the scattered light as it falls on the filter.

The Gunter bounce technique[82] for enhancing photomultiplier sensitivity is not employed in our detection system because the effective gain enhancement is a quite critical function of incident light angle. Also, the maximum gain of 2.0 which could be had in this way was not worth the effort.

Careful attention has been paid to the effects of diffraction and of spherical aberration in the design of all optical elements in this experiment.

Diffraction plays no significant role. By design, the collimated laser beam illuminates no apertures. Diffracted stray laser light will not be able to produce measurable Thomson scattering because of its low intensity, and is simply removed along with the rest of the equipment scattered light as discussed above. Where apertures are illuminated, as in the detection optics, they will be lens pupils, and we might ask whether diffraction might interfere with image formation. However, a quick calculation verifies that the beam etendues used throughout the system are very much larger than the pupil diffraction etendues. As shown, for example, in reference 83 the diffracted intensity distribution in the focal plane of a thin lens uniformly illuminated by a monochromatic plane wave with wavelength λ_o and intensity I_o is

$$\frac{I(r)}{I_o} = \left(\frac{D}{2r_o}\right)^2 \left[\frac{J_1(r/r_o)}{(r/r_o)}\right]^2 \qquad (5\text{-}3)$$

where $r_o = \left(\frac{f_\# \lambda_o}{\pi}\right)$, f is the lens focal length, and $f_\# = f/D$ its effective f-number as determined by a finite circular pupil of diameter

D in the lens plane. This is the so-called "Airy pattern" of the lens. The central zone of this pattern, bounded by the first zero of the Bessel function, contains 84% of the diffracted energy, and has a radius $r_1 = 1.22\, f_{\#}\lambda_o$.* The fraction of the total energy which is bounded by the nth zero of J_1 is

$$\frac{I(r_n)}{I(r_\infty)} = 1 - J_o^2(r_n/r_o) \qquad (5\text{-}4)$$

so that 95.2% of the energy lies within the fourth zero, at radius $r_4 = 4.23\, f_{\#}\lambda_o$. This latter radius corresponds to an <u>etendue</u>

$$\Phi_d = \left(\frac{\pi}{2}\right)^3 (4.23)^2 \lambda_o^2 = 2.1 \times 10^{-7} \text{ sr-cm}^2$$

which is independent of $f_{\#}$. This figure is 100 times smaller than the smallest <u>etendue</u> employed in the system.

Sperhical aberration is not so easily dismissed. In order to keep the cost of our lenses below $1,500, aspheric surfaces could not be used. Instead, plano-convex surfaces were used throughout. Insofar as shape is a factor, this choice nearly minimizes spherical aberration when a simple lens is used to focus a parallel beam, provided that the beam impinges on the convex surface. For such a lens, the angular aberration of the edge rays is[84]

$$d\theta_{ab} = \frac{n^3 - 2n^2 + 2}{16n(n-1)^2 f_{\#}^3} \qquad (5\text{-}5)$$

*This is the origin of the so-called "Rayleigh limit" for diffraction-limited optics.

which, for ordinary materials and red light, amounts to

$$d\theta_{ab} = \frac{145}{f\#^3} \text{ milliradians (mr)} . \qquad (5\text{-}6)$$

A survey of the experiment in Table 5-1 shows that spherical aberration is within reasonable limits, particularly as the typical ray will experience much less aberration than an edge ray. As a counter example, an f-number of 3.0 for the viewing lens would cause 16 milliradians of aberrations.

Table 5-1

Survey of Spherical Aberration

location	f-number	edge-ray spherical aberration (mr.)	limiting divergence (mr.)	nature of limit
laser collimator output lens	10.0	0.15	0.6	design value of expanded beam divergence
plasma illumination lens	15.0	0.04	0.6	same as above
plasma viewing lens	8.33	0.25	2.0	degradation of filter (F_1) bandwidth

The plane windows through which the converging illumination and scattered beams must pass also cause lateral aberration, but in a direction opposite to spherical aberration, by increasing rather than decreasing the effective focal distance of the edge rays. This effect has

also been calculated. Its magnitude is such as to eliminate aberration in the illumination lens, and to give net viewing lens aberration of the same magnitude listed in Table 5-1 but opposite sign, for the edge rays.

5.5.1 The Multilayer Dielectric Filter-Instrumental Properties

We use multilayer dielectric filters to scan the scattered spectrum because they are cheap, and because they can provide 2 or 3 orders of magnitude greater etendue than a monochromator when a modest resolution ($d\lambda \gtrsim 1$ Å) and tuning range ($\Delta\lambda/\lambda_o \sim 10\%$) are sufficient.

Such a filter consists of two or more stacks of plane parallel quarter-wave layers of alternating high and low refractive index, with integral half-wave high or low index spacers between adjacent stacks. Their gross behavior can best be introduced by considering light transmission through a single half-wave layer with refractive index n_k.

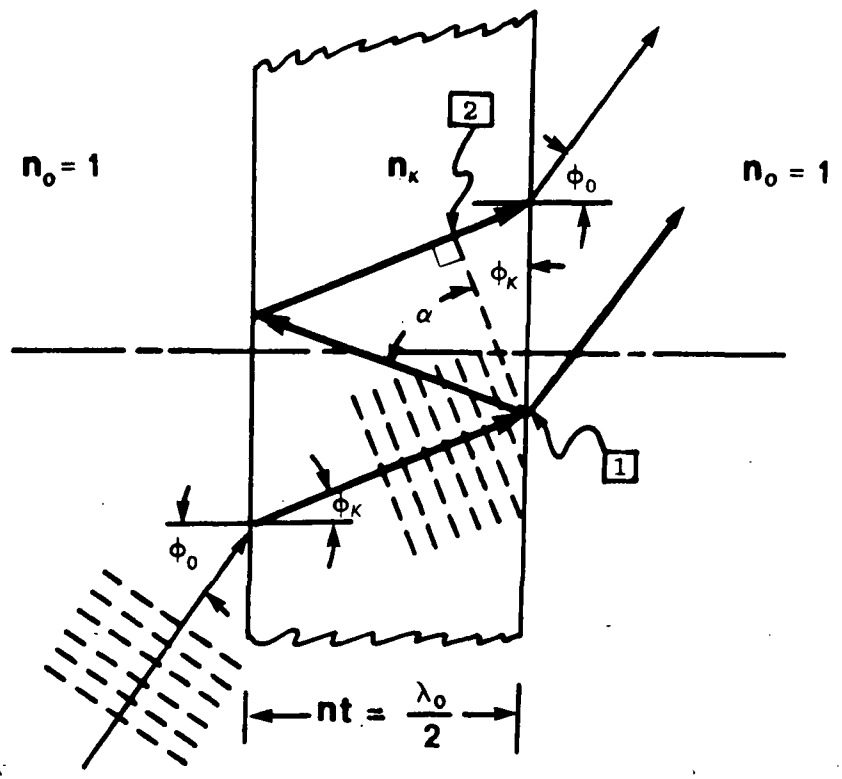

Figure 13

Ray-Tracing in a Half-Wave Layer

In the diagram, a plane wave of wavelength $\lambda \leq \lambda_o$ is incident from air on the layer at angle ϕ_o. The layer has phase thickness $n_k t = \frac{\lambda_o}{2}$. The transmitted wave will be a maximum when the rightward moving wavefronts resulting from multiple internal reflections are all in phase. For example, the amplitudes at points 1 and 2 will have a phase distance difference

$$n_k(d_2-d_1) = \frac{n_k t}{\cos \phi_k} (1 + \sin \alpha) = \lambda_o \cos \phi_k$$

since $\alpha = \frac{\pi}{2} - 2\phi_k$. If we require that $n_k(d_2-d_1) = p\lambda$

$$\frac{\lambda}{\lambda_o} = \frac{\cos \phi_k}{p}$$

so that a simple tuning formula results for the first transmission maximum $(p = 1)$:

$$\frac{\lambda}{\lambda_o} = \left[1 - \frac{\sin^2 \phi_o}{n_k^2}\right]^{1/2} \qquad (5\text{-}7)$$

or

$$\frac{\lambda - \lambda_o}{\lambda_o} = \frac{\Delta\lambda}{\lambda_o} \cong - \frac{\phi_o^2}{2n_k^2}$$

using Snell's law to relate internal and external incidence angles. This shift toward the blue is somewhat counter-intuitive since it might at first seem that increasing incidence angle, and the resulting increase in ray path length in the film, would lead to a red shift.

In fact, it can be shown (see, for example, reference 85) that the tuning formula for a complete filter including the quarter-wave stacks is also given by (5-7) to within a very small error, if n_k is replaced by an "effective filter index" n_f, which depends upon details of the filter construction. For practical purposes, the simpler tuning formula

$$\Delta\lambda = -b\,\phi_o^2 \quad \text{Å} \tag{5-8}$$

will be adequate. It is accurate to within 2% for angles less than 20° with our filter, using $b = 1{,}350$ Å for $n_f = 1.51$. The exact formula, derived in a paper now in preparation, shows a very slight dependence on the state of incident light polarization. For our filter, the variation amounts to 2.5% of the tuning range at an angle of 30°.

By differentiating equation (5-8), it can be seen that tight limits exist on the allowed nonparallelism of the incident light if the effective filter resolution (reciprocal bandwidth) is not to be degraded. However, since those rays which diverge from the incident beam axis in the plane of incidence will generally have a much more serious effect on the filter resolution than those which diverge perpendicularly to this plane, simply writing $-\delta\lambda = 2b\phi_o\delta\phi_o$ is not sufficient.

Two cases may be distinguished. The first, $\delta\phi_o \gg \phi_o$ describes perpendicular beam incidence. Here,

$$\sigma_\lambda\Big|_{\phi_o=0} = \frac{b}{\sqrt{3}}(\delta\phi_o)^2 \quad \text{Å} \tag{5-9}$$

gives the standard deviation of peak transmission wavelength for a beam whose rays diverge uniformaly in all directions up to half-angle $\delta\phi_o$ from the beam axis. If the filter has face area A cm^2, the <u>etendue</u> for normal incidence is then

$$\Phi_{f_{max}}(0) = \pi A(\delta\phi_o^2) = \frac{\pi\sqrt{3}\,A}{b}\,\sigma_\lambda \quad \text{sr-cm}^2 . \tag{5-10}$$

In the second case, $\delta\phi_o \ll \phi_o$, it will be useful for further discussion to express the deviation of incidence angle $\delta\phi$ in terms of

its angular components $\delta\phi_\perp$ and $\delta\phi_\parallel$ with respect to the plane of incidence. This gives:

$$\frac{\delta\phi}{\phi_o} \cong \frac{\delta\phi_\parallel}{\phi_o} + \frac{(\delta\phi_\perp)^2 + (\delta\phi_\parallel)^2}{2\phi_o^2} \quad . \tag{5-11}$$

In the traditional method of illuminating filters in experiments such as ours, $\delta\phi_\perp \cong \delta\phi_\parallel$ with maximum half-angle $\delta\phi_o$ as before, so that

$$\sigma_\lambda\Big|_{\phi_o \neq 0} = b\,\phi_o\delta\phi_o \quad \overset{o}{A}$$

and

$$\Phi_f(\Delta\lambda) = \frac{\pi A}{b|\Delta\lambda|}\,\sigma_\lambda^2 \quad \text{sr-cm}^2 \quad . \tag{5-12}$$

This is a gross underestimate of the available filter <u>etendue</u>, as will be shown. By equating <u>etendues</u>, we find that the plasma sample area we are allowed to view is only

$$A_p = \frac{4Af_\#^2\sigma_\lambda^2}{b|\Delta\lambda|} \quad \text{cm}^2 \quad . \tag{5-13}$$

if $\delta\phi_\perp = \delta\phi_\parallel$. In our experiment, if we require $\sigma_\lambda = 1$ $\overset{o}{A}$, a maximum tuning range $|\Delta\lambda| = 200$ $\overset{o}{A}$ and viewing lens $f_\# = 8.33$, the projected area of the plasma sample volume could be at most 2 mm^2.

We are most interested in the situation where most of the divergence occurs perpendicular to the plane of beam incidence* on the filter. We see from (5-11) that the contributions of $\delta\phi_\perp$ and $\delta\phi_\parallel$ to $\delta\phi$ are

*The "plane of incidence" is always defined as that plane which contains the incident beam symmetry axis and the surface normal.

comparable only when $\delta\phi_\perp \gg \delta\phi_\parallel$ that is, for $(\delta\phi_\perp)^2 \to \phi_o \delta\phi_\parallel$.

Our contribution has been simply to align the filter rotation axis in such a way that the larger of the two components of $\delta\phi$ will be perpendicular to the filter incidence plane. Then, since $\ell \gg w$, we have $\delta\phi_\perp = \ell/2f$ and $\delta\phi_\parallel = w/2f$. Now, ℓ may be made as large as

$$\ell^2 = \pi w f \phi_o \tag{5-14}$$

without further degrading the filter bandwidth. Expressed in terms of peak wavelength standard deviation, this degradation is now only $\sigma_\lambda \cong b\phi_o \delta\phi_\parallel$ Å so that we have as a final result for the etendue achievable with the new method of illumination,

$$\Phi_f'(\Delta\lambda) \simeq \frac{\pi A}{b\sqrt{|\Delta\lambda|}} (\sigma_\lambda)^{3/2} \quad \text{sr-cm}^2 . \tag{5-15}$$

This represents an improvement of $\sqrt{|\Delta\lambda|/\sigma_\lambda}$ over the usual experimental etendues, as expressed by (5-12) above. Again picking $\sigma_\lambda = 1$ Å and $|\Delta\lambda|_{max} = 200$ Å for a numerical estimate, we can now see at least 28 mm^2 of plasma area. The actual magnitude of our filter's etendue at $|\Delta\lambda| = 200$ Å is 3×10^{-3} sr-cm^2, which is a figure about 100 times that of a good monochromator, but only a factor of 4 greater than we require in our experiment. At normal incidence, the filter may easily be 1000 times better than the monochromator and this advantage is indpendent of resolution. Unfortunately, the filter must be tuned.

Multilayer filters also have 2 or 3 orders of magnitude better rejection ratio for light outside the pass band than do monochromators. This is a severe disadvantage for monochromators, since they must be used in series with another dispersing instrument for successful Thomson scattering work.

5.5.2 The Multilayer Dielectric Filter - Measured Properties

The useful tuning range of a multilayer filter is limited by degradation of the transmissivity and/or resolution at large incidence angles. Further, as mentioned in the previous section, the resolution or $(\text{bandwidth})^{-1}$ will be further degraded if the incident light is non-parallel. Of specific interest are the total or integrated transmissivity and the effective resolution as functions of illumination incidence angle, divergence angle and state of polarization. The integrated transmissivity must be known precisely so that its variation may be removed from the Thomson data.

Accordingly, a recording spectrophotometer was assembled to measure these parameters (see Figure 14). The parallel white light source is a uniformly illuminated pinhole in the focal plane of a high quality collimating lens. The beam divergence is controlled by the size of the pinhole, and may be 0.55, 1.70 or 4.85 milliradians. The smallest pinhole used was 38μ in diameter. A series of 20 spectrograms at varying incidence angles from 0 to 30° was repeated 6 times for each of the 4 filters tested, in order to have measurements for the 3 beam divergence settings in both parallel and perpendicularly polarized light. Part of such a series for the filter used in our experiment is reproduced in Figure 15, normalized to the incident spectral intensity. Of course, the original spectrograms were taken in much greater detail. In this figure, the degradation of filter resolution at large angles is clearly seen, but the variation of the area under each curve (the integrated transmissivity) is not yet clear.

Separate measurements of this quantity were achieved by completely opening the spectrometer exit slit to accomodate the entire filter spectrum and repeating measurements of transmitted intensity versus

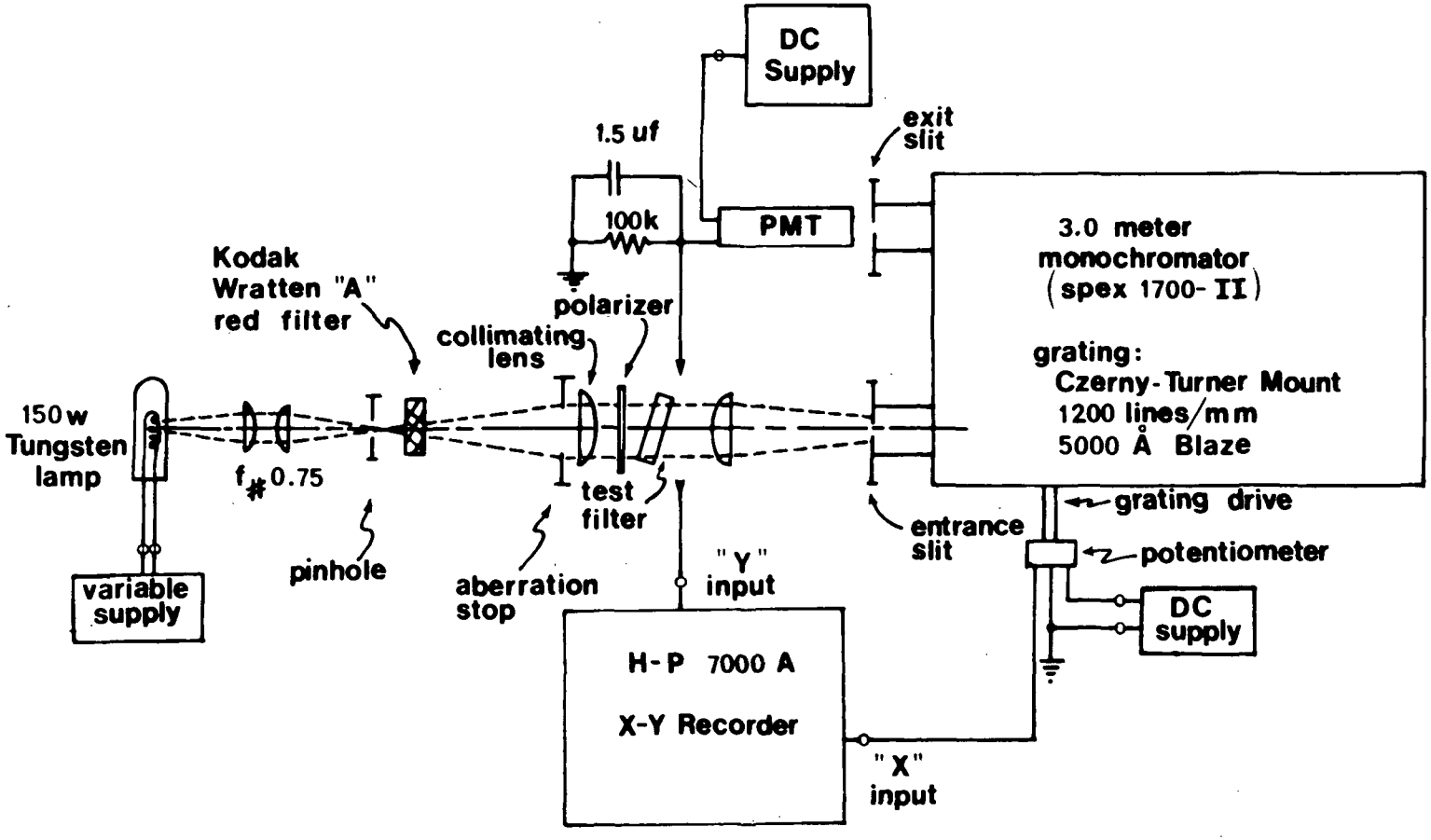

Figure 14

Spectrophotometer Setup

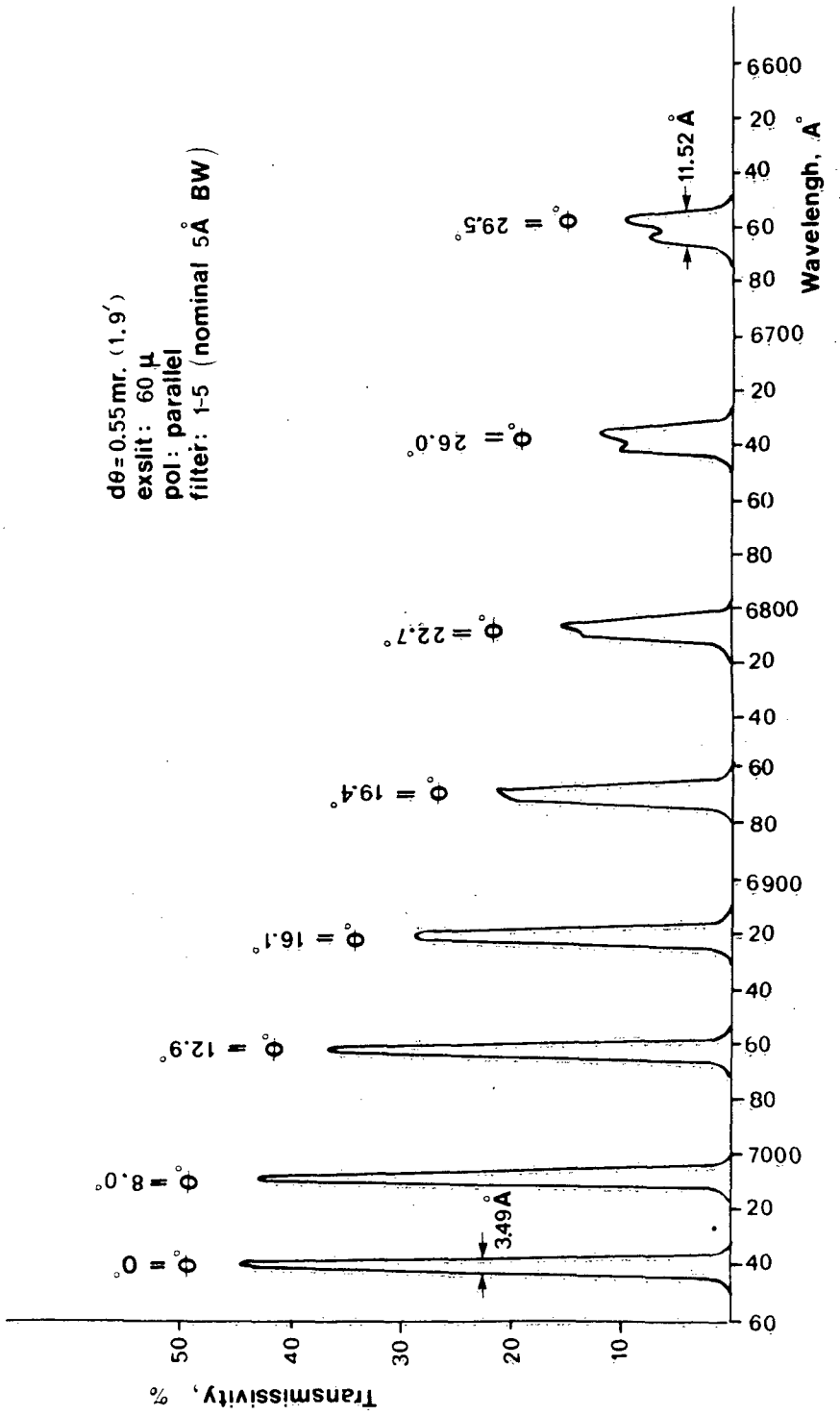

Figure 15

Typical Filter Spectrograms at Various Incidence Angles

incidence angle. After again normalizing to incident spectral intensity, a plot such as reproduced in Figure 16 results.

From the filter spectrograms, additional plots were made of peak transmissivity and bandwidth as a function of wavelength, and of peak transmission wavelength shift versus incidence angle, all with state of polarization and beam divergence as parameters. The bandwidth and tuning curves for the 5 $\mathring{A}$ width filter used in our experiment are shown in Figures 17 and 18.

Several conclusions can be drawn from all this data.

(1) We can see that the integrated transmissivity of this filter is much more nearly constant than is its peak transmissivity, so that only a small relative correction to the Thomson data will be required over the doppler range of about 200 $\mathring{A}$ employed.

(2) There is a significant dependence of the bandwidth and integrated transmissivity on the state of polarization of incident light.

(3) The degradation of resolution with filter tuning is tolerable because it occurs in the slowly varying wings of the scattered spectrum.

(4) The <u>amount</u> of degradation with filter tuning is much smaller if the incident light is linearly polarized parallel or perpendicular to the incidence plane, rather than circularly polarized, as in most published measurements. This is because the splitting seen in Figure 18 for large angles is added to the apparent bandwidth for circularly polarized light.

(5) The integrated transmissivity is insensitive to incident beam divergence up to about 5 milliradians. In fact, selective tests show this to be true even at 11 mr. If this were not true, a different calibration would be necessary for every change in plasma sample volume dimensions. In our experiment, $\delta\phi_{\parallel}$ is at most 0.8 mr.

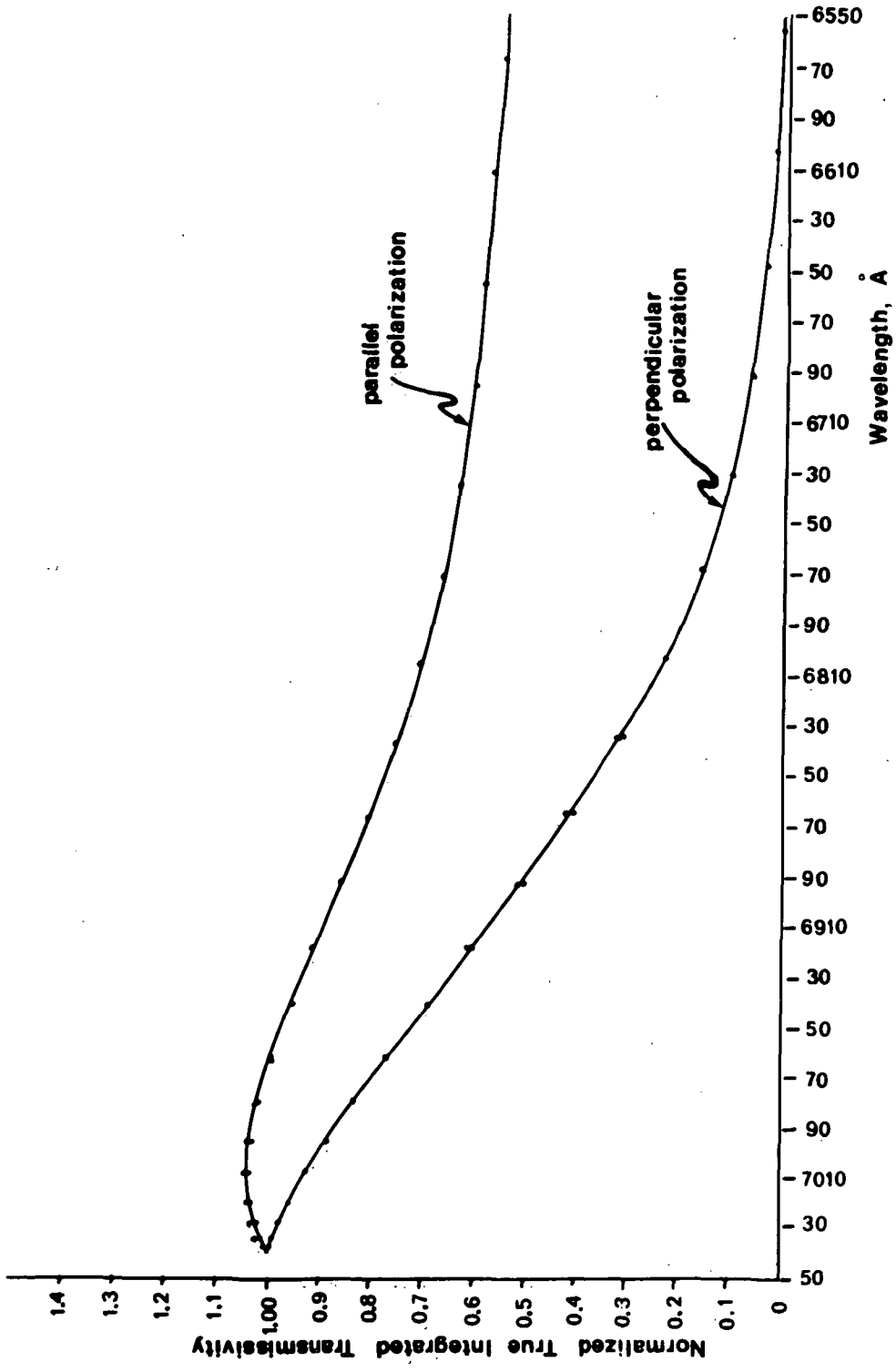

Figure 16

Integrated Transmissivity vs Wavelength, Filter 1-5

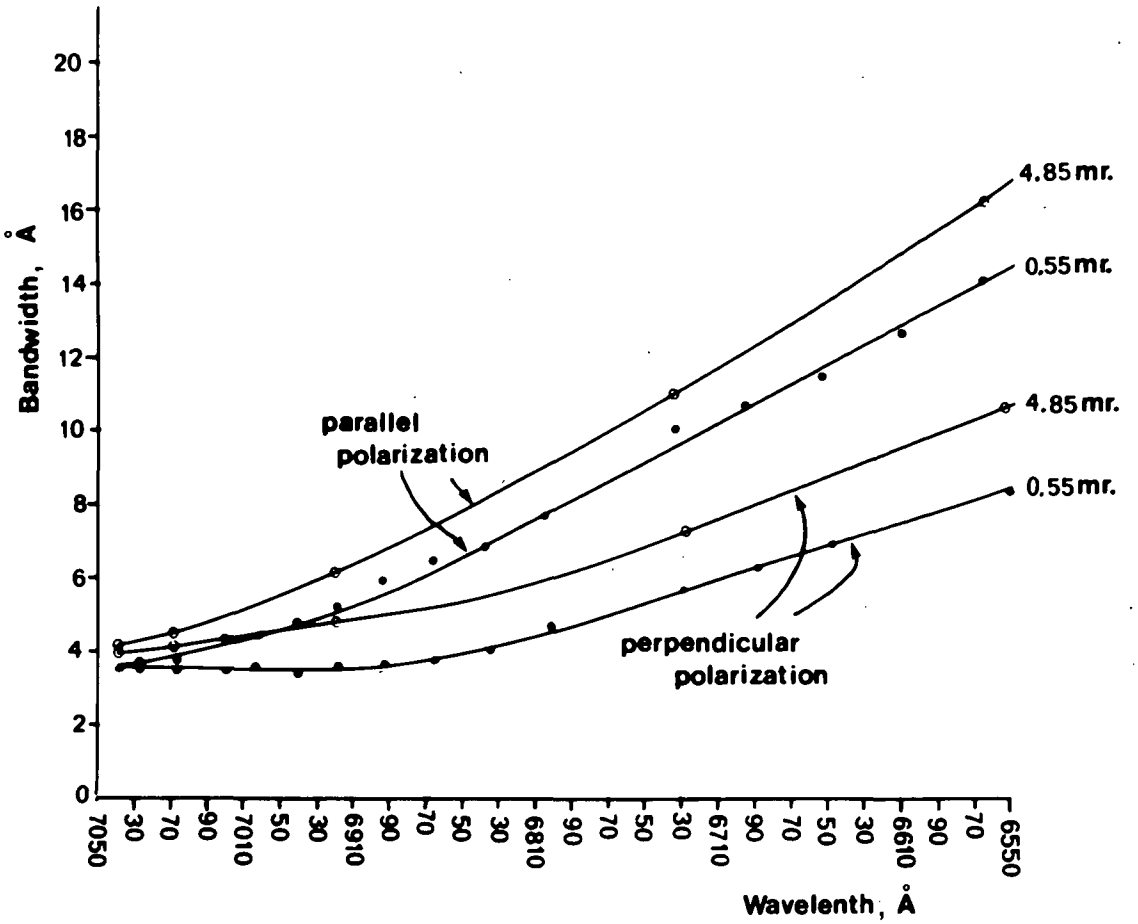

Figure 17

Measured Bandwidth vs Wavelength, Filter 1-5

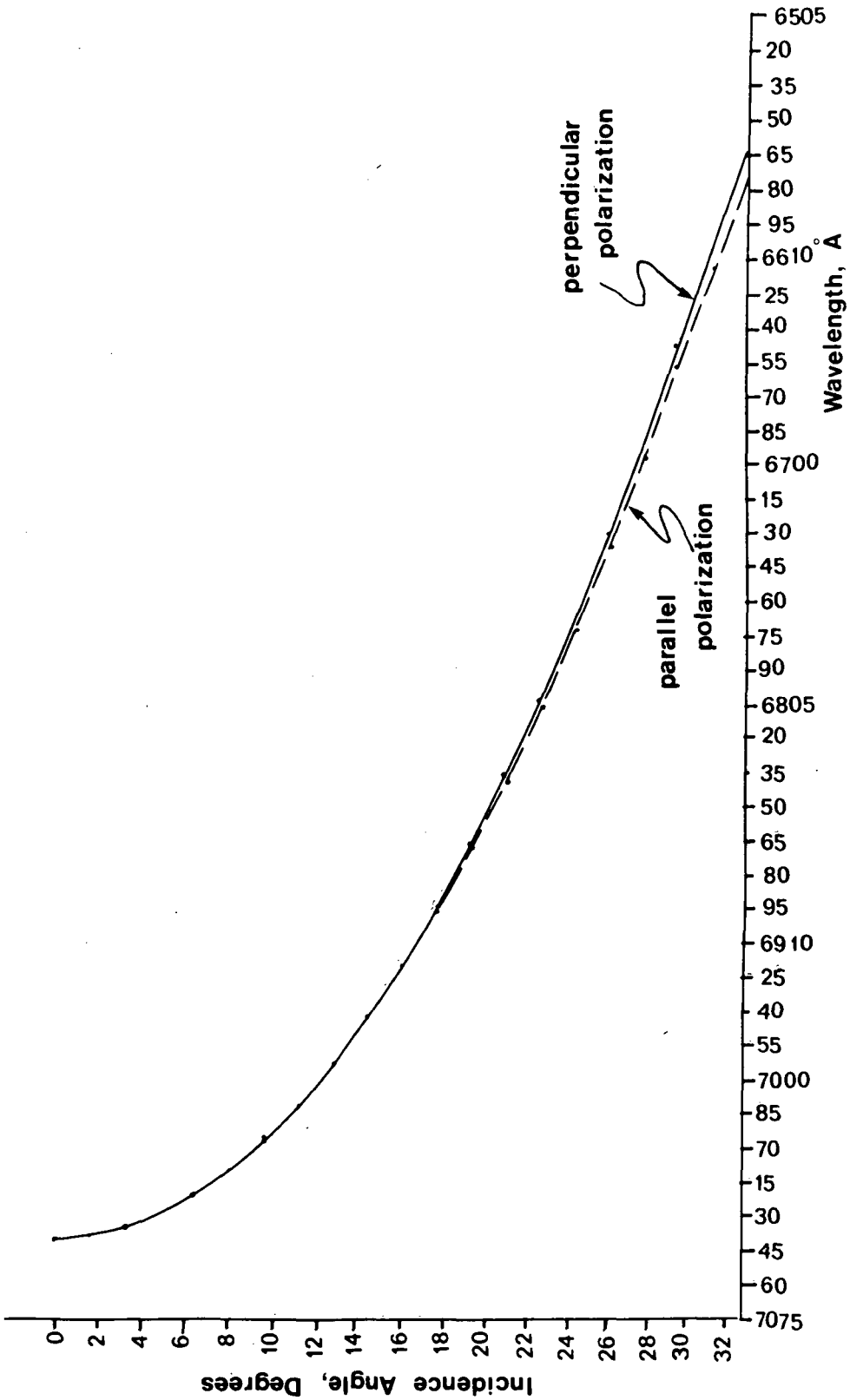

Figure 18

Measured Tuning Curve for Filter 1-5

Fortunately, Thomson scattered light is linearly polarized, and it is a simple matter to orient the filter rotation axis so that the filter sees only one state of polarization. (This is the same orientation that maximizes etendue when $\ell > w$.) However, the integrated transmissivity of a filter for any state of polarization can be accurately synthesized from the parallel and perpendicular data, providing the filter behaves isotropically. Figure 19 demonstrates that this is true. Here we plot the calculated response of the filter for a polarization vector inclined at 60° to the plane of incidence next to the measured integrated transmissivity for this situation.

Finally, we note that the integrated transmissivity of a general multilayer filter is much less well behaved as the filter is tuned than was true for the one discussed in this section. For example, a nominal 2 Å width filter which was considered and rejected for use in our experiment has the measured characteristic reproduced in Figure 20. In tuning to 6840 Å, at the blue edge of the Thomson spectrum, the filter shows a 70% increase in transmitted light for parallel polarization, but a 40% decrease for perpendicularly polarized light.

5.6 System Electronics

Figure 21 is a functional block diagram of the principal electronic components of the system used to fire the laser and the Penning discharge and to record Thomson scattering and other data. An asterisk indicates those components designed and built especially for this project.

The laser and the discharge current source are both controlled by highly stable delay generators. These allow the time of the laser flash to be carefully controlled relative to the plasma evolution and also provide control of the discharge pulse duration. Since the discharge cathodes are directly heated by 60 Hz current of the order of 100

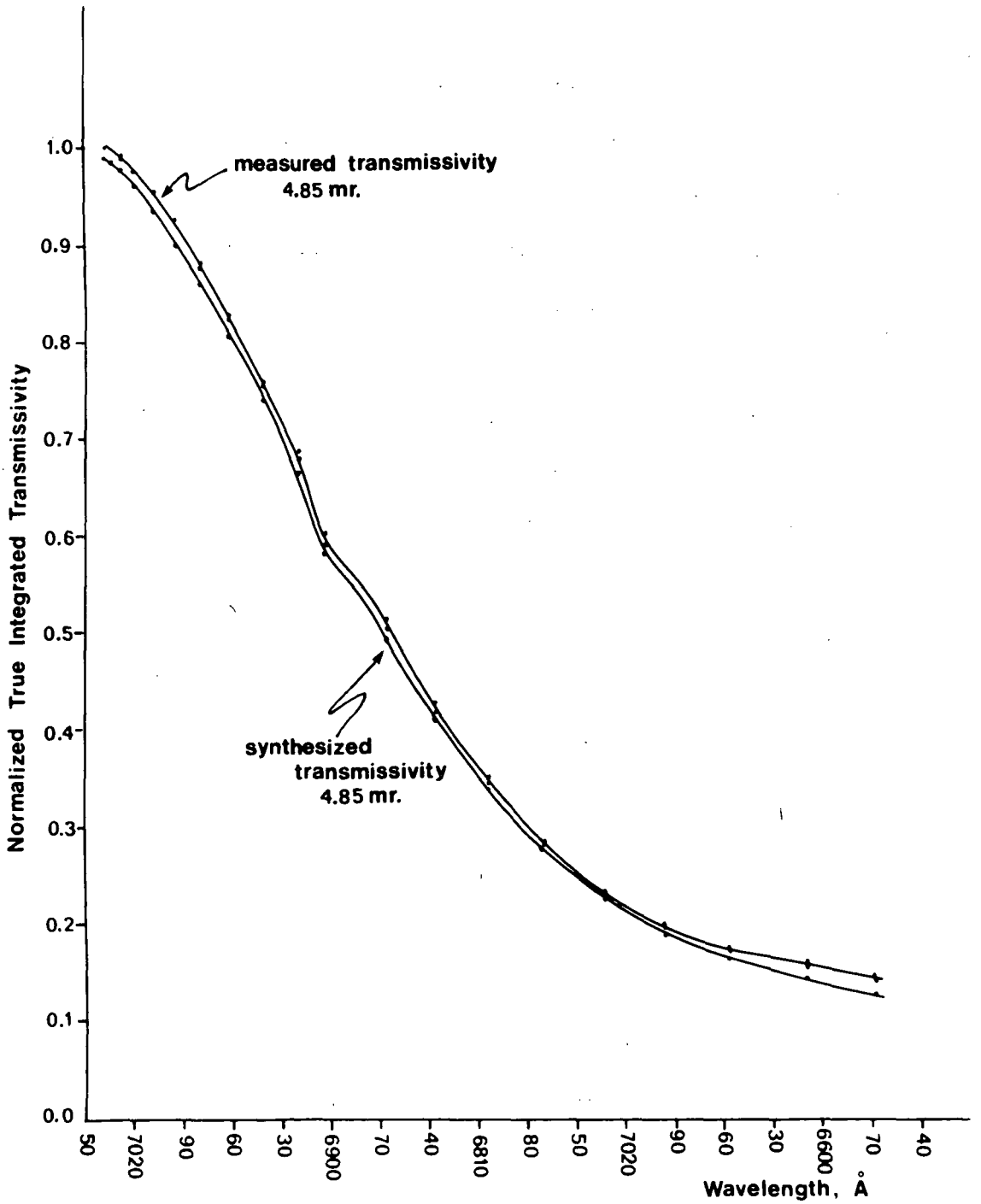

Figure 19

Synthesized and Measured Integrated Transmissivity, Filter 1-5

(Polarization Vector 60° to Plane of Incidence)

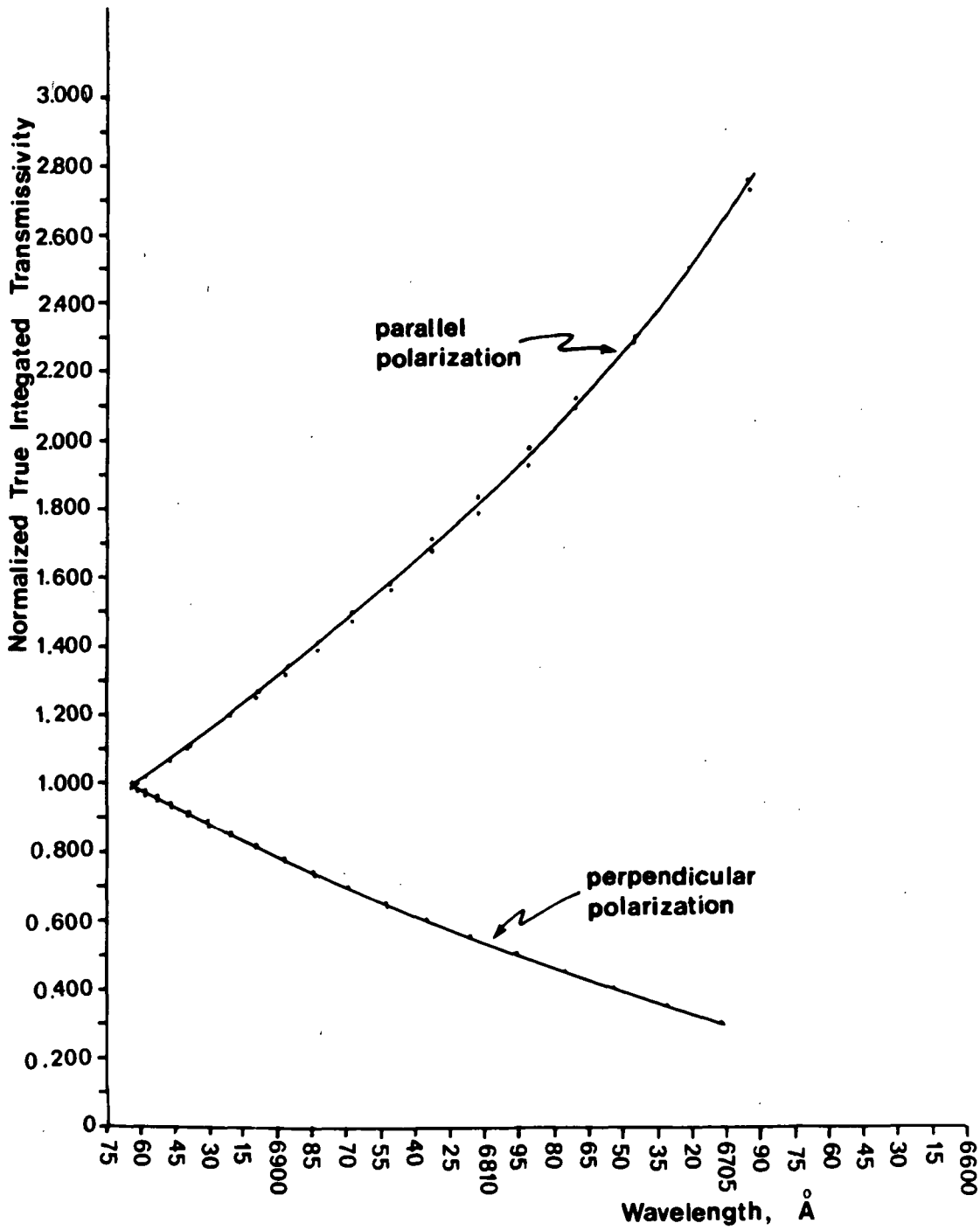

Figure 20

Integrated Transmissivity vs Wavelength, Filter 1-2

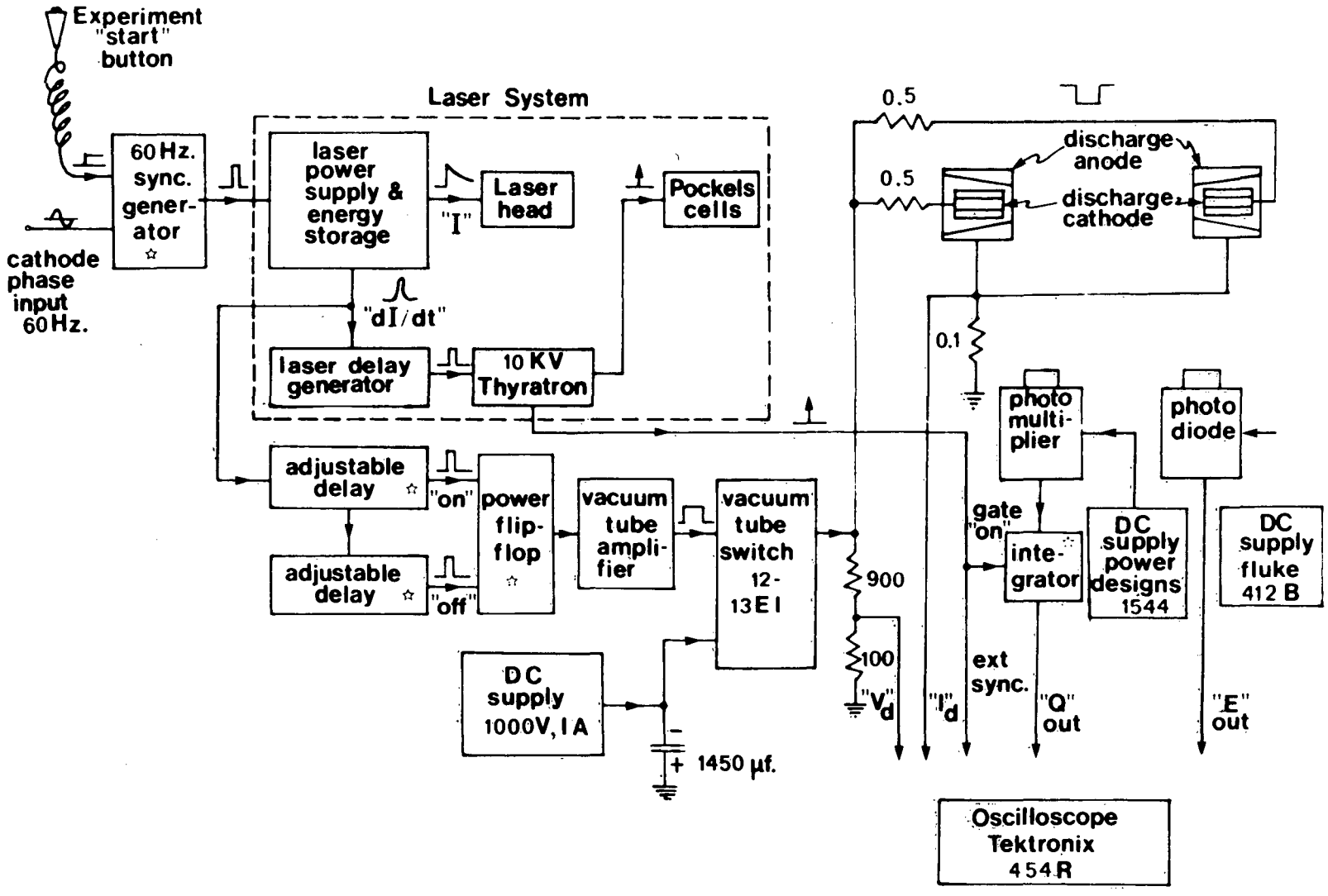

Figure 21

Functional Black Diagram of System Electronics

amperes, an alternating axial magnetic field component of peak value 90 gauss is present in the cathode region, resulting in a significant 60 Hz modulation of discharge parameters. For this reason, and also to eliminate the effect of 60 Hz pickup from other sources, most of the experiment is operated from this phase of the a-c line, and all experiment events are times to occur within ± 0.05 radians of the zero-crossing of this phase.

The 60 Hz synchronization generator produces a timing pulse whose jitter with respect to the 60 Hz zero-crossing is only ± 10 μsec or ± 4 milliradians. By this means, any 60 Hz effect present will certainly be quite constant from one shot to the next.

Of the 3 delay generators, the one provided with the laser introduces a timing jitter which is at most ± 0.05% of the delay time or ± 0.5 μsec and accuracy of order ± 0.2% or ± 2 μsec. Accuracy of the two specially built delay generators is of the same order, but jitter is only ±0.005% under normal conditions.

In operation, the synchronization pulse initiates optical pumping of the ruby about 1 millisecond before the 60 Hz zero-crossing. When the laser lamp begins to conduct, a lamp current rate pulse simultaneously starts the 3 timing generators which ultimately start the plasma discharge current source, open the Pockels cell shutter and then stop the discharge, closely concurrent with the zero-crossing. This approach allows Thomson measurements to be made at a selected time during the plasma discharge without affecting lamp energy input to the ruby rod.

A vacuum-tube amplifier and high current switch was available for the discharge current source. Since the two discharge electron guns together are capable of about 600 amperes, temperature limited, it was desired to have a current source of similar capabilities in order to

get as much plasma electron density as possible. Unfortunately, this switch is capable of 140 amperes at most, but its other characteristics are ideal. It consists of 12 Ediswan 13E1 beam tetrodes in parallel, and when these are driven temperature-limited, they behave like ideal current sources. This automatically provides the necessary stabilizing factor in the negative-resistance region where we operate the discharge. In addition, this behavior results in rapid achievement of a steady-state discharge in the quiescent mode of operation, and consequent close control of discharge input energy.

Figure 22 is a picture of the typical discharge current and voltage profiles, and demonstrates this last point. Other properties of the current switch are: maximum open circuit voltage, 900V; rise and fall times, 5 μsec; pulsewidth for 5% current amplitude decay, 400 μsec; and duty cycle, 0.02 at maximum voltage and current.

5.7 Detector Electronics and Photographic Record

The photomultiplier used to record scattered light signals is an RCA 31000F extended red response tube. Twelve stages of electron multiplication provide an overall electrical gain of 6×10^7 at 2350V. Rise time of the anode signal is 2.4 ns, which is the same as our oscilloscope rise time. Although anode dark current is only 50 nanoamperes at this voltage and room temperature, the tube is housed in a thermoelectric refrigerator. However, the purpose of this device is to eliminate temperature-dependent gain changes in the tube rather than to further reduce the dark current. We normally operate the tube at 15°C.

The other major source of gain changes in multiple stage photomultipliers is supply voltage variation since $\delta \ln G = n \delta \ln V$ for an n-stage tube. When $n = 12$, we require approximately 0.1% voltage stability for 1% tube gain stability. Our supply is 5 times better than this over a 24 hour period.

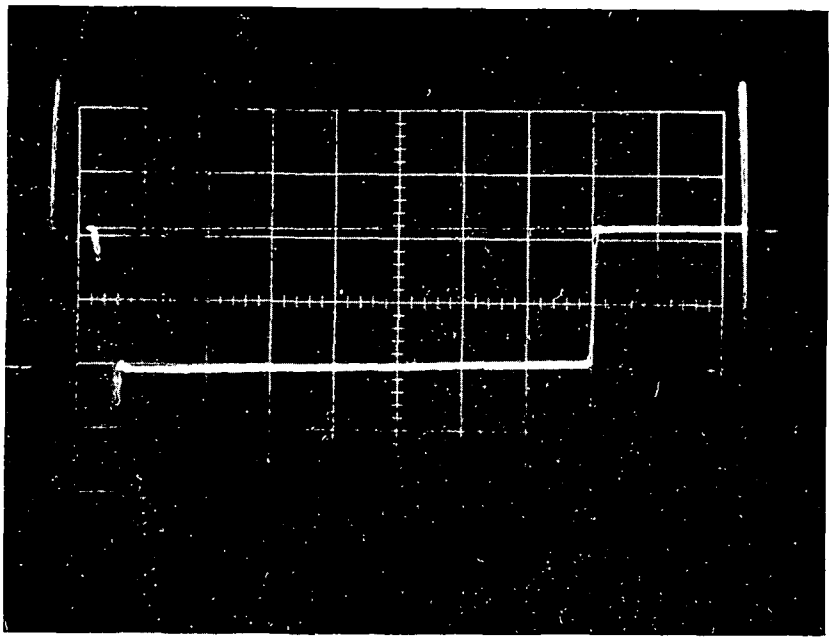

Discharge Current

Vertical: 50 amp/division
Horizontal: 50 μsec/division

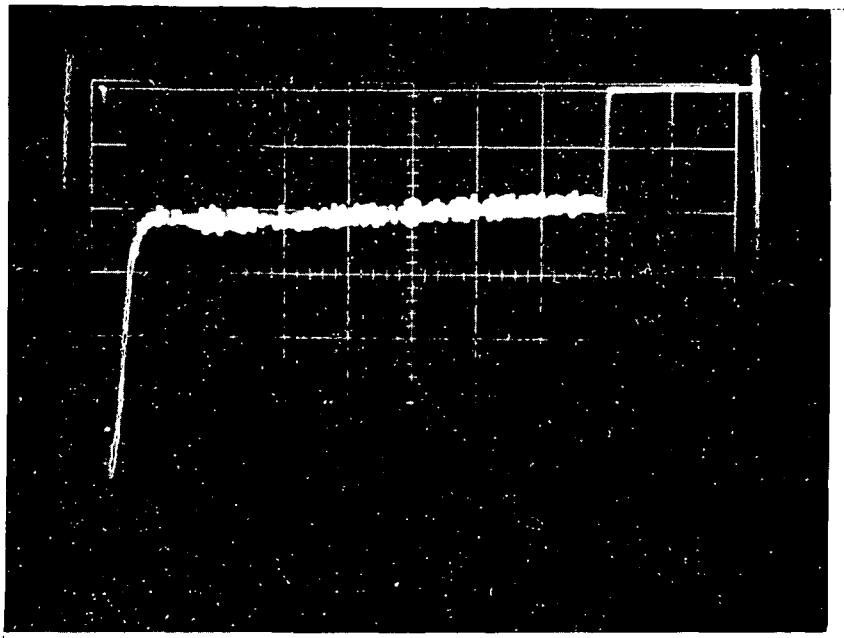

Discharge Voltage

Vertical: 100 volt/division

Horizontal: 50 μsec/division

Figure 22

Typical Penning Discharge Voltage and Current Profiles (400 μsec Duration)

The photomultiplier "front end" has several special properties which are essential for this experiment. The Na/K/Sb/Cs semitransparent cathode material has a measured photon-to-electron conversion efficiency of 7.05% at 6943 Å which, at the time of purchase, was the best commercially available. This is a factor of 4 improvement over the best standard surface (S-20) at this wavelength. High quantum efficiency is extremely important from statistical considerations (see chapter 6) when low light levels are being detected. Another advantage of the tube is its first-dynode gain of 50, which practically eliminates statistical noise contributions from the multiplication process itself. Finally, the tube is linear up to an anode peak current of 150 ma, which corresponds to a cathode signal of about 300 photoelectrons with our operating parameters. This is 5 times the largest Thomson signal recorded.

The photomultiplier anode pulse must be integrated numerically or electronically, since it is the total charge which corresponds to the scattered photon number. Electronic integration is much the easier of the two and also discriminates against high frequency electronic noise. A high speed gated integrator was constructed for this purpose and is located very close to the PMT chamber, since our laboratory is a highly active electrical environment. Its electronic properties are: sensitivity, 2.4 mv per picocoulomb (pc); time constant, 1 μsec; noise level, 3 pc; delay, 15 ns; and linearity, about 3% up to $Q = 10^3$ pc or 10 ma peak input current, and down to an input pulsewidth of 5 ns. With our operating parameters, the integrator provides an output signal of 22 mv per PMT cathode photoelectron.

Our oscilloscope is a Tektronix R454. While not the fastest scope available at the time of purchase, its 2.4 ns rise time is more than adequate for recording the integrated scattering signal, and this input bandwidth is maintained down to a sensitivity of 20 mv/division.

The oscilloscope camera and CRT together provide a writing speed of 3.2 divisions per nanosecond with ASA 10,000 Polaroid film. Features contributing to this speed are the 14 kv accelerating potential and P11 (blue) phosphor used in the CRT, the $f_{\#}1.2$ camera lens and the 0.5 image-to-object ratio used in this system.

5.8 Vacuum System and Mechanical Design

The vacuum system consists of a mechanical forepump, 300 liter/sec oil diffusion pump, liquid nitrogen cold trap and separate experiment roughing pump. The cold trap is re-entrant and has a 36 hour liquid nitrogen capacity. The vacuum station is quite clean and will achieve a base pressure of 5×10^{-8} torr.

The total conductance of the experiment tube is 16 liter/sec at the vacuum station port, but this is normally reduced to about 4 liter/sec by partially closing the valve to this port, in order to preserve an upper limit of 10% neutral density variation throughout the discharge. The total leak rate of the system is about 0.02 micron-liter/sec, so that this pumping speed results in a possible contamination of order 1% at an operating pressure of 1 μ. Hydrocarbons are responsible for only 15% of this contamination level, the rest being air or outgassing hydrogen. The tube base pressure is about 2×10^{-6} torr. Pressures are measured at the cold trap port and at the tube fill gas inlet using triode-type ionization gages with the appropriate correction factors for different gases. These tubes are sensitive to magnetic fields and must be used with external field sources turned off. A Granville-Phillips variable leak with numerical indicator provides control of gas flow rate into the discharge tube.

The axial magnetic field required for operation of the Penning discharge is provided by 8 air-core water-cooled coils made by Ogallala

Electronic Mfg., Inc. Each has a 20.3 cm bore, overall diameter of 38.1 cm and 8.0 cm thickness, and is rated to produce a maximum field of 1200 gauss on axis, at 16.5 gauss/ampere. With a 15.3 cm center-to-center spacing, the assembly produces about 30 gauss per ampere on axis with a maximum spacial variation of ± 2%. The available current supplies for these coils limit the available field intensity to 750 gauss, but more is not needed for our purposes.

In the laser beam optics, angular alignment of the order of 5 seconds of arc must be maintained to assure proper registration of the beam focus with the observation volume. This is just the price we pay for using distance to reduce equipment scattering. Prevension of unintended motion of the scattering volume within the plasma column depends on rigid interconnection of the Penning discharge and the experiment optics. A nonmagnetic bench was constructed for this purpose from structural aluminum. The main beams of the bench are sufficiently rigid to deflect less than 0.001 inches per 800 pounds of distributed load. All other elements of the bench which might affect optical alignment, including lens and mirror holders, are also aluminum. In this way, misalignment due to differential thermal expansion is avoided.

Operational alignment of the entire system is provided by a small gas laser beam, expanded to the same size as the ruby beam and arranged so that insertion of a right angle prism produces a test beam which is concentric and collinear with the ruby laser output. This beam was also used for initial alignment of the detection optics, by using a small mirror to redirect it from the center of the scattering volume.

6. RESULTS AND EXPERIMENTAL PROCEDURE

In this chapter, we present and interpret our Thomson scattering measurements, and discuss relevant data obtained by other means. Experimental conditions are analyzed carefully and related to the procedures used to collect and analyze data.

6.1 Langmuir Probe Measurements

When Thomson scattering measurements are possible, they give much more detailed and reliable information about the state of a plasma than do Langmuir probe measurements. However, the probe was invaluable as an exploratory device for locating the best combination of ionization fraction, electron density and parameter repeatability from shot to shot. Even if these measurements had given different temperatures from those deduced from Thomson measurements, we would not have been too upset, because probe electron collection is strongly influenced by magnetic fields. However, it is gratifying that good agreement was found.

To take Langmuir data, the time-sample technique introduced by Hosea[86] was used. This method is desirable in a pulsed plasma where density and temperature change significantly during the plasma evolution, and permits rapid construction of a probe curve characteristic of a particular time during the pulse. In this technique, an oscilloscope is set up to record probe voltage versus current continuously, but is gated "on" for only a brief interval (0.5 μsec) during each plasma pulse. With a stable plasma firing repeatedly, the result is a fixed blinking dot on the scope screen, which will trace out a probe curve representing the selected time epoch when probe voltage is varied. Further, the extent to which the blinking dot remains confined to a

single curve in the V-I plane is a good quantitative measure of the reproducibility of plasma density and temperature.

Typical probe traces taken by time sampling are reproduced in Figure 23. These pictures represent conditions during the discharge, for magnetic fields of 150 and 600 gauss, respectively. The transition to an unstable discharge is clearly seen. In the second picture, neither the space nor the floating potentials are defined, and even an approximate temperature cannot be deduced. However, Thomson measurements have been made in a similar environment (series 4).

A summary of the variation of plasma density and temperature with changing neutral pressure at a time 25 μsec before shutdown of the discharge current source is shown in Figure 24, as measured by the Langmuir probe. These measurements were made at the center of the plasma column with a uniform magnetic field of 190 gauss. The subsequent variation of density and temperature indicated by the Langmuir data for the same magnetic field and radial position was shown in Figure 5. Curves for other pressures in the range shown in Figure 24 behave in very much the same way in the afterglow. Below this pressure range, the available neutral number begins to limit the electron density while above it, the ionization fraction is so small that the electron temperature falls below useful values for our experiment.

6.2 Rayleigh Scattering

The total Rayleigh scattering cross-section is

$$\frac{d\sigma_R}{d\Omega} = \frac{4\pi^2(\mu-1)^2}{n_o^2 \lambda_o^4} \sin^2\psi \qquad (6\text{-}1)$$

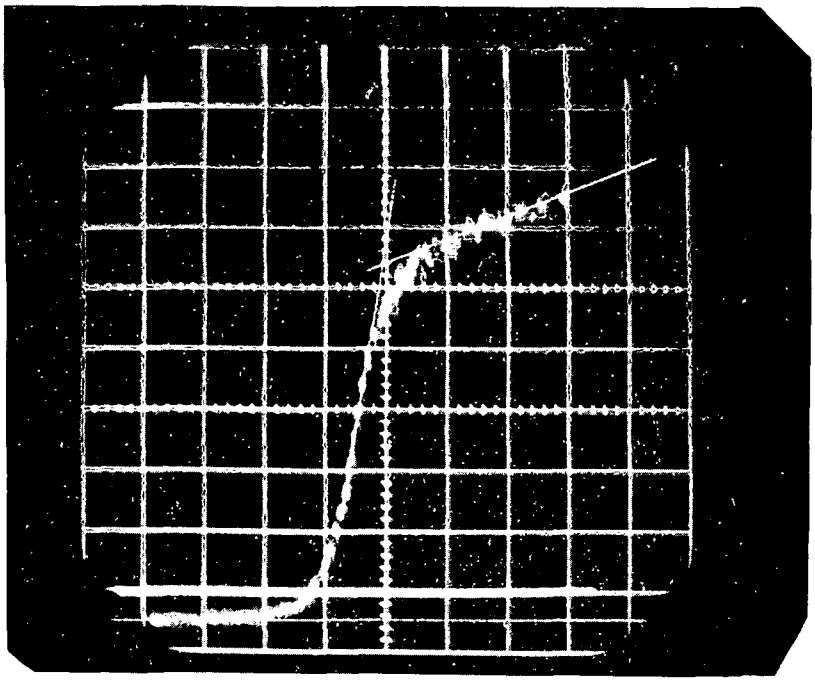

B = 190 gauss
(Quiescent)

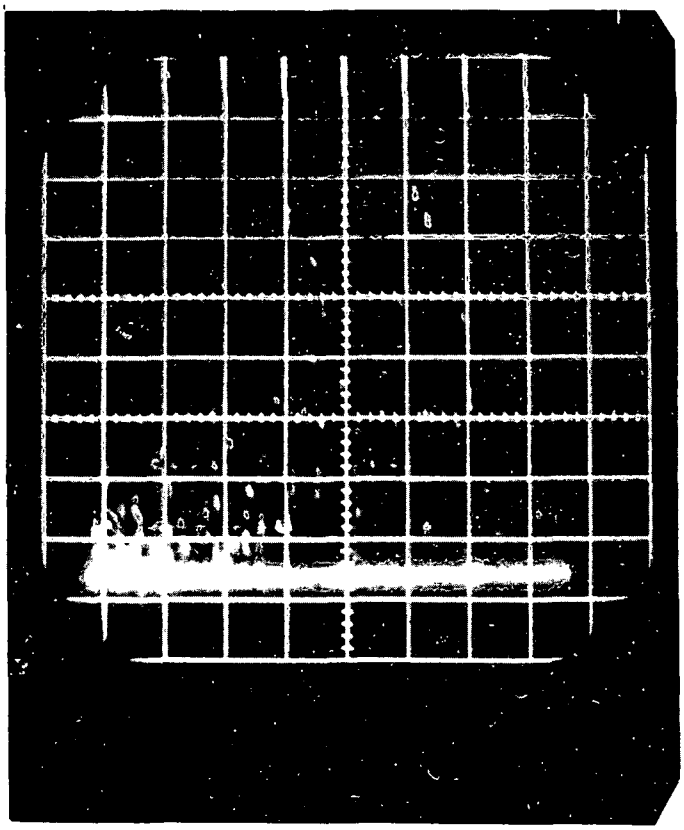

B = 600 gauss
(Unstable)

Figure 23

Langmuir Probe Curves Showing Effect of Strong Instabilities

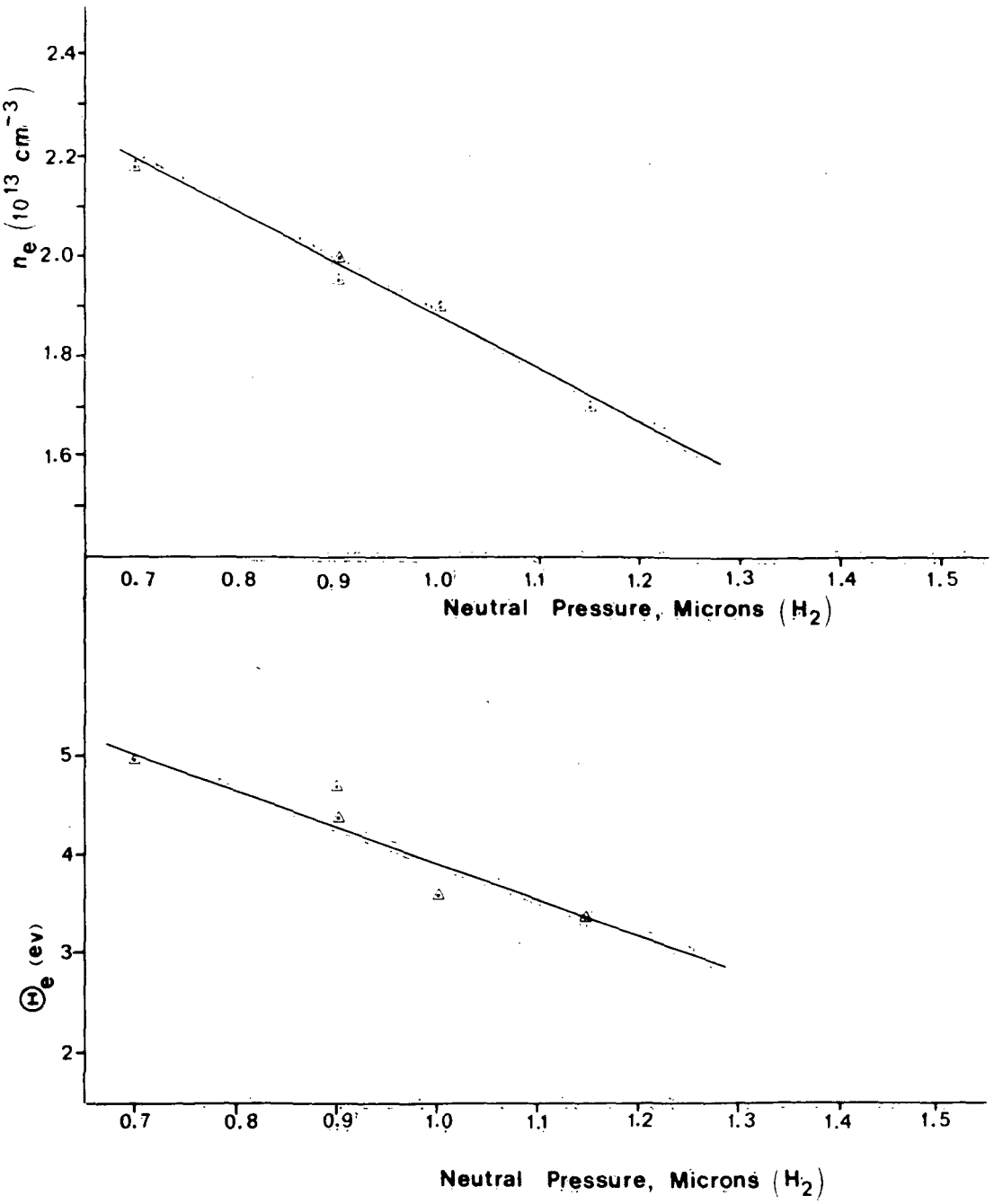

Figure 24

Langmuir Probe Measurements of Density and Temperature Variation with Tube Fill Pressure

in a gas of neutral density n_o and refractive index μ, for radiation of wavelength λ_o. Doppler shifting is present here, too, of course, but the molecular velocities are so small that the thermal doppler half-width can be no more than, say, 0.1 $\mathring{A}$ for a molecular temperature of 10^3 ^oK. Accordingly, in a Thomson scattering environment, the Rayleigh scattering can almost always be thought of as occurring at the laser frequency only.

The Rayleigh cross-section in the scattering plane ($\sin\Psi = 1$) is 2.071×10^{-28} cm^2 for nitrogen and only 0.449×10^{-28} cm^2 for hydrogen, at 6943 $\mathring{A}$. The ratio $d\sigma_T/d\sigma_R$ of the total Thomson to the total Rayleigh cross-sections is therefore 1,720 per atom and electron in hydrogen. The relative magnitude of the observed Thomson and Rayleigh signals at the laser line will depend on the ionization ratio and on the fraction of the total Thomson spectrum admitted by the dispersing instrument. A more useful figure is our measured Rayleigh scattering contribution of about 0.4 photoelectrons per joule-micron (light energy, neutral pressure). In a typical Thomson measurement, our ionization fraction was such that the Rayleigh contribution was no more than 10% of the equipment-scattered light at the laser frequency, or 0.5% of the Thomson signal at the spectrum center.

Therefore, Rayleigh scattering is not an important consideration in analyzing our Thomson results, but it is an extremely useful way of calibrating and fine-aligning the light detection system, as well as checking for drifts in the original filter calibration. For example, through Rayleigh calibration, we find no more than a factor of 2 total difference between calculated and measured absolute scattering magnitudes, a figure which includes absolute error in pressure indicated by our ionization gages.

Rayleigh measurements were made at a pressure of 500μ in dry

nitrogen in order to get a signal of the order of 10^3 photoelectrons at pressures low enough to avoid photoionization of the gas. Pressure was established by a ratio method, at flow rates of order 0.2 liter/sec in the discharge tube.

6.3 Gas Selection

Hydrogen was used for all Thomson measurements to be reported. Among the gases which could be used in a Penning discharge, Table 6-1 lists the best nine in decreasing order of desirability, with regard only to their spectral activity in the Thomson region.

Table 6-1

Spectral Activity of Various Gases in the Interval 6700 Å - 7100 Å, from M.I.T. Wavelength Tables

gas	number of spectral lines, 6700-7100 Å	location of nearest lines	reactive?	easy to use?
1. hydrogen	0	+1,261, -380	no	yes
2. sodium	0	+1,240, -782	yes	no
3. helium	2	+123, -265	no	no
4. rubidium	3	+99, -138	yes	no
5. nitrogen	17	+3, -0	no	no
6. oxygen	5	+59, -32	yes	no
7. chlorine	11	+8, -9	yes	no
8. potassium	4	+21, -5	yes	no
9. neon	8	+81, -13	no	yes

The spectrum of argon contains 35 lines in this interval, although it is a very well-behaved gas for Penning discharges. Either hydrogen or helium might have been used, except that helium is more difficult to use in the discharge.

6.4 Plasma Heating by the Laser

The equivalent fractional increase in electron temperature which can occur via inverse bremsstrahlung during the laser pulse is given by Kunze[47] as:

$$\frac{\Delta\Theta_e}{\Theta_e} = 5.3 \times 10^{-7} \frac{n_i Z^2 g_{ff} \lambda_o^3}{\Theta_e^{3/2}} \left[1-e^{-h\nu_o/kT_e}\right] J \qquad (6\text{-}2)$$

where Θ_e is electron temperature T_e expressed in ev, n_i is ion density, J is laser energy intensity in the scattering region (joules/cm^2), λ_o is the laser wavelength in cm, and g_{ff} is a Gaunt factor which may be approximated by unity for purposes of rough estimation.

This expression is just Spitzer's formula[69] for the inverse bremsstrahlung absorption coefficient for a fully ionized plasma. However, it includes the assumption that electron-electron relaxation times t_{ee} in the plasma are several times smaller than the laser flash duration t_L, which is in turn supposed to be several times smaller than the energy equilibration time t_{ie} for plasma electrons and ions as species. That $t_{ee} < t_L$ in our plasma can be demonstrated with our handy formula for this quantity, also based on Spitzer:

$$t_{ee} \cong 30\Theta_e^{3/2}/n_{el2} \text{ nanoseconds} . \qquad (6\text{-}3)$$

If, for example, $\Theta_e = 3$ ev and $n_{el2} = 20$ ($10^{12} cm^{-3}$), typical values, we find $t_{ee} \sim 7.8$ nanoseconds, so that the usual laser flash persists for 4 or 5 electron relaxation times. Spitzer's formula for t_{ie} gives a time of several microseconds, but the actual time will be closer to hundreds of microseconds in our discharge because the hot ion gyroradii are so large that they instantly escape.

With these provisions, for $n_e \approx n_i$ at $h\nu = 1.79$ ev, Kunze's formula can be simplified to

$$\frac{\Delta\Theta_e}{\Theta_e} \cong 1.8 \times 10^{-7} \left(\frac{n_{el2} J}{\Theta_e^{3/2}}\right)\left[1-e^{-1.79/\Theta_e}\right] \qquad (6\text{-}4)$$

which with our typical energy intensity $J = 150$ joules/cm^2, $\Theta_e = 3$ ev and $n_{el2} = 20$ gives an estimate of the relative heating $\Delta\Theta_e/\Theta_e \sim 5 \times 10^{-5}$. It should be noted that the approach used by Gerry[50] leads to an unnecessarily large estimate for the relative heating.

6.5 Plasma Light

For our hydrogen plasma, bremsstrahlung is expected to be the most important process producing plasma light in the Thomson interval. We employ a formula of Glasstone and Lovberg for the bremsstrahlung production rate, converted to practical units for a hydrogen plasma and for $n_e \approx n_i$:[87]

$$P_\lambda d\lambda \cong 3.9 \times 10^{-12} \frac{n_{el2}^2 \bar{g}}{\sqrt{\Theta_e}} e^{-1.79/\Theta_e} \, d\mathring{A} \text{ watts/cm}^3 \qquad (6\text{-}5)$$

into 4π sterradians. Since our Thomson data will be expressed in units of PMT cathode photoelectrons and since we have not yet taken into account the light collection efficiency of our detection system, a more useful form of (6-5) for direct comparison with measurements is, again writing $\bar{g} = 1$:

$$I_p \cong 1.1 \times 10^{-3} n_{el2}^2 \Theta_e^{-1/2} e^{-1.79/\Theta_e} \tau\eta \, d\Omega \, dV \, d\mathring{A}$$

$$\text{photoelectrons/nanosec.} \qquad (6\text{-}6)$$

In (6-6), τ is the effective filter transmissivity, equal to its absolute integrated transmissivity divided by its bandwidth $d\mathring{A}$ in Angstroms, $d\Omega$ is the viewing solid angle, η is the PMT quantum efficiency and dV is the visible plasma volume (larger than the scattering volume) in cm^3. Inserting the correct values for these quantities, we find for $n_{el2} = 20$ and $\Theta_e = 3$ ev that $I_p = 3 \times 10^{-5}$ p.e./ns. This calculation agrees well with our measurements, which show less than 2×10^{-3} p.e./ns from all sources including the PMT dark current noise discussed in the next section.

6.6 Photomultiplier Produced Noise

The recorded variable is the quantity of charge contained in the PMT anode pulse. Because the PMT has unusually high first dynode gain, the largest single source of statistical or "shot" noise is in the conversion of photons to photoelectrons at the cathode, rather than in electron multiplication.

Accordingly, we expect that since the arrival of N_p photons constitutes N_p Bernoulli trials in which "success" is the production of a photoelectron with probability 0.07, the photoelectron statistics as measured at the anode will be governed by the binomial distribution, with $\eta^* = 0.07$:

$$b(N_e;N_p,\eta) = \binom{N_p}{N_e} \eta^{N_e}(1-\eta)^{(N_p-N_e)} \quad . \tag{6-7}$$

Further, we expect that the normal density will be a good approximation to the binomial distribution for most of our conditions, so that the expected standard deviation of the number of photoelectrons received due to the arrival of N_p photons will be

*This is the photocathode quantum efficiency.

$$\sigma = \sqrt{N\bar{\eta}(1-\bar{\eta})} \approx \sqrt{N\bar{\eta}} = \sqrt{N_e} \ , \qquad (6\text{-}8)$$

where N_e is the total number of photoelectrons received, whether in a single shot or over a number of shots. Accordingly, at regions of very small signal, a sufficient number of shots is taken to reduce the standard deviation to a reasonable level.

With no light input, a photomultiplier cathode or dynode produces a very small thermal current which is called the "dark current" when it is measured in amplified form at the PMT anode. At the tube operating temperature of 15°C, and an operating voltage of 2350 V, the PMT dark current is only 50 nanoamperes. Referred back to the cathode, the equivalent dark photoelectron production rate is then only 6×10^{-6} p.e./ns, which is entirely ignorable for our purposes.

6.7 Plotting Thomson Data

We are very fortunate in having designed an experiment in which the statistical noise expressed by (6-8) is the only significant source of noise which must be dealt with over the scattered spectrum. Of course, equipment-scattered light including Rayleigh scattering is present at the spectrum center, and must be subtracted. In general, this has been measured repeatedly in each Thomson series, and its standard deviation is very low compared to that of the signal. In any case, the amount subtracted is plotted along with each scattered spectrum reported, and labeled "ESL".

To take data, Langmuir measurements were initially employed as described earlier to locate an operating point giving sufficient density and temperature to allow measurements. The plasma discharge was then fired recurrently at about 1 pps for 3 or 4 hours to permit sputtered impurities to be flushed out of the system. This could be verified when

no change in tube pressure resulted from firing the discharge. Then, Thomson measurements were made at each wavelength listed on a precalculated shot schedule. This schedule was arranged so that approximately 7 measurements would be made on each side of the spectrum, including at least 2 at the center and 2 in the extreme wings, for each of the two scattered spectra ($\parallel$ and $\perp$) to be measured in one series. The schedule sequence begins at the spectrum center and moves through the blue wing, then returns to the spectrum center and moves through the red wing, always alternating between a point for the parallel and a point for the perpendicular spectra. Each "point" in these measurements consisted of from 10 to 20 repeated shots, the number required depending on received signal strength and our estimate of the desirable standard deviation.

Since this procedure already sounds like the tale of the man going to St. Ives, we might mention that a typical "series", leading to one curve each for the parallel and perpendicular spectra, required approximately 1,000 shots, 40 rolls of Polaroid film and 10 hours to complete. This, in fact, is the reason for the complicated procedure listed above. We trust our measurements because the same signal was found in all cases upon returning to the spectrum center after 5 hours spent in the blue wing. Some examples of scattering data are reproduced in Figure 25.

Later, the signals were read off the Polaroid prints, numerically averaged for each measurement wavelength, and corrected for ESL and for changing filter integrated transmissivity and laser output energy. The resulting values, normalized to normal incidence transmissivity and 1 joule of light, are plotted on a linear scale versus $[\Delta\lambda/\sin(\theta/2)]$. After finding the wavelength around which the plotted values were symmetrically distributed, the logarithm of signal strength was replotted versus $[\Delta\lambda/\sin(\theta/2)]^2$. It will be seen from equation (2-30) that such

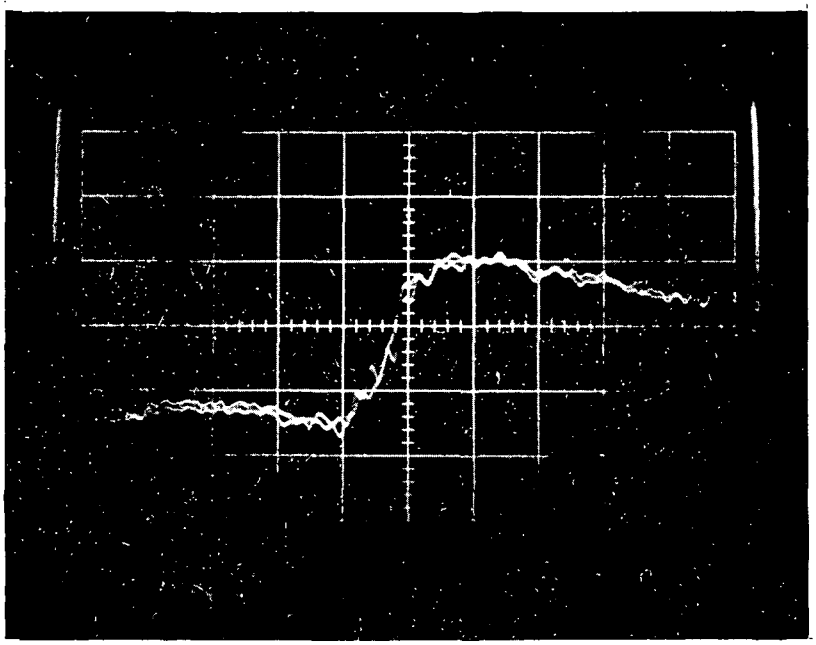

Scattered Energy Signal
(2 shots)
Vertical: ~ 5 photoelectrons
per division
Horizontal: 20 ns/division

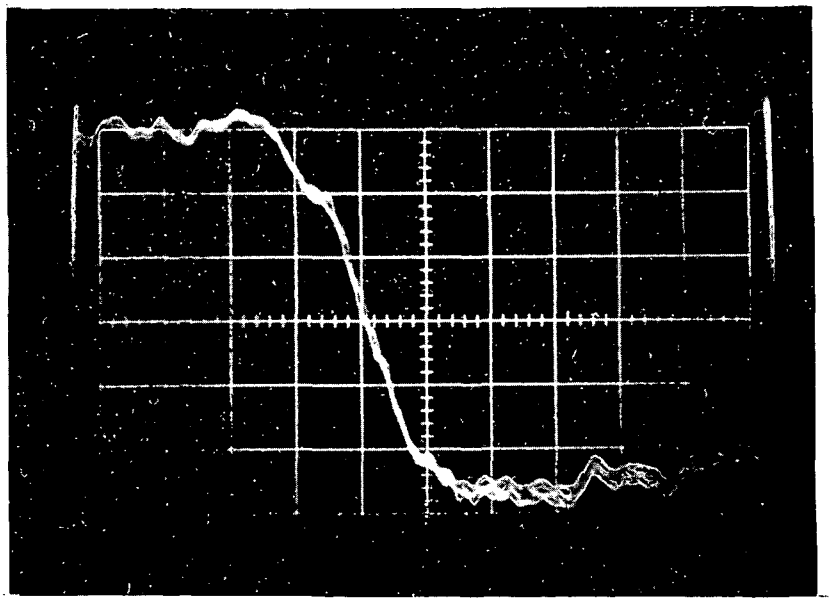

Laser Energy Monitor
Signal (5 shots)
Vertical: 0.2 joules/division
Horizontal: 20 ns/division

Figure 25

Examples of Scattering Data

a curve will lie on a straight line of slope equal to $-(a\Theta_e)^{-1}$, if the electrons are Maxwellian. For a plot on decilog paper, a = 1738.

In fact, all our measurements show a Maxwellian plasma, except the last, for which the discharge was deliberately operated above the critical field for instability. Even for this case, the data conversion method used here was the most appropriate.

7. ACTUAL THOMSON SCATTERING RESULTS

7.1 Data Presentation

A total of four measurement series were completed, each consisting of a parallel and a perpendicular distribution measurement. All were made at the plasma column center. The first series, however, featured a smaller sampling volume than the last three. For series 1, the sampling cylinder is 3.0 mm and 5.3 mm in length for the longitudinal and transverse parts, respectively. This is the only complete series in which the $\perp$ and $\parallel$ data were not interleaved. Series 2, 3 and 4 were made with a cylinder length of 8.5 mm. The sampling cylinder has a diameter of 1 mm, determined by the laser beam waist. Total plasma diameter along the cylinder direction is more than 4 times the cylinder length.

Discharge time for all measurements is 25 μsec before the cessation of discharge current. Magnetic field strength is a uniform 190 gauss for series 1-3 and 450 gauss for series 4, where we deliberately exceeded the critical field for plasma instability. Neutral pressure varies among the series, and is listed for each set of figures.

Series 1 was our very first successful Thomson measurement (Figures 26-28). At that time, we thought we would have to be satisfied with a signal strength of 5-10 photoelectrons per shot, and so completed our only high temperature measurement. In succeeding measurements, this was never attempted, since high temperatures go with low densities and the two effects together reduce signal strength to masochistic levels. While the standard deviations achieved in this series are not impressive, better results would most likely have been impossible with our apparatus. Within experimental error, series 1 shows two equal temperature Maxwellians with a temperature of about 5 ev. The most extreme point on

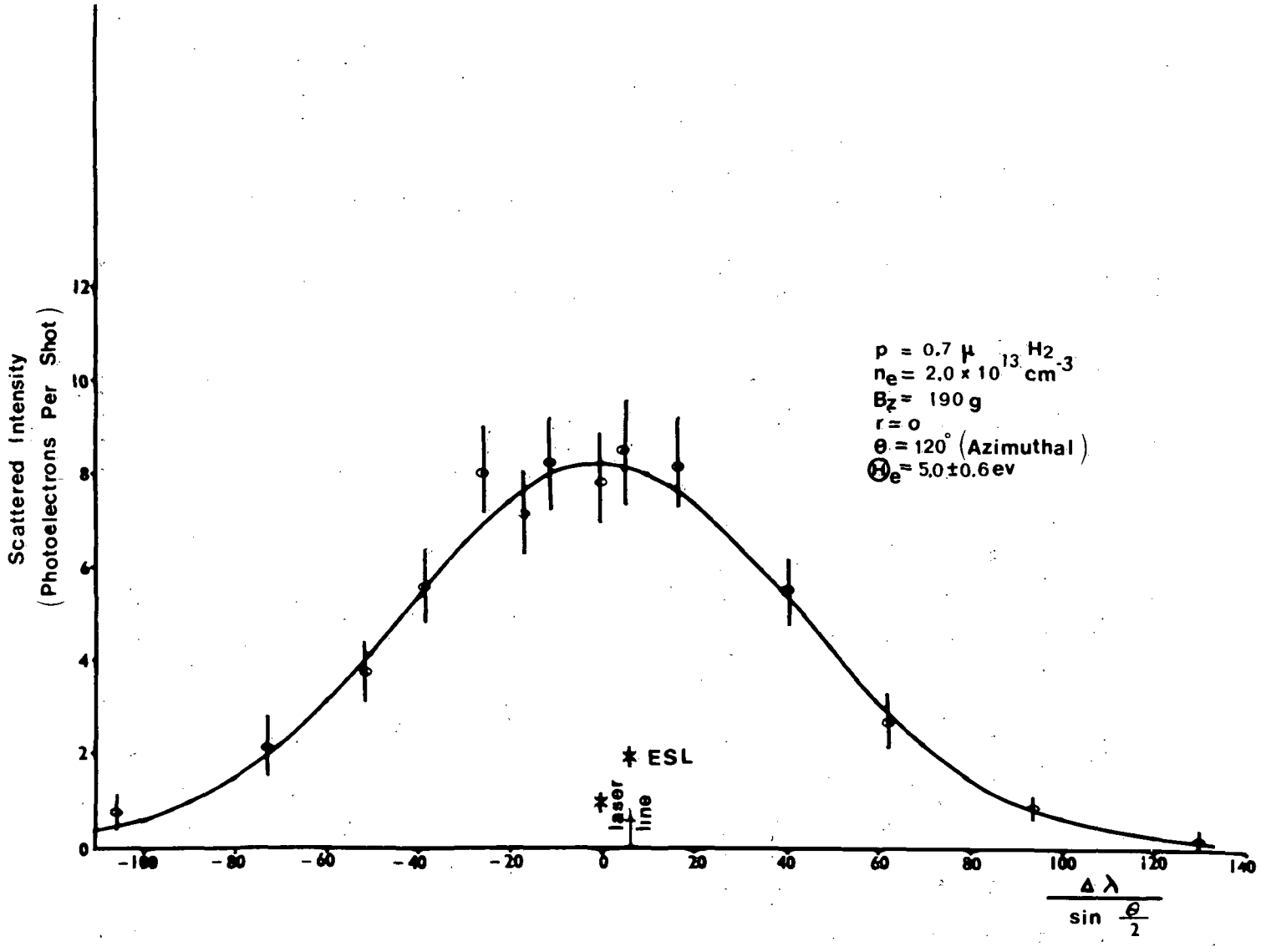

Figure 26

Series 1, Azimuthal Distribution

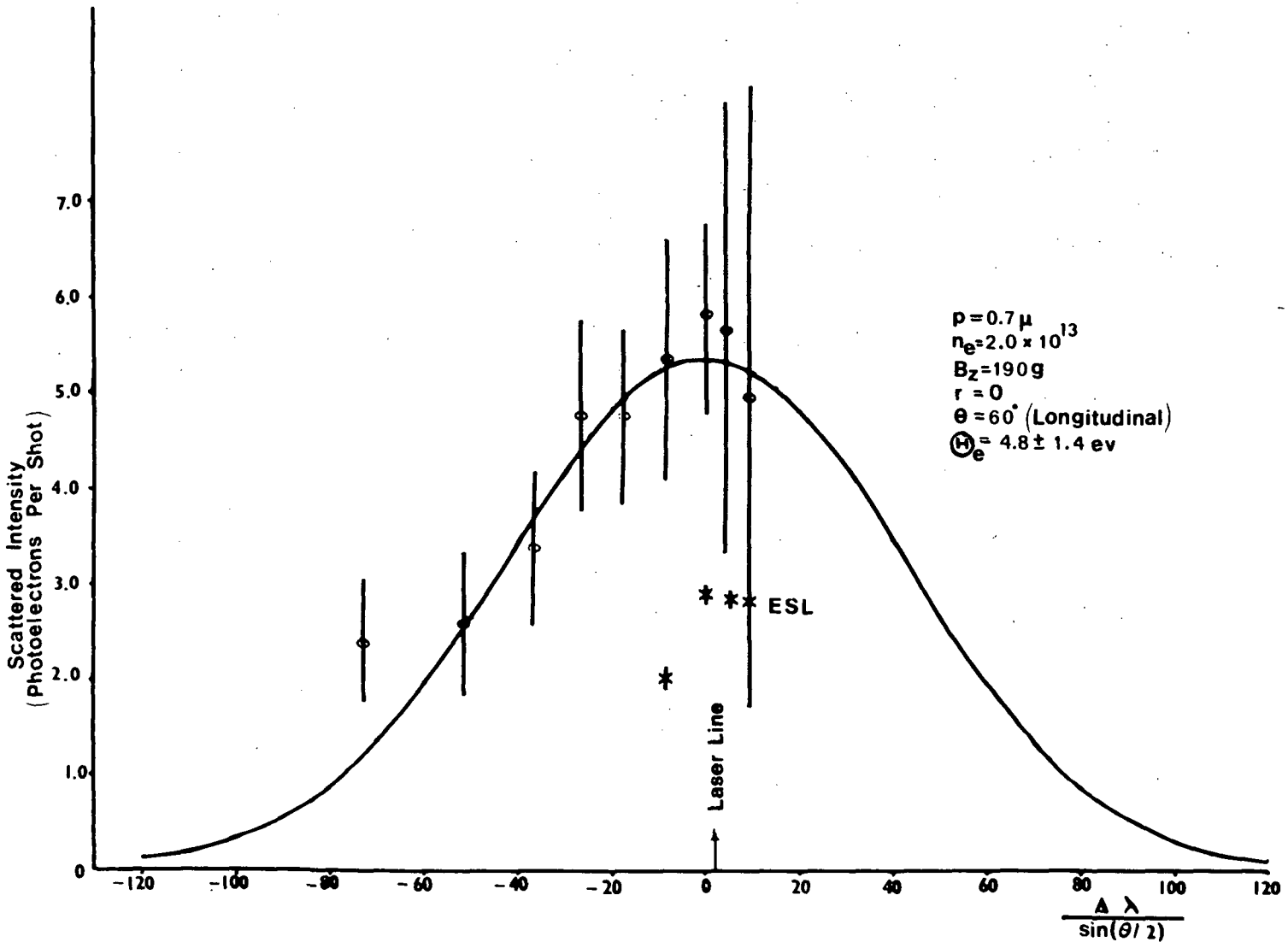

Figure 27

Series 1, Longitudinal Distribution

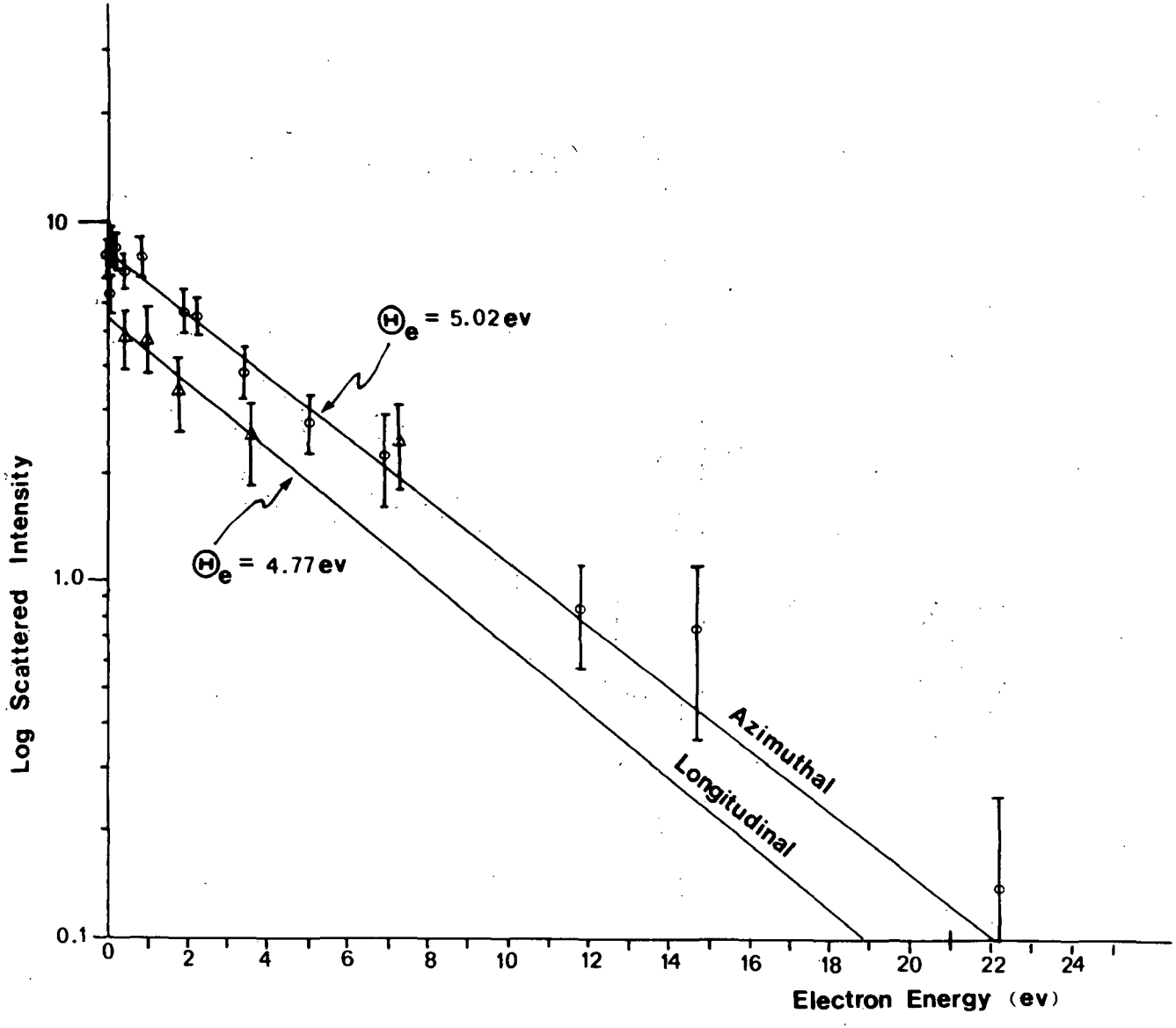

Figure 28

Series 1, Logarithmic Plot

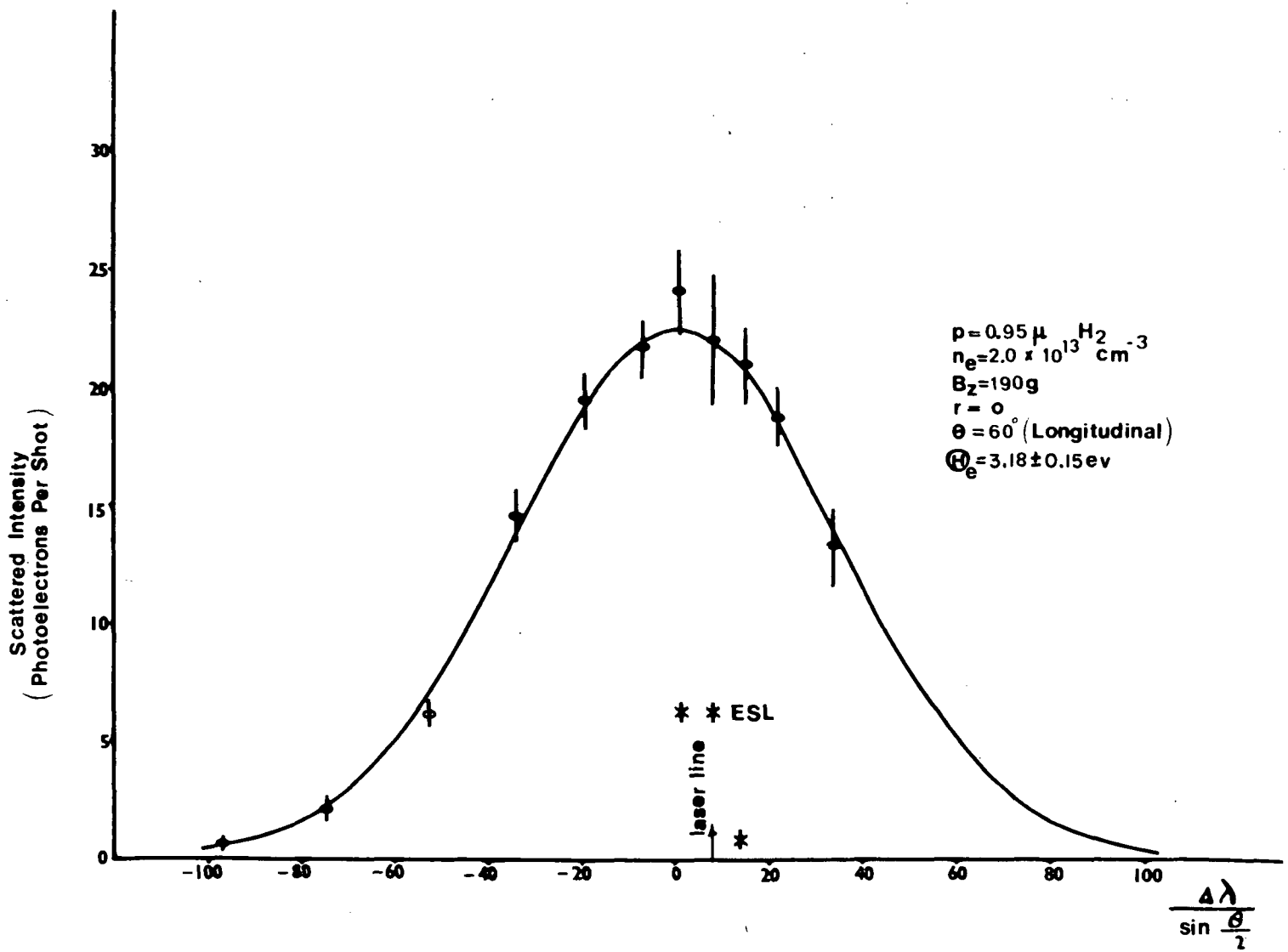

Figure 29

Series 2, Longitudinal Distribution

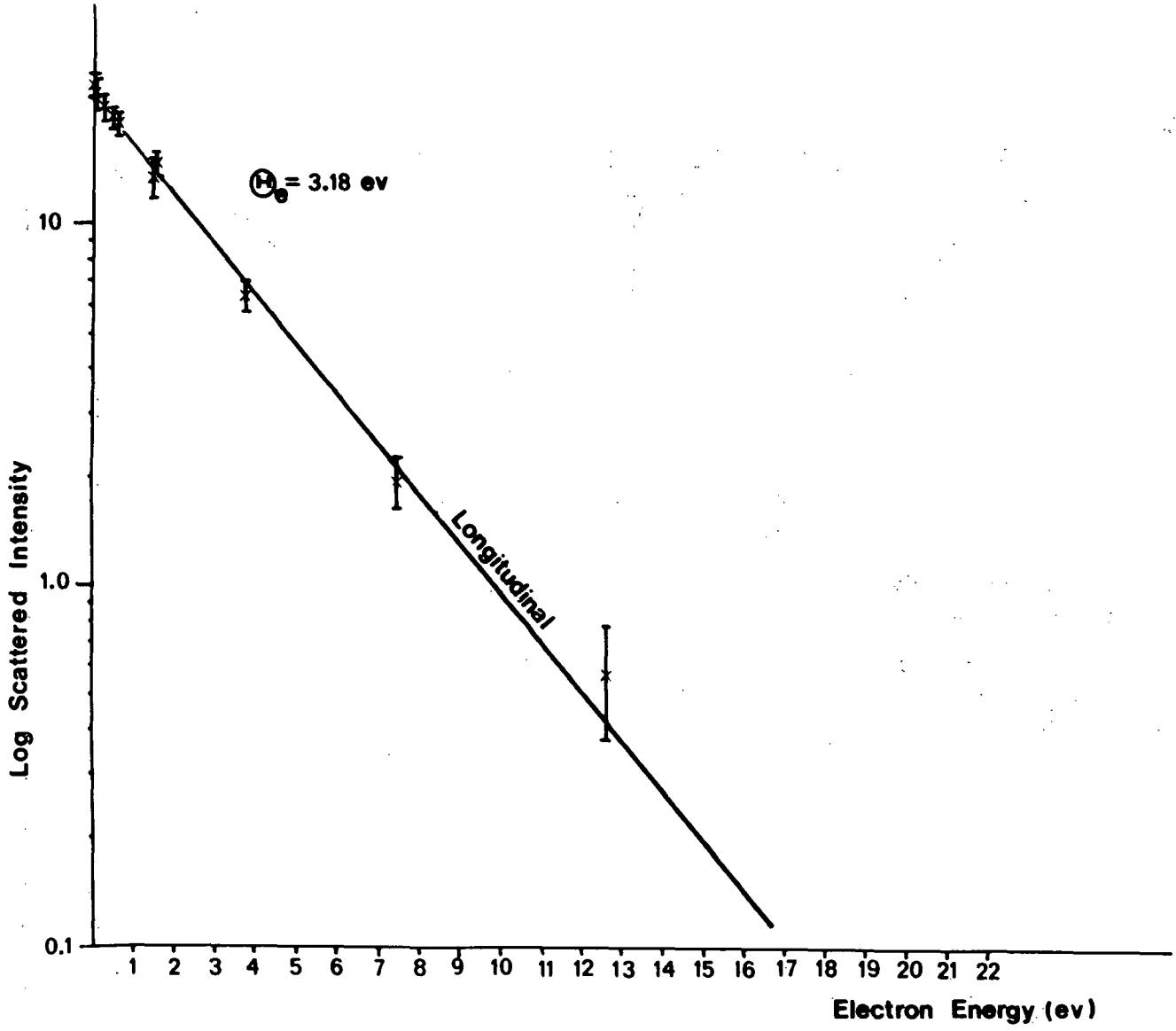

Figure 30

Series 2, Logarithmic Plot

the transverse plot is significant because of its very low magnitude, 0.15 ± 0.15 p.e./shot. This point represents an average incidence of 2 photons per shot.

Series 2 is an isolated longitudinal plot (see Figures 29, 30) which could not be accompanied by a transverse measurement due to laser failure. It is included because it is the first instance of what we consider good standard deviation in the results. The accompanying log plot (Figure 30) shows that a single temperature of 3.18 ev can describe all points on this curve, out to electron energies of about 13 ev.

Series 3 (refer to Figures 31-33) is our best overall pair of measurements, showing excellent standard deviation and little if any serious evidence of the high energy tails to be found in series 4. Single temperatures describe all points on both curves out to electron energies as large as 6 times the thermal energy, and these temperatures are equal within experimental error. These temperatures are 3.0 ± 0.3 ev for the perpendicular distribution and 3.2 ± 0.2 ev for the parallel distribution. The measurements on these plots show Maxwellian behavior over a much broader range than has ever been seen before in Thomson scattering.

Series 4 (Figures 34-37) provides by far the most interesting of our results. It is immediately clear from either log plot that a straight line will not fit the data within experimental error. In fact, the distributions have quite large high energy tails, so that a free-form curve drawn through the data points has a tangent line at zero energy corresponding to about 2 ev, while in the wings of the distributions, the tangent line slope is 15 to 20 ev in both cases. It is worth noting that the transverse plot has lower "central temperature" and higher "wing temperature" than the longitudinal plot.

The accompaning gaussian curves on the linear plots (Figures 34 and 36) for the two directions correspond to a temperature of 2.27 and

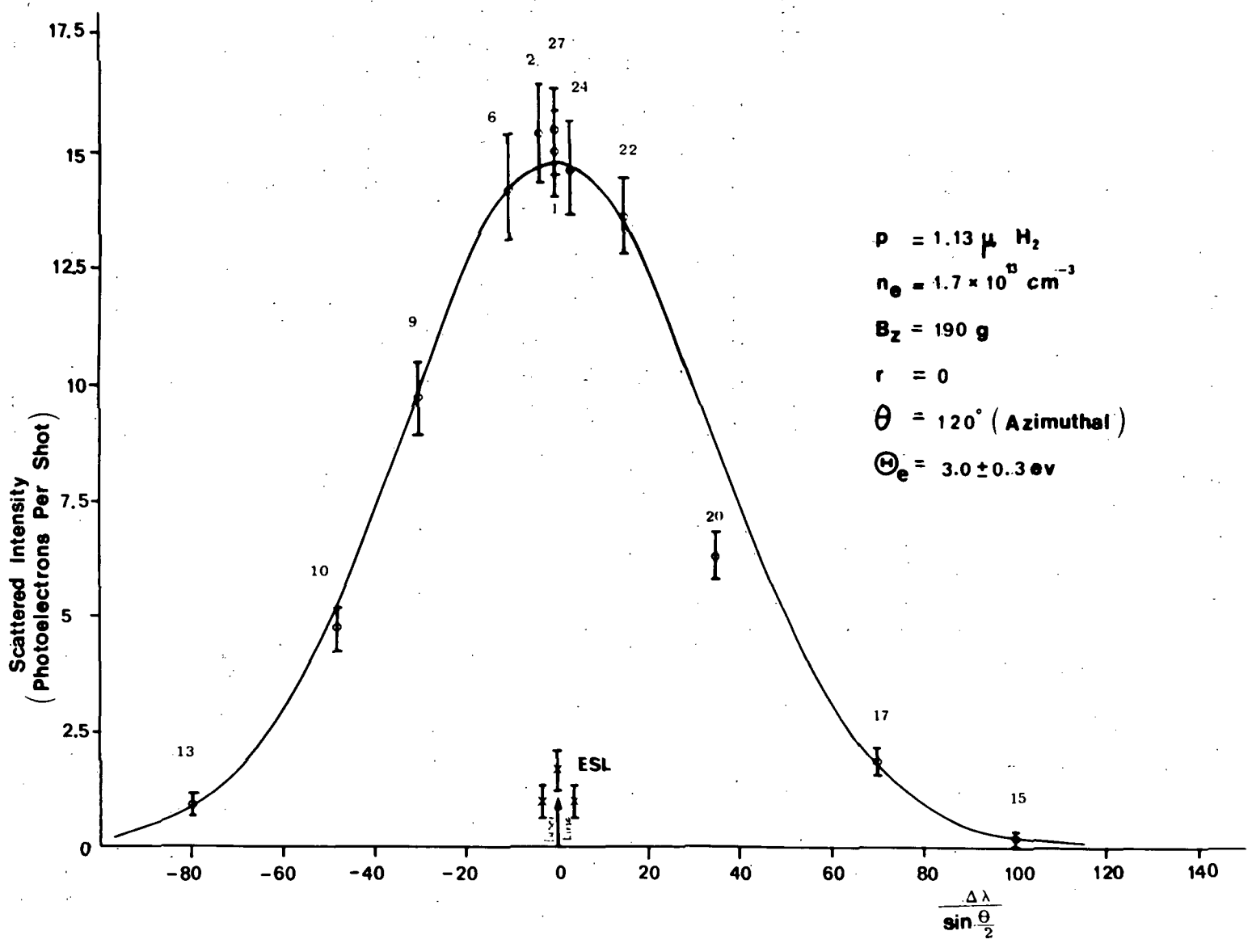

Figure 31

Series 3, Azimuthal Distribution

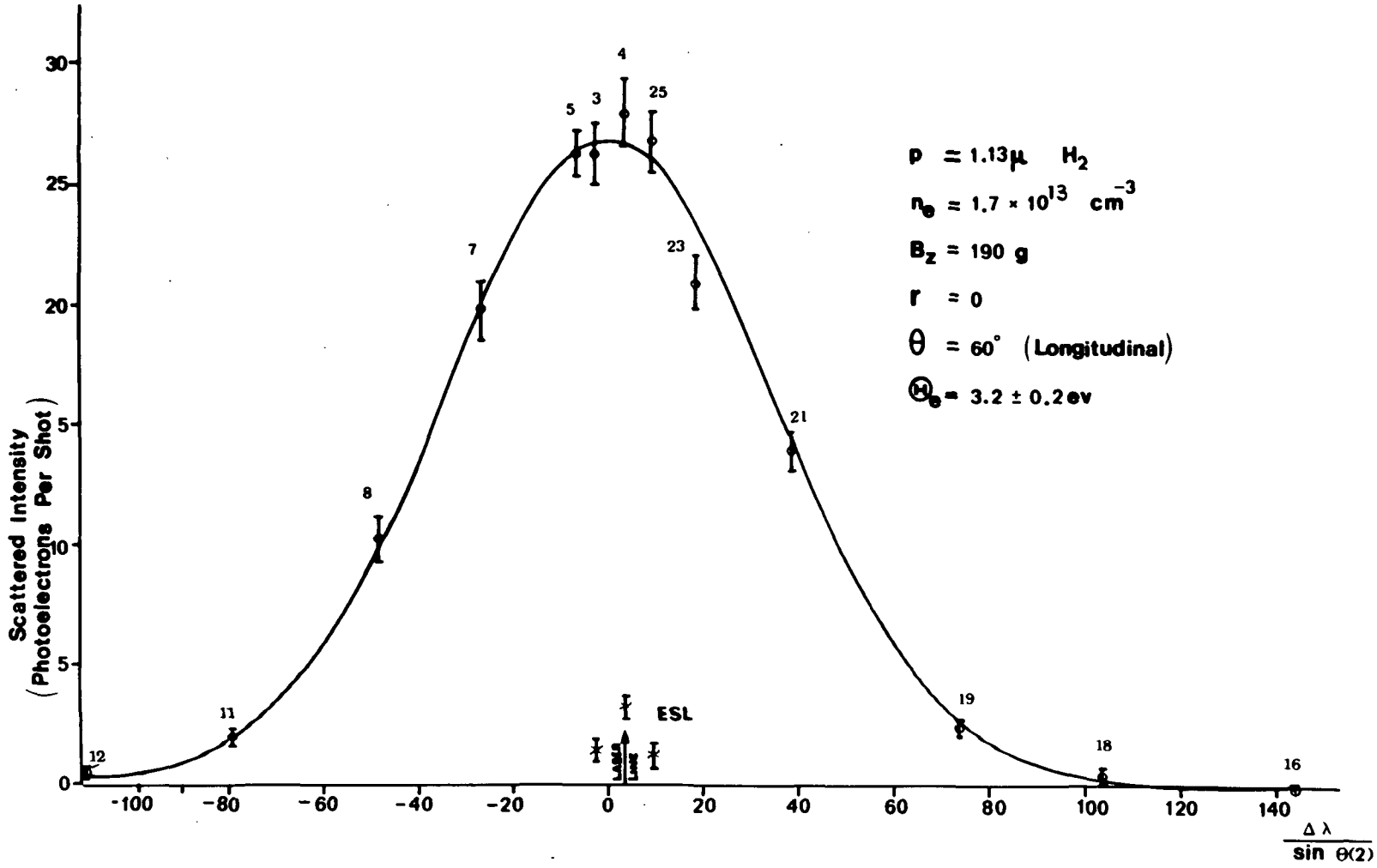

Figure 32

Series 3, Longitudinal Distribution

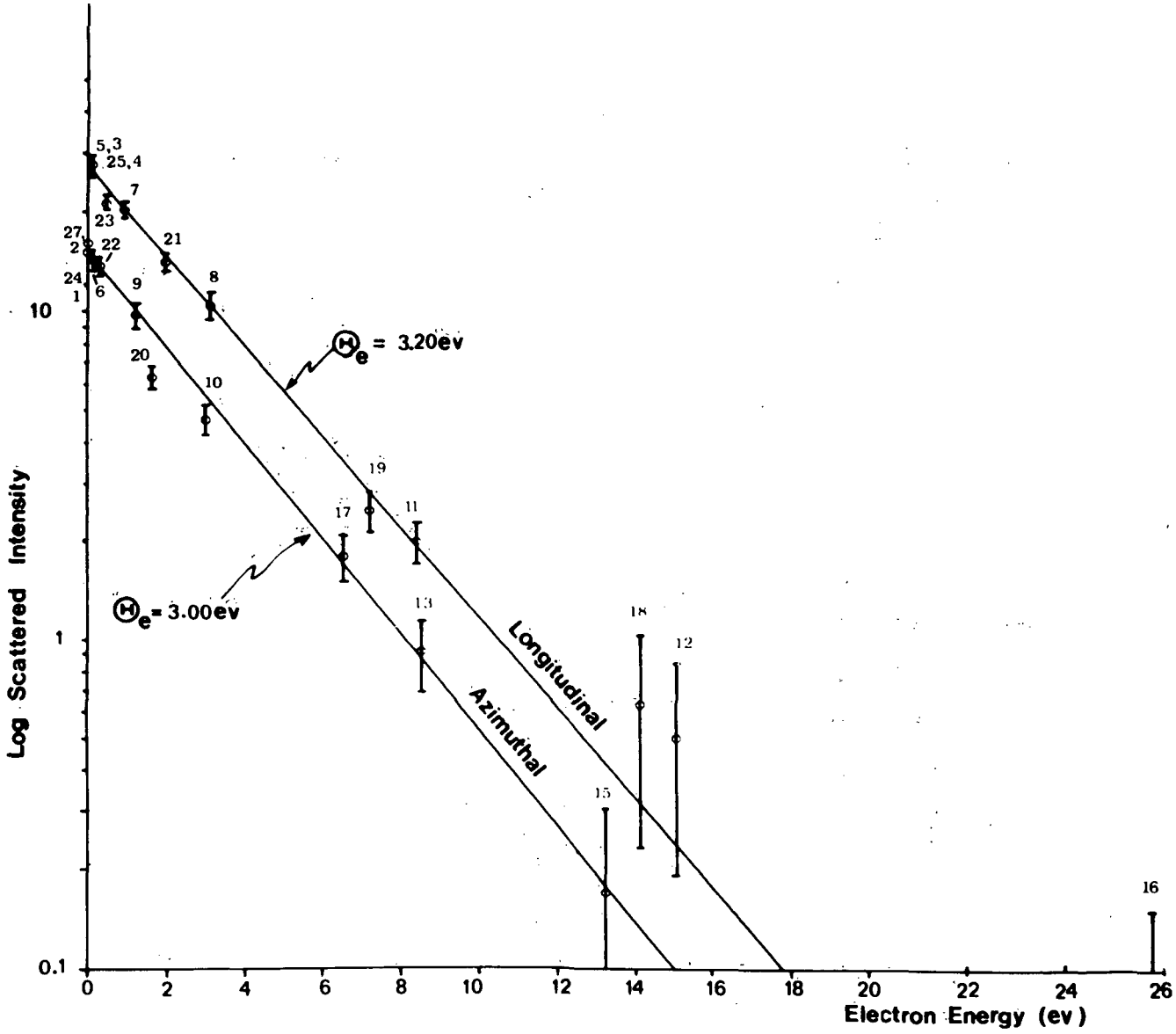

Figure 33

Series 3, Logarithmic Plot

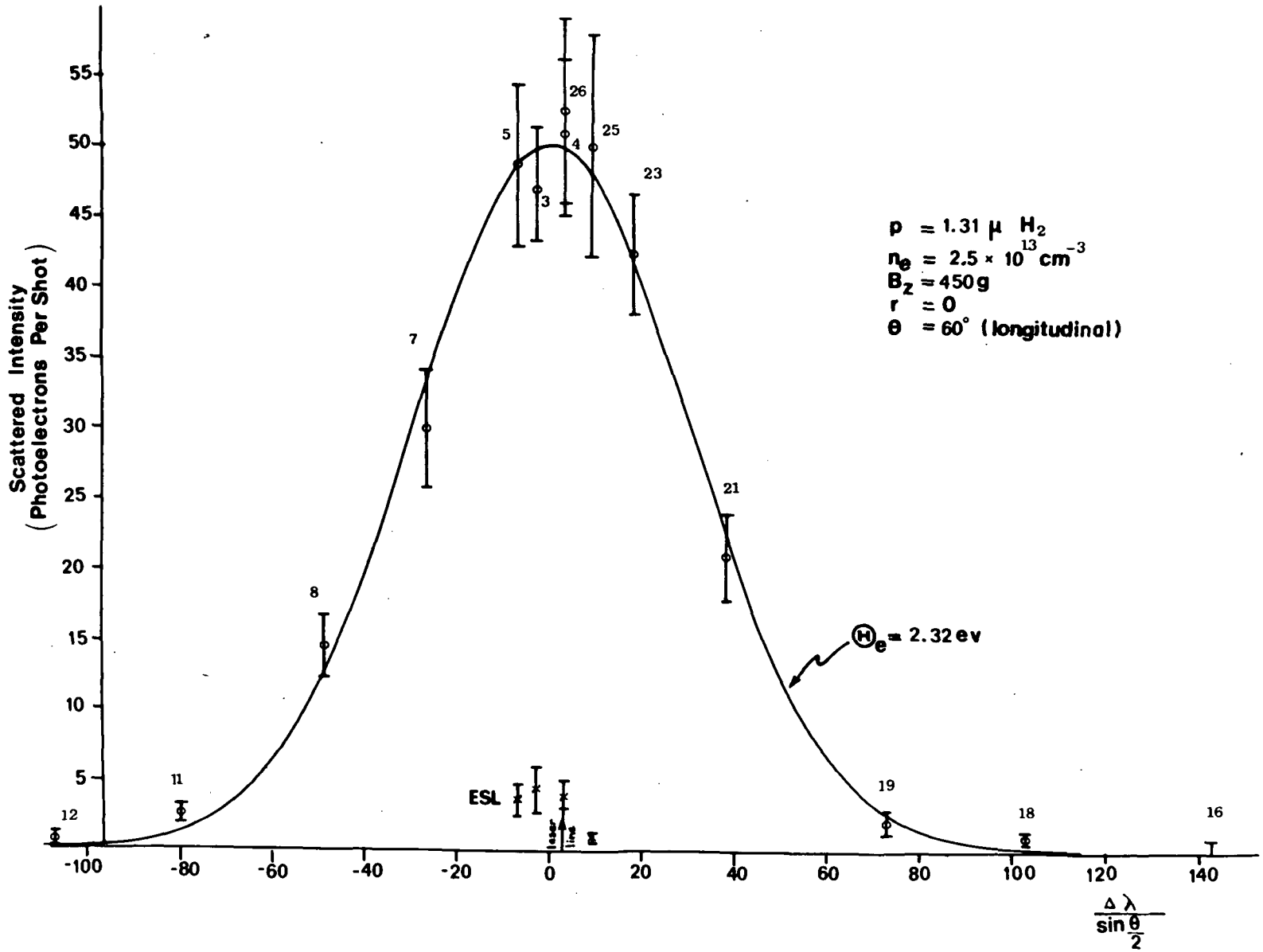

Figure 34

Series 4, Longitudinal Distribution

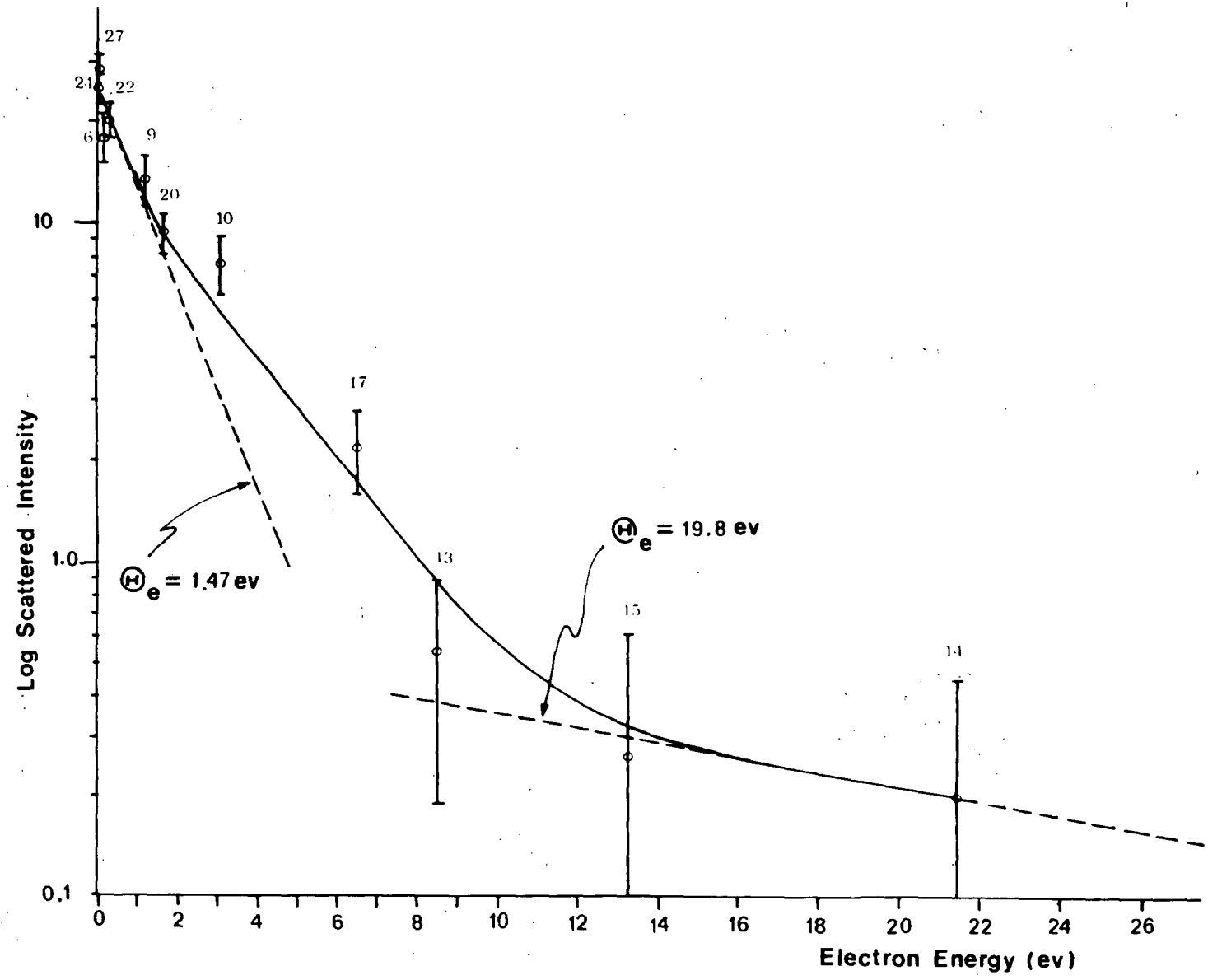

Figure 35

Series 4, Logarithmic Plot of Longitudinal Data

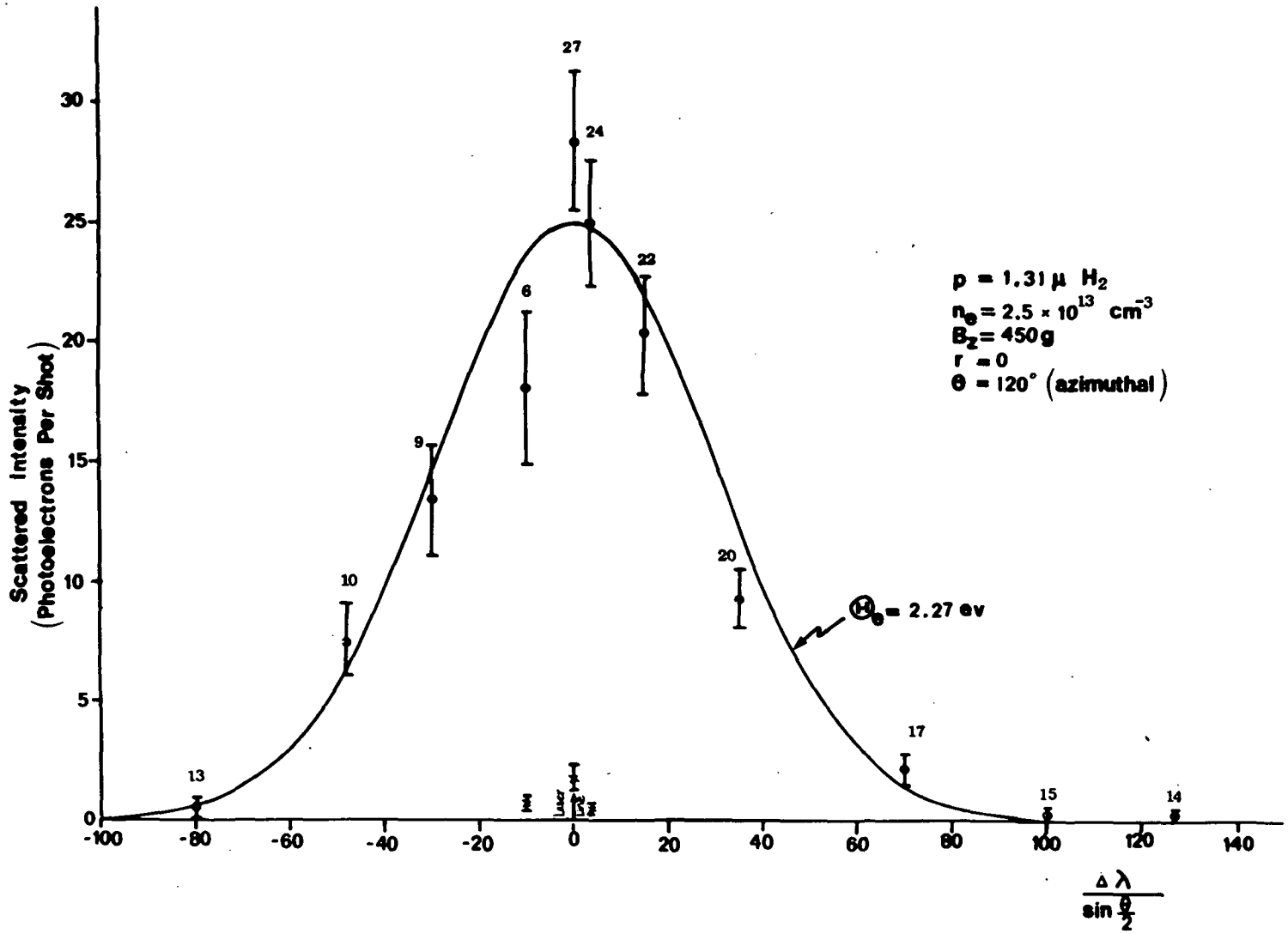

Figure 36

Series 4, Azimuthal Distribution

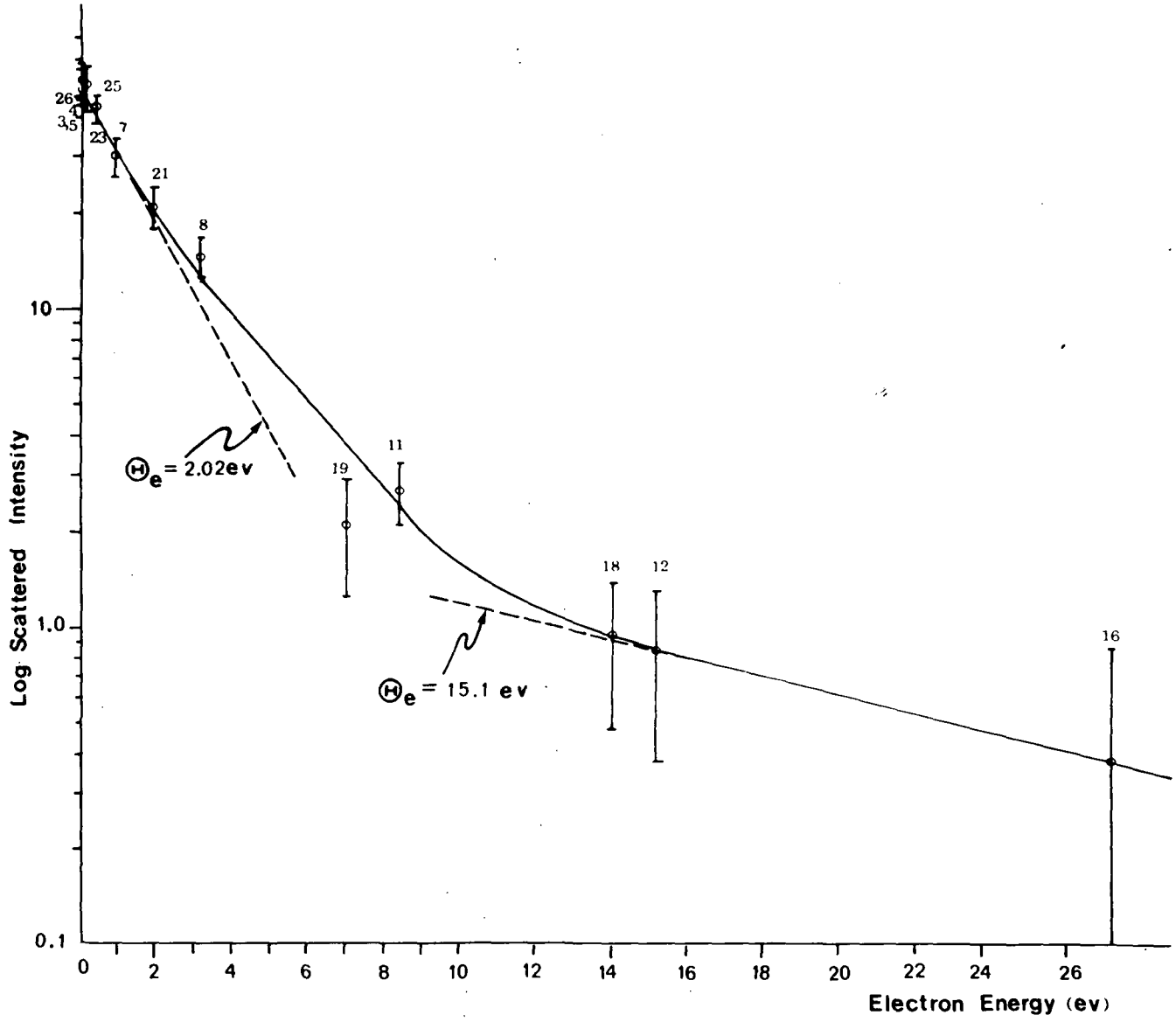

Figure 37

Series 4, Logarithmic Plot of Azimuthal Data

2.32 ev, respectively. These were chosen as the best fit to the low energy data points in each log plot, and are meant to demonstrate the excessive electron numbers in the wings. However, the log plot is more dramatic for this purpose.

This is the first time that measurements showing this behavior have been made using Thomson scattering. Of course, the standard deviations are much worse in series 4 because of the chaotic conditions in the plasma they represent. Nevertheless, one should keep in mind the near impossibility of making measurements in this regime by any other means. To put this point in perspective, we again refer to Figure 22, which shows a Langmuir trace taken under the same conditions.

7.2 Data Summary and Suggestions for Future Work

These measurements demonstrate nearly identical behavior in the electron velocity distributions parallel and perpendicular to the magnetic field direction in a highly ionized Penning discharge in hydrogen. Even when the discharge is operated so as to encourage the Hoh instability, the same general behavior is found between the distributions, with the exception that the azimuthal distribution seems to have the lower central temperature and the higher wing temperature of the two. Otherwise, when a Maxwellian exists (series 1,2 and 3), the temperatures found are equal to within experimental error and agree well with Langmuir probe measurements taken under the same conditions.

These results are quite different from those found by Koons and Fiocco[63,64] but, as explained earlier, the conditions of their experiment were quite different from our own. On the other hand, our results agree qualitatively with those being obtained by McCormick[65] on a highly ionized hollow cathode arc discharge in argon.

We are not surprised by the findings. On the contrary, the electrons should thermalize very rapidly in this discharge at points relatively far from the chaotic cathode fall region near the electrodes.

Qualitatively, this experiment is the best yet reported in the following areas:

(1) Equipment scattered light is several orders of magnitude below other comparable experiments, due to careful design of stray light trapping systems.

(2) This is the first Thomson experiment to measure Maxwellian behavior over a range from zero to 6 thermal energies.

(3) This is the first Thomson experiment to clearly show non-Maxwellian behavior in a Penning discharge plasma.

Also, it can be deduced from the data that good $\bar{k}$-space resolution can be had in a Thomson scattering measurement, and yet permit measurements out to at least one thermal energy for electron densities as low as 10^{12} cm^{-3}. Of course, densities down to 10^{11} cm^{-3} or lower could be permitted in an isotropic plasma where light collection from many directions is possible. The idea that Thomson scattering may not be used below 10^{13} cm^{-3} is just a myth.

Up to this point, we have not commented on the apparent slight zero offset toward the blue shown in most of our data. It is not clear to us if it is significantly larger than the experimental error, since this error could arise from so many different parameters. Nevertheless, where it occurs, it always occurs in the same direction, and amounts to only 3 or 4 $\mathring{A}$. It could be due to net electron drift, since it occurs with one exception (series 1, azimuthal) in the longitudinal distribution. If this is the case, the magnitude of such a drift would be of order 10^{7} cm/sec.

We note here that this technique is completely capable of demonstrating plateaus or "bump in tail" effects in the electron velocity distribution, such as discussed in the theory[88]. It would be particularly interesting to extend Thomson measurements to much lower densities, in order to observe longer-lived behavior of this sort than we have found. Such experiments could be done, since at the very low densities the plasma heating limit is much less severe (see 6-4), allowing the use of very high laser energies provided that (6-3) is observed and the laser power kept constant. For example, a plasma with temperature 3 ev but density 10^{10} cm^{-3} could be observed by our optics using a 10^3 joule laser with a 30 microsecond pulse length, without altering the heating fraction of 5×10^{-5} which we obtain. Lower densities yet could be observed by increasing the light collection solid angle by 10^2 to 1 sr. One must be careful, however, to maintain $n_e D_e^3 > 1$ unless consideration is given to the consequences.

17. J.J. Thomson, Conduction of Electricity Through Gases, Volume II, 3rd Edition, Cambridge University Press, 1933, p. 257 and ff.

18. G. Mie, Ann. Physik, 25, 377 (1908).

19. S. Ichimaru, "Theory of Fluctuations in a Plasma," Annals of Physics, 20, 78 (1962).

20. A.I. Akhiezer, I.G. Prokhoda and A.G. Sitenko, "Scattering of Electromagnetic Waves in a Plasma," Sov. Phys. JETP, 6, 576 (1958).

21. I.B. Bernstein, S.K. Trehan and M.P.H. Weenink, "Plasma Oscillations: II. Kinetic Theory of Waves in Plasmas," Nuclear Fusion, 4, 61 (1964).

22. W.H. Kegel, "Light Scattering from Plasmas with a Non-Maxwellian Velocity Distribution," Plasma Physics, 12, 295 (1970).

23. J. Weinstock, "New Approach to the Theory of Fluctuations in a Plasma," Phys. Rev., 139A, 388 (1965).

24. E.C. Taylor and G.G. Comisar, "Frequency Spectrum of Thermal Fluctuations in Plasmas," Phys. Rev. 132, 2379 (1963).

25. A.G. Sitenko and A.A. Gurin, "Effect of Particle Collisions on Plasma Fluctuations," Sov. Phys. JETP, 22, 1089 (1966).

26. A. Ron, J. Dawson and C. Oberman, "Influence of Collisions on Scattering of Electromagnetic Waves by Plasma Fluctuations," Phys. Rev., 132, 497 (1963).

27. T. Hagfors, "Density Fluctuations in a Plasma in a Magnetic Field, with Applications to the Ionosphere," J. Geophys. Res., 66, 1699 (1961).

28. P.M. Platzman and P.A. Wolff, "Light Scattering from a Plasma in a Magnetic Field," Phys. Rev. 174, 489 (1968).

29. P.G. Corolan and D.E. Evans, "Influence of Symmetry About the Magnetic Vector on the Spectrum of Light Scattered by a Magnetized Plasma," Plasma Physics, 13, 947 (1971).

30. T.S. Brown and D.J. Rose, "Plasma Diagnostics Using Lasers: Relations between Scattered Spectrum and Electron-Velocity Distribution," J. Appl. Phys. 37, 2709 (1966).

31. R.A. Pappert, "Incoherent Scatter from a Hot Plasma," Phys. Fluids, 6, 1452 (1963).

32. R.E. Pechacek and A.W. Trivelpiece, "Electromagnetic Wave Scattering from a High-Temperature Plasma," Phys. Fluids, 10, 1688 (1967).

33. O. Theimer and J.E. Sollid, "Relativistic Corrections to the Light-Scattering Spectrum of a Plasma," Phys. Rev., 176, 198 (1968).

REFERENCES

1. E. Thompson, M.I.T. Res. Lab. of Electronics Quarterly Progress Report No. 68, 74 (January 15, 1963).

2. G. Fiocco and E. Thompson, "Thomson Scattering of Optical Radiation from an Electron Beam," Phys. Rev. Lett., 10, 89 (1963).

3. K.L. Bowles, "Observation of Vertical-Incidence Scatter from the Ionosphere at 41 Mc/sec," Phys. Rev. Lett., 1, 454 (1958).

4. W.E. Gordon, "Incoherent Scattering of Radio Waves by Free Electrons with Applications to Space Exploration by Radar," Proc. I.R.E., 46, 1824 (1958).

5. K.L. Bowles, National Bureau of Standards Report 6070 (1959).

6. J.A. Fejer, "Scattering of Radio Waves by an Ionized Gas in Thermal Equilibrium, " Can. J. Phys., 38, 1114 (1960).

7. J.A. Fejer, "Scattering of Radio Waves by an Ionized Gas in Thermal Equilibrium in the Presence of a Uniform Magnetic Field," Can. J. Phys., 30, 716 (1961).

8. J.P. Dougherty and D.T. Farley, "A Theory of Incoherent Scattering of Radio Waves by a Plasma," Proc. Roy. Soc. London, 259A, 79 (1960).

9. J.P. Dougherty and D.T. Farley, "A Theory of Incoherent Scattering of Radio Waves by a Plasma," J. Geophys. Res., 68, 5473 (1963).

10. E.E. Salpeter, "Electron Density Fluctuations in a Plasma," Phys. Rev., 120, 1528 (1960).

11. E.E. Salpeter, "Plasma Density Fluctuations in a Magnetic Field," Phys. Rev., 122, 1663 (1961).

12. E.E. Salpeter, "Density Fluctuations in a Nonequilibrium Plasma," J. Geophys. Res., 68, 1321 (1963).

13. K.L. Bowles, "Incoherent Scattering by Free Electrons as a Technique for Studying the Ionosphere and Exosphere; Some Observations and Theoretical Considerations," J. Res. N.B.S., 65D, 1 (1961).

14. M.N. Rosenbluth and N. Rostoker, "Scattering of Electromagnetic Waves by a Nonequilibrium Plasma," Phys. Fluids, 5, 776 (1962).

15. O. Buneman, "Scattering of Radiation by the Fluctuations in a Non-equilibrium Plasma," J. Geophys. Res., 67, 2050 (1962).

16. J. Renau, "Notes on Number Density Fluctuations and the Scattering Cross Section for Electromagnetic Waves Scattered from a Thermal Nonequilibrium Plasma," Zeit. für Phys., 177, 458 (1964).

34. E.T. Gerry and R.M. Patrick, "Thomson Scattering Computations for Laboratory Plasmas," Phys. Fluids, 8, 208 (1965).

35. J.H. Williamson, R.A. Nodwell and A.J. Barnard, "Computed Profiles for Electromagnetic Radiation Scattered from a Plasma," J. Quant. Spect. Rad. Trans., 6, 895 (1966).

36. E. Thompson and G. Fiocco, "Measurements of Large-Angle Scattering of Laser Radiation from D. C. Plasmas," CR VIth Conf. Internat. Phoenomenes d'Ionisation dans les Gas, Paris, SERMA, 4, 111 (1963).

37. E. Fünfer, W.H. Kegel, B. Kronast and H.J. Kunze, "Local Determination of Plasma Parameters in a θ-Pinch Plasma by Light Scattering Experiments," CR VIth Conf. Internat. Phenomenes d'Ionisation dans les Gas, Paris, SERMA, 4, 119 (1963).

38. H.J. Kunze, E. Fünfer, B. Kronast and W.H. Kegel, "Measurement of the Spectral Distribution of Light Scattered by a θ-Pinch Plasma," Phys. Lett., 11, 42 (1964).

39. A.W. DeSilva, D.E. Evans and M.J. Forrest, "Observation of Thomson and Co-operative Scattering of Ruby Laser Light by a Plasma," Nature, 203, 1321 (1964).

40. P.W. Chan and R.A. Nodwell,"Collective Scattering of Laser Light by a Plasma," Phys. Rev. Lett., 16, 122 (1966).

41. S.A. Ramsden and W.E.R. Davies, "Observation of Cooperative Effects in the Scattering of a Laser Beam from a Plasma," Phys. Rev. Lett., 16, 303 (1966).

42. H. Röhr, "A 90° Laser Scattering Experiment for Measuring Temperature and Density of the Ions and Electrons in a Cold Dense Theta Pinch Plasma," Phys. Lett., 25A, 167 (1967).

43. H. Röhr, Institute for Plasma Physics, Garching, Germany, Report No. IPP 1/58, August 1967.

44. M. Daehler and F.L. Ribe, "Cooperative Light Scattering from θ-Pinch Plasmas," Phys. Rev., 161, 117 (1967).

45. M. Daehler, G.A. Sawyer and K.S. Thomas, "Coordinated Measurements of Plasma Density and Cooperative Light Scattering in a Theta-Pinch Plasma," Phys. Fluids, 12, 225 (1969).

46. B. Kronast, H. Röhr, E. Glock, H. Zwicker and E. Fünfer, "Measurements of the Ion and Electron Temperature in a Theta-Pinch Plasma by Forward Scattering, "Phys. Rev. Lett., 16, 1082 (1966).

47. H.-J. Kunze, "The Laser as a Tool for Plasma Diagnostics," Plasma Diagnostics, W. Lochte-Holtgreven, Ed., North Holland Pub. Co., Amsterdam (1968).

48. D.E. Evans and J. Katzenstein, "Laser Light Scattering in Laboratory Plasmas," Rep. Prog. Phys., 32, 207 (1969).

49. W.E.R. Davies and S.A. Ramsden, "Scattering of Light from the Electrons in a Plasma," Phys. Lett., 8, 179 (1964).

50. E.T. Gerry and D.J. Rose, "Plasma Diagnostics by Thomson Scattering of a Laser Beam," J. Appl. Phys. 37, 2715 (1966).

51. S.E. Schwarz, "Plasma Diagnosis by Means of Optical Scattering," J.A.P., 36, 1836 (1965).

52. M.J. Forrest, N.J. Peacock, D.C. Robinson, V.V. Sannikov and P.D. Wilcock, "Measurement of the Plasma Parameters in Tokamak T3-A by Thomson Scattering," Report CLM-R 107, U.K.A.E.A. Culham Laboratory, Abingdon, Berks, England, July 1970.

53. R.M. Patrick, "Thomson Scattering Measurements of Magnetic Annular Shock Tube Plasmas," Phys. Fluids, 8, 1985 (1965).

54. M. Martone and S.E. Segre, "Measurements on Stationary Collisionless Hydromagnetic Shock Waves," Plasma Phys., 12, 205 (1970).

55. L. Kellerer, "Measuring Magnetic Fields in Plasmas by Means of Light Scattering," Zeit. Phys., 239, 147 (1970).

56. D.E. Evans and P.G. Carolan, "Measurement of Magnetic Field in a Laboratory Plasma by Thomson Scattering of Laser Light," Phys. Rev. Lett., 25, 1605 (1970).

57. B. Kronast and R. Benesch, "Observation of a Line Structure in the Light Scattering Spectrum of Electron Plasma Waves in a Magneto Plasma," paper presented at the Gordon Conference, Andover, New Hampshire (1971).

58. H. Ringler and R.A. Nodwell, "Enhanced Plasma Oscillations Observed with Scattered Laser Light," Phys. Lett., 29A, 151 (1969).

59. H. Ringler and R.A. Nodwell, "Enhanced Cross Section for Scattering of Laser Light," Phys. Lett., 30A, 126 (1969).

60. H. Ringler and R.A. Nodwell, "Anomalous Scattering of Laser Light by a Steady State Plasma," Proc. 3rd European Conf. on Fusion, Utrecht.

61. W.H. Kegel, "On the Scattering of Light from a Non-Maxwellian Plasma," Phys. Lett., 29A, 681 (1969).

62. L.A. Farrow and S.J. Buchsbaum, Bull. Am. Phys. Soc., 10, 226 (1965).

63. H.C. Koons and G. Fiocco, "Anisotropy of the Electron Velocity Distribution in a Reflex Discharge Measured by Continuous-Wave Laser Scattering," Phys. Lett., 26A, 614 (1968).

64. H.C. Koons and G. Fiocco, "Measurements of the Density and Temperature of Electrons in a Reflex Discharge by Scattering of cw Ar Laser Light," J. Appl. Phys., 39, 3389 (1968).

65. G. McCormick and L.M. Lidsky, "The Measurement of Electron Temperature Perpendicular and Parallel to the Magnetic Field in an HCD by Thomson Scattering Diagnostics," Proc. Conf. Hollow Cathode Discharges and Their Applications, Orsay, 1971.

66. A. Klopfer, "Die Erzengung Von Hockstvakua mit Getter-Ionespumpen und das Messen von sehr Tiefen Drucken," Vacuum Tech., 10, 113 (1961).

67. E.B. Hooper, Jr., "A Review of Reflex and Penning Discharges," Advances in Electronics and Electron Physics, L. Marton, Ed., 27, 295 (1969), Academic Press, New York.

68. F.M. Penning, "Ein Neues Manometer fer Niedrige Gasdrucke Instesondere Zwischen 10^{-3} und 10^{-5} mm.," Physica, 4, 71 (1937).

69. L. Spitzer, Jr., Physics of Fully Ionized Gases, 2nd Edition, Interscience Pub., 1967.

70. R. Bingham, "Long Wavelength Instability in a Reflex Discharge," Phys. Fluids, 7, 1001 (1964).

71. D. Bohm, Chapter 2, Section 5 in The Characteristics of Electrical Discharges in Magnetic Fields, A. Guthrie and R.K. Wakerling, Eds., McGraw-Hill, 1949.

72. O. Buneman, private communication.

73. B.B. Kadomtsev and A.V. Nedospasov, "Instability of the Positive Column in a Magnetic Field and the Anomalous Diffusion Effect," Plasma Phys., 1, 230 (1960).

74. F.C. Hoh, "Instability of Penning-Type Discharges," Phys. Fluids, 6, 1184 (1963).

75. G. Guest and A. Simon, "Instability in Low-Pressure Plasma Diffusion Experiments," Phys. Fluids, 5, 503 (1962).

76. F.C. Hoh and B. Lehnert, "Screw Instability of a Plasma Column," Phys. Rev. Lett., 7, 75 (1961).

77. T.Ya. Fishkova, E.V. Shpak and S.Ya. Yaver, "Investigation of the Leakage of Charged Particles from a Discharge with Reflected Electrons," Sov. Phys. Tech. Phys., 9, 40 (1964).

78. K.I. Thomassen, "Measurements of an Anomalous Diffusion Coefficient," Phys. Fluids, 9, 626 (1966).

79. G. Briffod, M. Gregoire and S. Gruber, "Instability in a Cold Cathode Reflex Discharge," Plasma Phys., 6, 329 (1964).

80. "Inspection and Acceptance of Optical Surfaces," Military Specification MIL-O-13830A.

81. C.R. Phipps, Jr., Stanford University Institute for Plasma Research Report No. 277 (1969).

82. W.D. Gunter, Jr., E.F. Erickson and G.R. Grant, "Enhancement of Photomultiplier Sensitivity by Total Internal Reflection," Applied Optics, 4, 512 (1965).

83. J. Goodman, Introduction to Fourier Optics, McGraw-Hill (1968).

84. F.A. Jenkins and H.E. White, Fundamentals of Optics, McGraw-Hill (1957).

85. C.R. Pidgeon and S.D. Smith, "Resolving Power of Multilayer Filters in Nonparallel Light," J. Opt. Soc. Am., 54, 1459 (1964).

86. J.C. Hosea, "Probe Measurements in a Pulsed Plasma: Experimental Verification of the BBM Analysis for Ion Saturation Current," J. Appl. Phys., 37, 2695 (1966).

87. S. Glasstone and R.H. Lovberg, Controlled Thermonuclear Reactions, Van Nostrand, Princeton, New Jersey (1960).

88. J.M. Dawson and R. Shanny, "Some Investigations of Nonlinear Behavior in One-Dimensional Plasmas," Phys. Fluids, 11, 1506 (1968).